Doctoral Dissertation

博士論文

The novel membrane deformation ability of the ankyrin-repeat-containing protein ANKHD1 and its involvement on the early endosome

(アンキリンリピート含有タンパク質 ANKHD1 の
新規脂質膜小胞化活性とその初期エンドソームへの関与の同定)

A Dissertation Submitted for the Degree of Doctor of Philosophy
December 2018
平成 30 年 12 月博士 (理学) 申請

Department of Biophysics and Biochemistry, Graduate School of Science,
The University of Tokyo
東京大学大学院理学系研究科生物化学専攻

Manabu Kitamata
北又　学

Abstract

Ankyrin repeat domains (ARDs) are found in numerous proteins. ARDs are constituted of ankyrin repeats (ANKs). The number of ANKs is different among ARDs, and the shape of ANKs often form curved conformations similar to the Bin-Amphiphysin-Rvs (BAR) domain. BAR domains function as the membrane scaffold with the dimerization for tubulation of lipid membrane. Some BAR domains with amphipathic helices mediate membrane scission for small vesicle formation. However, whether ARD proteins have similar membrane tubulation and vesiculation abilities had not been elucidated. I found that the dimeric ARD of ankyrin repeat and KH domain-containing protein 1 (ANKHD1) efficiently cause membrane tubulation and vesiculation in vitro. ANKHD1 comprises 25 ANKs including the first 15 ANKs and the latter 10 ANKs. The 15 ANKs involve in dimer formation, and the 10 ANKs deform membrane into tubules and vesicles. The 10 ANKs were predicted to form a curved conformation with a positively charged protein surface like the BAR domains. Furthermore, there is the amphipathic helix adjacent to the 10 ANKs. Mutations of basic amino acid residues in the 10 ANKs and deletion of the amphipathic helix decreased the membrane vesiculation. The dimeric 25 ANKs also showed significantly higher membrane vesiculation ability than that of the 10 ANKs. Knockdown and localization of ANKHD1 in cells suggested that ANKHD1 involved in the regulation of enlargement of early endosomes by the membrane vesiculation ability. These results demonstrate that ANKHD1 enables membrane vesiculation of the early endosomes in a similar way to the BAR protein.

Contents

Abbreviations

ARDs	ankyrin repeat domains
ANKs	ankyrin repeats
BAR domain	bin-Amphiphysin-Rvs domain
PC	phosphatidylcholine
PE	phosphatidylethanolamine
PS	phosphatidylserine
SM	sphingomyelin
ER	endoplasmic reticulum
MVB	multivesicular body
ESCRT	endosomal sorting complexes required for transport
EST	expressed sequence tag
TPM	transcripts per million
EGFP	enhanced green fluorescent protein
BS(PEG)5	bis-*N*-succinimidyl-(pentaethylene glycol) ester
GTP	guanosine triphosphate
ATP	adenosine triphosphate
GST	glutathione S-transferase
PCR	polymerase chain reaction
IPTG	isopropyl β-D-1-thiogalactopyranoside
EDTA	ethylenediaminetetraacetic acid
PMSF	phenylmethylsulfonyl fluoride
DTT	dithiothreitol
SDS-PAGE	sodium dodecyl sulfate polyacrylamide gel electrophoresis
HEPES	N-2-hydroxyethylpiperazine-N-2-ethane sulfonic acid
BSA	bovine serum albumin

Chapter 1. Introduction

1-1. Membrane-deforming proteins and phospholipids in cell membrane

The inside and outside of cellular organelles are separated by lipid membrane. The organelle morphology is observed as the lipid membrane morphology and is dynamically deformed for fusion and fission during essential cellular events, including organelle division, vesicle trafficking, and endocytosis (Jarsch et al., 2016; McNiven and Thompson, 2006; Personnic et al., 2016; Praefcke and McMahon, 2004). Lipid membrane of the organelle is lipid bilayer, which mainly consists of phospholipids and sphingolipids (Evans and Hardison, 1985; Keenan and Morré, 1970). The cytoplasmic surface of the cell membrane is mostly composed of glycerophospholipids. Glycerophospholipids have a hydrophobic tail and a hydrophilic head. Glycerophospholipids are classified by the head groups. In cellular membrane, major glycerophospholipids are phosphatidylcholine (PC), phosphatidylethanolamine (PE), phosphatidylserine (PS), and phosphatidylinositol (PI) (Figure 1). PS is negatively charged lipids for its negative charge of head group. PC, PE, and PI are neutral. These glycerophospholipids have amphiphilic characteristics, and therefore, in water, glycerophospholipids are aligned with their hydrophilic heads toward water and with their hydrophobic tails toward inside.

In the membrane of eukaryote cells, PC is abundant and comprises approximately 50% of total phospholipids, and PE comprises approximately 20% of total phospholipids (Evans and Hardison, 1985; Keenan and Morré, 1970; Vance and Steenbergen, 2005). However, PS are less abundant than PE and is approximately 5% of total phospholipids (Evans and Hardison, 1985; Keenan and Morré, 1970; Vance and Steenbergen, 2005). The percentages of these phospholipids are different among intracellular organelles and plasma membrane. Plasma membrane contains a relatively high amount of PS (10%) compared with intracellular organelles (Evans and Hardison, 1985; van Meer et al., 2008). Furthermore, these glycerophospholipids are asymmetrically distributed in the membrane of the cells. In plasma membrane, sphingolipids are predominantly localized in the exoplasmic leaflet while PE and PS are predominantly localized in the cytoplasmic leaflet (Figure 2A) (Devaux, 1991; Marquardt et al., 2015; Sandra and Pagano, 1978). These asymmetric distributions could contribute to the regulation of membrane curvature by membrane-deforming proteins (Bigay and Antonny, 2012). In early endosome, the asymmetric distribution of PS is required for formation of the budding compartment and proper trafficking of vesicles to recycling endosome and Golgi (Figure 2B) (Chen et al., 2010; Lee et al., 2015; Xu et al., 2013).

The shape of lipid membrane is regulated by membrane-deforming proteins in various cellular events (Figure 3). These proteins bend membrane and regulate membrane curvature, resulting in formation of vesicles and tubules (McMahon and Gallop, 2005; Renard et al., 2018; Suetsugu, 2010). Membrane vesiculation and tubulation are performed through scaffolding such as oligomerization on the membrane surface or hydrophobic insertion such as amphipathic helix and hairpin loop (Jarsch et al., 2016; Suetsugu et al., 2014).

The membrane vesiculation is correlated with tubulation and is thought to be caused after formation of tubules. In vitro, vesicles and tubules formed by membrane-deforming proteins are frequently observed simultaneously (Boucrot et al., 2012).

1-2. The vesiculation and tubulation by membrane-deforming proteins

Bin- Amphiphysin-Rvs167 (BAR) domain superfamily proteins regulate membrane curvature for membrane tubulation (Peter et al., 2004; Shimada et al., 2007; Suetsugu et al., 2010). BAR proteins are involved in membrane invagination such as caveolae and clathrin-coated pits and membrane protrusion such as lamellipodia and filopodia (Scita et al., 2008; Senju et al., 2011; Shimada et al., 2007; Suetsugu et al., 2006). Also, BAR proteins are associated with vesicle transport from Golgi and endosome for formation of tubules (Burd and Cullen, 2014; Gehart et al., 2012). BAR domains are constituted of three helices in monomer and forms a curved structure by their dimer formation. The inner surface is abundant of basic amino acids (Peter et al., 2004). Furthermore, BAR domains are oligomerized on membrane surface upon formation of the tubes (Farsad et al., 2001). BAR domains deform membrane into tubules according to their shapes through the electrostatic interaction between the positively charged surfaces and the negatively charged lipids such as PS (Figure 4A) (Daumke et al., 2014 ; Suetsugu et al., 2014). In addition, some BAR domains, which include that of endophilin, possess amphipathic helices that are inserted into the membrane for promotion of membrane vesiculation and tubulation (Figures 4B and 4C) (Boucrot et al., 2012; Gallop et al., 2006; Masuda et al., 2006; Nishimura et al., 2018).

Several other proteins, such as Sar1p, Arf1, and Epsin, possess amphipathic helices, inducing the tubulation and vesiculation (Boucrot et al., 2012; Lee et al., 2005; Paczkowski and Fromme, 2014). Sar1p, Arf1, and Epsin are involved in vesicle formation in endoplasmic reticulum (ER), Golgi, and clathrin-coated pits, respectively (Ford et al., 2002; Kuge et al., 1994; Paczkowski and Fromme, 2014). Amphipathic helix is a cylinder of hydrophilic and hydrophobic surfaces. Therefore, the hydrophobic surface of the amphipathic helices is embedded into the outer leaflet of the lipid bilayer, inducing membrane curvature for the membrane vesiculation and tubulation (Figure 5).

Other than the proteins with amphipathic helices, there are several membrane-embedded proteins that deform the membrane. The reticulon proteins generate tubules and vesicles in vitro (Hu et al., 2008) and involve in the morphogenesis of ER (Jozsef et al., 2014). The reticulons contain ~200-1,200 amino-acid residues, and the C-terminal regions of ~200 amino-acid residues contain the conserved region with two hydrophobic regions and a hydrophilic loop.(Yang and Strittmatter, 2007). These hydrophobic regions form wedge-shaped hairpins, which are inserted into outer leaflet of the membrane, generating membrane curvature (Shibata et al., 2009).

The proteins that are involved in membrane vesiculation with other mechanisms include dynamin and endosomal sorting complexes required for transport (ESCRT).

Dynamin is mechanoenzyme that induces the membrane scission through the formation of the helical rings at the constriction sites of membrane tubes (Hinshaw and Schmid, 1995; Roux et al., 2006; Takei et al., 1995). The GTP-bound dynamin forms helical rings for constriction of the membrane. Then, the GTP hydrolysis induces disassembly of the dynamin oligomers, which accompanies the membrane scission. The binding of dynamin to membrane is mediated by the plekstrin homology (PH) domain that mediates the electrostatic interaction with negatively charged lipid and the hydrophobic loop insertion into lipid bilayer (Achiriloaie et al., 1999; Ramachandran et al., 2009), which is quite in contrast to the PH domains in the other proteins. Dynamin performs membrane fission at clathrin-coated pits, caveolae, Golgi, endosome, and mitochondria (Jones et al., 1998; Lee et al., 2016; Oh et al., 1998; Sever et al., 2000).

ESCRT proteins are composed of ESCRT-0, ESCRT-I, ESCRT-II, and ESCRT-III subunits (Babst et al., 2002a; Babst et al., 2002b; Katzmann et al., 2001; Raiborg et al., 2002). In these four subunits, ESCRT-III subunits form helical filaments on membrane by the oligomerization, leading to constriction of membrane neck (Buchkovich et al., 2013; McCullough et al., 2015; Wollert et al., 2009). ESCRT-III oligomers require the ATPase vacuolar protein sorting-associated 4 (VPS4) for the disassembly (Wollert et al., 2009). ESCRT proteins regulate multivesicular body (MVB) formation, cytokinesis, and virus budding by the membrane fission (Babst et al., 2002a; Carlton and Martin-Serrano, 2007)

1-3. Ankyrin repeat domain is the candidate for the novel membrane-deforming domain

Ankyrin repeat domain (ARD) consist of several tandemly repeated modules of ankyrin repeat (ANK). ANK is a 33 amino acids residues motif that contains two antiparallel α-helices (Figure 6). ANKs are well known to function as protein-protein interaction modules and conserved in various proteins (Li et al., 2006; Sedgwick and Smerdon, 1999). ARDs are found in eukaryotes, bacteria, archaea, and viruses (Al-Khodor et al., 2010). ARD-containing proteins are involved in essential cellular functions such as signal transduction, transcription, cell cycle regulation, immune response and so on, by the specific protein-protein interaction (Mosavi et al., 2004). Cell cycle proteins Swi6/Cdc10 in yeast and signal transduction protein Notch in *Drosophila* were first identified ARD-containing proteins (Breeden and Nasmyth, 1987). Then, ANKs were named after plasma membrane scaffold protein Ankyrin (Lux et al., 1990).

The number of ANKs is different among ARD-containing proteins (Mosavi et al., 2004). The various number of ANKs produces diverse protein surface for various protein function. There are one to 34 ANKs in ARDs, however, a few ARD-containing proteins have over 26 ANKs. The number of ANKs is ranged from one to six repeats in most of the ARDs (Mosavi et al., 2004).

Previously, transient receptor potential cation channel subfamily V member 4 (TRPV4) ARD was found to bind to negatively charged lipids, including phosphatidylinositol (4,5) bisphosphate (PI (4,5) P_2) (Takahashi et al., 2014). Also, *Arabidopsis* ankyrin repeat protein 2A (AKR2A) contain an ARD binding to phosphatidylglycerol and monogalactosyldiacylglycerol (Kim et al., 2014). These imply the possibility that uncharacterized ARDs have membrane binding ability. There is approximately 600 ARD-containing proteins in *Homo sapiens* (Letunic and Bork, 2017). However, whether most ARDs have the membrane binding and deformation abilities have not been elucidated.

The variation in ANK number often adopt curved conformations (Figure 6). These properties imply that ARDs with lipid binding ability function as membrane scaffolds for the deformation, in a similar way to the BAR domains.

1-4. Aim of my thesis

The membrane deformation for vesicles and tubules is a key process in membrane trafficking and regulation of organelle homeostasis. However, the knowledge on the mechanisms of the membrane deformation is limited to a small number of proteins identified as membrane-deforming proteins. Owing to the variety of tubules and vesicles inside cells, the proteins with membrane deformation are not considered to be fully determined.

To identify the novel membrane-deforming proteins, I focused on large protein family of ARD-containing proteins because some ARDs have curved structures similar to BAR domain or have lipid binding ability.

In this study, to identify the novel membrane-deforming proteins from ARD-containing proteins, I examined the membrane binding and vesiculation abilities of the 18 highly expressed proteins that have ARD by liposome biochemical assay (Table 1). In this screening, I identified the membrane vesiculation ability of ANKHD1. To examine the membrane organelles that were vesiculated by ANKHD1, I analyzed the size of organelles in normal cell and ANKHD1-depleted cells. Then, I found that ANKHD1 was involved in the early endosome scission to prevent the early endosome enlargement with the membrane vesiculation ability. This result was correlated with the localization of ANKHD1 in membrane fission site of the early endosome.

Chapter 2. Materials and Methods

Antibodies

The following antibodies were used in my study: rabbit anti-GFP antibody (immunofluorescence 1:400, MBL Life Science, 598), rabbit anti-ANKHD1 antibody (western blotting 1:1000, immunofluorescence 1:200, Atlas Antibodies, HPA008718), mouse anti-EEA1 antibody (western blotting 1:1000, immunofluorescence 1:200, BD Biosciences, 610456), rabbit anti-EEA1 antibody (immunofluorescence 1:200, Cell Signaling Technology, 3288), mouse anti-GAPDH antibody (western blotting 1:1000, Santa Cruz Biotechnology, sc-166574), mouse anti-GM130 antibody (western blotting 1:500, immunofluorescence 1:200, BD Biosciences, 610822), mouse anti-Bcl-2 antibody (western blotting 1:500, BD Biosciences, 610538), mouse anti-Calnexin antibody (western blotting 1:200, immunofluorescence 1:400, Santa Cruz Biotechnology, sc-23954), mouse anti-mCherry antibody (immunofluorescence 1:200, Novus, NBP1-96752), mouse anti-Rab5 antibody (western blotting 1:1000, immunofluorescence 1:200, Santa Cruz Biotechnology, sc-46692), mouse anti-LAMP1 antibody (immunofluorescence 1:200, Santa Cruz Biotechnology, sc-20011), and mouse anti-Tom20 antibody (immunofluorescence 1:200, Santa Cruz Biotechnology, sc-17764).

Plasmids

Human ANKHD1 195–1418 aa (ARD25) were amplified by polymerase chain reaction (PCR) from ANKHD1 cDNA with the following primers: 5’-GAAGATCTGCAGAAAACAGCCACAATG-3’ and 5’-GAAGATCTTTAGTCTTTAGCCTTCACAATG-3’. They were inserted into the pCold Glutathione S-transferase (GST) vector (TaKaRa Bio) at the BamH1 restriction site.

The pEGFP-N3-ANKHD1 195-1418 aa was generated by using Gibson Assembly Master Mix (New England BioLabs). ANKHD1 195-1418 aa cDNA was amplified by the following primers: 5’-

CGGTACCGCGGGCCCGGGATCCGCCACCATGGCAGAAAACAGCCACAATG-3’ and 5’- CACCATGGTGGCGATGGATCCGTCTTTAGCCTTCACAATG-3’. They were inserted into the pEGFP-N3 vector using the BamH1 restriction site.

To generate the pVenus×3 vector, I replaced EGFP in the pEGFP-N3 vector with Venus×3. The backbone of the pEGFP-N3 vector was amplified by PCR with the following primers: 5’-TAAAGCGGCCGCGACTCTAG-3' and 5’-GGTGGCGATGGATCCCGGG-3’. Each Venus cDNA was amplified by PCR with the following primers:

5’-CCGGGATCCATCGCCACCATGGTGAGCAAGGGCGAG-3’ and 5’-GGCAGATCTGAGTCCGGACTTGTACAGCTCGTCCATG -3’.

5’- TCCGGACTCAGATCTGCCACCGCGGTGAGCAAGGGCGAGGAG-3’ and 5’-CGCGGTGGCGATGGATCCGCTCTTGTACAGCTCGTCCATGC-3’.

5’-GCGGATCCATCGCCACCGCGGTGAGCAAGGGCGAGGAGC-3’ and 5’-CTAGAGTCGCGGCCGCTTTACTTGTACAGCTCGTCCATGC-3’. These four fragments were then assembled by Gibson Assembly Master Mix.

The pVenus×3-ANKHD1 was prepared by Gibson Assembly Master Mix. The five cDNA fragments included the vector backbone of pEGFP-N3 vector, cDNA of full-length ANKHD1 (1-2542 aa), and three Venus cDNAs. The vector backbone of pEGFP-N3 vector was amplified by PCR with the following primers: 5’-TAAAGCGGCCGCGACTCTAG-3’ and 5’-ATCAGTCAGCATGGTGGCAGATCTGAGTCCGGTAGCGC-3’.

The three Venus cDNAs were amplified by the following primers: 5’-TCTCAAATATGTCAACAGCGGATCCATCGCCACCGCGGTGAGCAAGGGCG-3’ and 5’-GGCAGATCTGAGTCCGGACTTGTACAGCTCGTCCATG-3’. 5’-TCCGGACTCAGATCTGCCACCGCGGTGAGCAAGGGCGAGGAG-3’ and 5’-CGCGGTGGCGATGGATCCGCTCTTGTACAGCTCGTCCATGC-3’. 5’-AGCGGATCCATCGCCACCGCGGTGAGCAAGGGCGAGGAGC-3’ and 5’-CTAGAGTCGCGGCCGCTTTACTTGTACAGCTCGTCCATGC-3’.

The full-length of ANKHD1 was amplified from ANKHD1 cDNA by the following primers: 5’- GAAGATCTGCCACCATGCTGACTGATAGCGGAGG and GAAGATCTGTTGACATATTTGAGATGC-3’. The cDNA sequence was inserted into the pMD20-T vector by Mighty TA-cloning Kit (TaKaRa Bio). Then the cDNA of ANKHD1 full-length was extracted by BglII digestion for the preparation of pVenus×3-ANKHD1.

To prepare the constructions of siRNA resistant ANKHD1, five silent mutations were induced by site-directed mutagenesis in each target sequence of the three siRNAs: 5′-GGTGGAAACAGCGACTCTGATAAC-3′, 5′-GTGACACCCAACTCTTTGTCCACCAG-3′, and 5′-AGCAGCTGTGCGTGACAAACACCCGG-3′.

The cloning strategies of the plasmids used in the thesis are shown in Table 2.

Protein purification

Plasmids for expression of GST-tagged protein were transformed into Rosetta2 competent cells (Novagen). The cells were cultured in Luria broth (LB) medium at 37°C, and then proteins were overexpressed by addition of 1 mM isopropyl β-D-1-thiogalactopyranoside (IPTG). The incubation temperature of each plasmid for protein expression is shown in Table 3. The cells were incubated overnight at the indicated temperature. The cells were collected by centrifugation and then suspended in lysis buffer containing 10 mM Tris-HCl (pH 7.5), 150 mM NaCl, 1 mM EDTA, 0.5% Triton X-100 (8 mM), 1 mM phenylmethylsulfonyl fluoride (PMSF), and 2 mM 2-mercaptoethanol by using an ultrasonic homogenizer. After the lysate was centrifuged, the supernatant was incubated with the glutathione-sepharose 4B beads at 4°C for 1 hr. The beads were washed four times using approximately 10-fold dilutions in buffer containing 10 mM Tris-HCl (pH 7.5), 150 mM NaCl, 1 mM EDTA, and 1 mM dithiothreitol (DTT). Protein was collected by cleavage using prescission protease from the GST tag at 4°C overnight. The protein was stored at -80°C

Preparation of liposomes

PC (Sigma, P3841), PE (Sigma, P7693), PS (Sigma, P5660), and porcine brain lipids (Avanti, 131101P) were used. These lipids in chloroform were mixed as indicated weigh ratios to 10 μg of total lipid. Then, Rhodamine-PE (Avanti, 810150) was incorporated into the total lipids at 0.2% to visualize the liposome precipitation by ultracentrifugation. These lipids were dried at 37°C under nitrogen gas, and then maintained under vacuum to remove residual chloroform at room temperature for 20 min. The dried lipids were suspended in 10 mM Tris-HCl (pH 7.5), 150 mM NaCl, and 1 mM EDTA to 0.2 mg/ml, and then incubated at 37°C for 1 hr. In Figures 28B and 28C, liposomes were extruded 11 times through 800 nm polycarbonate filters by an extruder (Avanti).

Liposome sedimentation assay

The aggregates of proteins were removed by ultracentrifugation (109000 × g) for 20 min at 25°C before incubation with liposomes. The liposomes as described above were incubated with the proteins in 10 mM Tris-HCl (pH 7.5), 150 mM NaCl, 1 mM EDTA, and 0.5 mM DTT at room temperature for 30 min. After incubation, these solutions were centrifuged at 109000 × g to test the membrane vesiculation and at 245000× g to test the binding to liposomes in a TLA-100 rotor (Beckman) at 25°C for 20 min. The supernatant and pellet fractions were separated, and then SDS-PAGE sample buffer was added into the fractions to the same volume. Rhodamine-PE and proteins in the fractions were analyzed by SDS-PAGE. The fluorescence of rhodamine-PE in the supernatant and pellet fractions was measured by an FLA-8000 fluorescence image analyzer (Fuji-Film), and then the band intensities of Rhodamine were quantified by ImageJ software for the vesiculation of liposomes by proteins. The proteins were stained by Coomassie brilliant blue staining (CBB). The percentages of the proteins in the supernatant and pellet fractions were measured by ImageJ software for the protein binding to liposomes.

Electron microscopy

Liposomes (0.2 mg/ml) prepared at the indicated weight ratio of lipids were incubated with proteins in 10 mM Tris-HCl (pH 7.5), 150 mM NaCl, and 1 mM EDTA for 20 min at 25°C. After the incubation, a grid coated with formvar was put on the mixture for 1 min at 25°C and subsequently washed with 100 mM HEPES (pH 7.5). The grid was stained with 0.5% uranyl acetate for 30 s. The grids prepared by negative stain were observed by transmission electron micrography (Hitachi H-7100).

Crosslinking analysis

Proteins (250 nM) were incubated at room temperature for 30 min with or without liposomes (0.2 mg/ml) in 10 mM HEPES (pH 8.0), 150 mM NaCl, 1 mM EDTA, and 0.5 mM DTT. After the incubation, the mix solution was incubated with 100 µM BS(PEG)5 (Thermo Fisher Scientific, 21581) for 30 min at room temperature. The reaction was quenched by addition of SDS-PAGE sample buffer. The proteins analyzed by SDS-PAGE were stained by CBB.

Transfection and siRNA treatment

Caki-1 (human clear cell renal cell carcinoma), DLD1 (human colorectal adenocarcinoma) cells, HEK293T (human embryonic kidney), HeLa (human cervical epithelioid carcinoma), and U2OS (human bone osteosarcoma) were cultured in Dulbecco's modified Eagle's medium supplemented with 10% fetal bovine serum, penicillin, and streptomycin at 37°C in an atmosphere of 5% CO_2. One day before transfection, 5×10^4 cells were grown in wells of 6-well dishes. The cells were transfected with plasmid using Lipofectamine 3000 (Invitrogen). After transfection for 24 hr at 37°C with 5% CO_2, the cells were analyzed by confocal microscopy or subjected to western blotting.

ANKHD1 knockdown was performed by using stealth RNAi (Invitrogen).

The siRNA sequences were 5’-CAGGU GGGAA UAGUG AUUCA GAUAA-3’, 5’-GAAGU GACUC CUAAU UCCUU GUCAA-3’, and 5’-CAGUC AGCAA CUGUG UGUCA CUAAU-3’. These siRNAs were mixed, and then transfected into the cells using Lipofectamine 3000. The Negative Control stealth RNAi siRNA (Invitrogen) was also transfected as a control. One day before siRNA transfection, 5×10^4 cells were grown in wells of 6-well dishes, and then siRNA was transfected at 20 nM into the cells. After 48 hr of transfection at 37°C with 5% CO_2, the cells were analyzed by confocal microscopy or subjected to western blotting.

Immunostaining

Caki-1 cells, DLD1 cells, HEK293T cells, HeLa cells, and U2OS cells were fixed in 4% paraformaldehyde/PBS at room temperature for 10 min, permeabilized in 50 mM Tris-HCl (pH 7.5), 100 mM NaCl, and 0.1% Triton X-100 at room temperature for 10 min, and then blocked in a buffer containing 50 mM Tris-HCl (pH 7.5), 100 mM NaCl, and 1% bovine serum albumin (BSA) at room temperature for 1 hr. The cells were incubated with primary antibody as described above in 50 mM Tris-HCl (pH 7.5), 100 mM NaCl, and 1% BSA for 1 hr at room temperature. After washing by using PBS, the cells were incubated with secondary antibody conjugated with Alexa Fluor 488 or 568 in 50 mM Tris-HCl (pH 7.5), 100 mM NaCl, and 1% BSA for 1 hr at room temperature. The cells were washed with PBS and mounted in ProLong Diamond Antifade Mountant (Invitrogen).

Confocal microscopy (FV1000D, Olympus) with a 100× immersion objective lens (NA 1.40, Olympus) was used to acquire all fluorescence images for live and fixed cell. Z-stack images in Figure 15 were acquired at 0.4 μm intervals.

Live cell imaging

Lysosomes were visualized by using 75 nM Lysotracker Red DND-99 (Molecular Probes, L7528) at 37°C with 5% CO_2 for 1 hr. Mitochondria were stained using 200 nM

Mitotracker Red CM-H_2Xros (Molecular Probes, M7513) at 37°C with 5% CO_2 for 45 min. I observed live cells by confocal microscopy at 37°C with 5% CO_2.

Quantification of organelle area

The number of puncta, total area, and average area of organelles per cell were calculated using ImageJ software from fluorescence images with the focal plane close to the cell attachment on the coverslips, where the area of cell is the largest. Fluorescence images of organelles per cell were converted into binary images. In each experiment, the images were set in equal thresholds. The minimal particles size was determined as 0.04 μm^2, and then the organelles were evaluated by the *Analyze Particles* in the ImageJ software.

Quantification of colocalization in cells

The percentages of colocalization of two proteins per cell in Figure 16, Figure 17, Figure 20, and Figure 21 were calculated by using the Colocalization Threshold in the ImageJ software. Colocalization indicates the overlap with green and red channel of two proteins above a threshold and shows the pixels that have both channels. Colocalization were represented as the number of pixels that had both channels / total number of pixels of each channel. In each experiment, fluorescence images by confocal microscopy were set in equal thresholds.

Statistical analysis

Statistical differences were determined by paired two tailed Student's *t*-test in Figure 8, Figure 12, Figure 13, Figure 16B, Figure 25, Figure 27, Figure 28, Figure 30, and Figure 31B. Unpaired two tailed Student's *t*-test were performed in Figure 14, Figure 15, Figures 16D-16H, Figure 20, Figure 22, Figure 23, Figure 26, Figures 31D-31F, and Figure 32. The number of repeated experiments and *P*-values are described in figure legends. All error bars represent standard error.

Chapter 3. Results

3-1. ANKHD1 ARD is a membrane vesiculation protein

I expected that highly transcribed genes have important role for various cellular functions. I selected 18 genes for the relatively high frequencies of expressed sequence tags (EST) in the Unigene database (Boguski and Schuler, 1995) among the approximately 600 ARD-containing proteins in *Homo sapiens* (Letunic and Bork, 2017) (Figure 7).

I purified 18 ARDs containing fragments derived from human or mouse in *Escherichia coli* (Figure 8A). Then, ARD binding to the liposomes and the vesiculation of the liposomes by the proteins were examined with a liposome sedimentation assay. In the liposome sedimentation assay, liposomes are precipitated by centrifugation. Co-precipitation of the protein with liposomes indicates the protein binding to the liposomes. As sedimentation efficiency depends on the size of the liposome, the precipitation of the liposome decreases as the liposome size decreases in the presence of proteins. This decrease in the sedimentation of liposomes indicates the membrane vesiculation by the protein (Boucrot et al., 2012). The quantity of liposomes in the supernatant (S) and the pellet (P) was measured by rhodamine-labeled phosphatidylethanolamine (PE) incorporated into liposomes (Figure 8B).

I prepared liposomes made of 60% PC, 30% PE, and 10% PS at a weight ratio because PS is less abundant than PC and PE, while PC and PE are abundant in the Golgi complex, mitochondria, ER, and endosomes (Evans and Hardison, 1985; Horvath and Daum, 2013; Keenan and Morré, 1970; Marquardt et al., 2015; van Meer et al., 2008). Each of the 18 ARDs containing fragments was incubated with the protein-free liposomes (Figures 8C–8G). The ARD of human ANKHD1 (ANKHD1 195–1418 amino acid residues (aa), termed ARD25), displayed the highest vesiculation of the liposomes among the 18 ARD-containing fragments, (Figure 8E). Ankyrin repeat domain-containing protein 17 (ANKRD17), which is a paralogue of ANKHD1, also showed vesiculation (Figure 8G). Ankyrin repeat and FYVE domain-containing 1

(ANKFY1) showed weak vesiculation compared to ANKHD1 (Figure 8E).

To examine whether there is a group of ANKs with membrane vesiculation ability, I examined ANKs of all of ARDs in *Homo sapiens* for sequence similarities. The amino acid sequences of the ANKs of ANKHD1 are similar to that of ANKRD17, showing a distinct group in the 18 ARDs (Figure 9). However, the ANKs of ANKHD1 does not form a group based on amino-acid sequence similarity among all of ARDs in *Homo sapiens* (Figure 10), which suggests that an assembly of several ANKs is important for ARD with their proper function. The frequency of average EST of ANKHD1 was 167 transcripts per million (TPM) and the TPM of ANKHD1 was the highest among the 18 ARDs containing proteins (Figure 7B). The EST frequency of ACTR3 (Arp3) and SH3GL1 (endophilin A2) was 234 TPM and 100 TPM, respectively. These TPM were equivalent to those of ANKHD1. ACTR3, which causes branched actin filaments, is a component of the Arp2/3 complex. Endophilin A2 is BAR domain containing protein. Therefore, I selected ANKHD1 in subsequent studies for the highest EST frequency similar to SH3GL1 and ACTR3, suggesting the essential role of ANKHD1 in cellular events.

To examine whether ARD25 protein vesiculates liposomes composed of natural lipids, the vesiculation of liposomes composed of total lipids from porcine brain (Folch fraction) was examined via the liposome sedimentation assay. Liposomes composed of the Folch fraction were vesiculated by ARD25 at 1 μM (Figures 11A and 11B). However, liposomes made of the Folch fraction or 60% PC / 30% PE / 10% PS were not vesiculated by ARD25 at 250 nM (Figures 11A and 11B). To confirm the vesiculation of the liposomes by ARD25 at 1 μM, I observed the liposomes after incubation with ARD25 by transmission electron microscopy. ARD25 at 1 μM vesiculated the liposomes composed of 60% PC / 30% PE / 10% PS and the Folch fraction into small vesicles, which was consistent with the liposome sedimentation assay (Figures 11C and 11D). These results indicate that the ARD of ANKHD1 can vesiculate the liposomes made of natural lipids and 60% PC / 30% PE / 10% PS depending on the protein concentration.

3-2. ANKHD1 knockdown increases total area of EEA1-positive early endosomes and decreases that of mitochondria

To examine the intracellular function of ANKHD1 with membrane vesiculation ability, ANKHD1 was downregulated in HeLa cells by small interfering (si)RNA. I performed western blotting to quantify marker proteins for organelles, including Bcl-2 for mitochondria (Wolter et al., 1997), EEA1 for early endosomes (Zoncu et al., 2009), GM130 for cis-Golgi (Nakamura et al., 1995), and Calnexin for ER (Wang et al., 2000). Whole cell lysates with control siRNA and ANKHD1 siRNA treatment were analyzed by western blots (Figure 12). The decrease of ANKHD1 increased the amount of EEA1, Calnexin, and GM130 and decreased the amount of Bcl-2 (Figure 12). Glyceraldehyde 3-phosphate dehydrogenase (GAPDH) was employed as a standard. A similar upregulation of EEA1 was shown in Caki-1, DLD1, HEK293T, and U2OS cells by the knockdown of ANKHD1 (Figure 13).

Thereafter, I measured the area of EEA1-positive early endosomes, cis-Golgi, ER, and mitochondria in HeLa cells with control siRNA or ANKHD1 siRNA treatment by confocal microscopy (Figure 14). At each focal plane in the confocal microscope, ANKHD1 knockdown increased the number of EEA1 puncta and the total area of EEA1 localization (Figure 15). Therefore, I selected the focal plane that was adjacent to the cell attachment on the coverslips because the area is the largest in cells, in order to examine the changes of organelle area between control siRNA-treated cells and ANKHD1 siRNA-treated cells. The number of EEA1 puncta and the total area of EEA1 localization in ANKHD1-depleted HeLa cells were approximately 1.5-fold larger than that in the control HeLa cells (Figures 14A-14C), suggesting that the EEA1-positive early endosomes increased in ANKHD1-depleted HeLa cells. ANKHD1 siRNA treatment did not change the number of Golgi fragments and the total area of GM130 localization (Figures 14D-14F). In addition, ANKHD1 siRNA treatment also did not change the total area of Calnexin localization (Figures 14G and 14H). Interestingly, the total area of mitochondria stained by Mitotracker in ANKHD1-depleted HeLa cells was approximately 70% that of mitochondria in control HeLa cells (Figures 14I and 14J). Hence, the knockdown of ANKHD1 was involved in an increase of the EEA1-positive early endosome total area and a decrease of the mitochondria total area. Since ANKHD1 vesiculates the membrane into small vesicles, the depletion of ANKHD1 was thought to enlarge the area of target organelles where ANKHD1 mediated membrane scission. Therefore, potential sites of ANKHD1 function are the EEA1-positive early endosomes, not mitochondria.

EEA1 is known as the membrane tethering factor of early endosomes, functions with the small GTPase Rab5 for fusion of endocytic vesicles (Murray et al., 2016), and can thus localize in mature early endosomes, while Rab5 localizes in endocytic vesicles and early endosomes regardless of early endosome maturation (Friedman et al., 2013; He et al., 2017; Zoncu et al., 2009). The amount of endogenous Rab5 was not changed in ANKHD1 siRNA-treated HeLa cells (Figures 16A and 16B). The total area of Rab5 localization was not changed in ANKHD1 siRNA-treated HeLa cells (Figures 16C and 16D). However, ANKHD1 siRNA treatment in HeLa cells decreased the number of Rab5 puncta (Figure 16E). The smaller Rab5 puncta also decreased in the size distribution, where the average area of Rab5 puncta increased (Figures 16F and 16G). Furthermore, the colocalization of Rab5 with EEA1 increased upon treatment of ANKHD1 siRNA (Figure 16H), where most of the Rab5-positive puncta contained the EEA1-positive puncta. Therefore, these results suggest that Rab5-EEA1-double-positive early endosomes were increased in ANKHD1-depleted HeLa cells. Thus, an increase of the number of EEA1-positive puncta in ANKHD1 siRNA-treated HeLa cells is considered to be an increase of the number of mature early endosomes by the suppression of the membrane vesiculation by ANKHD1, which would further suppress the subsequent vesicle transport from early endosome.

3-3. Localization of ANKHD1 in Rab5-positive early endosomes

To investigate the intracellular localization of ANKHD1 in HeLa cells, anti-ANKHD1 and anti-EEA1 antibodies were used for visualization of endogenous ANKHD1 and EEA1 in immunostaining. The partial colocalization of the two proteins was observed by confocal microscopy (Figure 17). Similar to HeLa cells, endogenous ANKHD1 partially colocalized with endogenous EEA1 in Caki-1, DLD1, HEK293T, and U2OS cells (Figure 18). Expressed ANKHD1 tagged with enhanced green fluorescent protein (EGFP) also partially colocalized with endogenous EEA1 in HeLa cells (Figure 19).

To further examine the ANKHD1 localization on early endosomes, I investigated the colocalization of Rab5 with endogenous ANKHD1, because activation of Rab5 regulates recruitment of EEA1 to early endosomes (Lawe et al., 2002). Endogenous ANKHD1 was partially colocalized with expressed mCherry-tagged Rab5, the expressed mCherry-tagged constitutive active Rab5 with Q79L mutation, and endogenous Rab5 (Figure 20 and Figures 21A and 21F). The percentage of colocalization of the Rab5Q79L with ANKHD1 was increased in ANKHD1 siRNA-treated HeLa cells (Figures 20B and 20C). Therefore, ANKHD1 was thought to be recruited on early endosomes by Rab5 activation. In addition to Calnexin for ER and GM130 for cis-Golgi, anti-Tom20 and anti-LAMP1 antibodies were used for labeling of mitochondria and late endosomes/lysosomes, respectively, in immunostaining (Kanaji et al., 2000; Saftig and Klumperman, 2009). Colocalization of Rab5 and Tom20 with ANKHD1 was higher than that of GM130, LAMP1, and Calnexin (Figure 21).

3-4. ANKHD1 antagonizes Rab5-mediated early endosome enlargement

I examined the effect of the decrease of ANKHD1 on the number and average area of Rab5-positive early endosomes in HeLa cells. Interestingly, the knockdown of ANKHD1 remained unchanged the number of expressed EGFP-tagged Rab5 puncta, but decreased the number of expressed EGFP-tagged Rab5Q79L puncta (Figures 22A, 22B, 22D and 22E). However, the depletion of ANKHD1 increased the average area of the EGFP-Rab5 puncta and the EGFP-Rab5Q79L puncta (Figures 22A, 22C, 22D, and 22F), where the small EGFP-Rab5Q79L puncta were almost absent. Then, I examined the localization of ANKHD1 in Rab5-positive early endosomes without fixation. To better visualize expressed ANKHD1 in cell, Venus×3 tag, which was tandem repeats of three Venus (Nagai et al., 2002), was prepared. Then, Venus×3-tagged ANKHD1 was expressed in HeLa cells. In ANKHD1 siRNA-treated HeLa cells weakly expressing ANKHD1-Venus×3, the ANKHD1 transiently colocalized with mCherry-Rab5 and mCherry-Rab5Q79L puncta upon membrane scission of early endosomes (Figures 22G and 22H).

The switch from Rab5 to Rab7 has important role in the maturation of early endosomes to late endosomes/lysosomes. Endosome maturation is associated with the acidification of the lumen and is visualized via Lysotracker staining (Huotari and Helenius, 2011; Rink et al., 2005). The total area, the number, and the average area of lysosome puncta stained by Lysotracker were not changed by ANKHD1 knockdown (Figure 23). Since early endosomes are enlarged by fusion of endocytic vesicles, these results suggested that ANKHD1 antagonized the Rab5-localized early endosome enlargement by the membrane vesiculation without affecting endosome maturation (Figure 24).

3-5. The regions necessary for dimerization and membrane vesiculation in ANKHD1

To investigate the mechanism of vesicle formation by ANKHD1, the predicted structured (ordered) and disordered regions in ANKHD1 were examined by using a disorder-prediction program (Ward et al., 2004). ANKHD1 contains 25 ANKs and a KH domain. The region outside of the 25 ANKs was mostly disordered (Figure 25A). I prepared the ANKHD1 fragments, including ANKHD1 1-885 aa (N+ARD15), ANKHD1 886-1587 aa (ARD10), and ANKHD1 1–1587 aa (N+ARD25). N+ARD15 and ARD10 contain the first 15 ANKs and the latter 10 ANKs, respectively (Figure 25A).

When the EGFP-tagged ANKHD1 fragments and EGFP-tagged ANKHD1 were expressed in ANKHD1-depleted HeLa cells via ANKHD1 siRNA treatment, the expression levels of N+ARD15-EGFP, N+ARD25-EGFP, and ARD25-EGFP were equivalent and higher than that of ANKHD1-EGFP (Figure 25B). However, the expression level of ARD10-EGFP were very low (Figure 25B). The expression of ANKHD1-EGFP and N+ARD25-EGFP decreased the amount of EEA1 in ANKHD1 siRNA-treated HeLa cells (Figures 25B and 25C), however, the other fragments did not significantly decrease the amount of EEA1 as shown by western blotting. The effect of ARD10-EGFP on the amount of EEA1 was unclear because of its extremely low expression. Therefore, these results suggested that the N+ARD25 fragment was the active fragment for vesiculation of early endosomal membrane.

Then, I investigated the effect of expressed ANKHD1-EGFP and its fragments on the total area of EEA1 localization and the number of EEA1 puncta in HeLa cells (Figures 26A-26D). The expressed N+ARD25-EGFP and ANKHD1-EGFP reduced the total area of EEA1 localization compared with other ANKHD1 fragments (Figure 26C). The expressed ANKHD1-EGFP slightly reduced the number of EEA1 puncta, though the expressed ANKHD1 fragments did not significantly reduce the number of EEA1 puncta (Figure 26D). Therefore, the expression of the N+ARD25 fragment or ANKHD1 was suggested to reduce the EEA1-positive early endosomes. In contrast, the expression of N+ARD25-EGFP did not change the total area of mitochondria, ER, and cis-Golgi as examined by Mitotracker, Calnexin, and GM130 staining, respectively (Figures 26E-26J). The expressed N+ARD25-EGFP also did not change the number of Golgi fragments (Figure 26K).

Furthermore, I purified the ANKHD1 fragments from *E.coli*, and then examined vesiculation of liposomes made of 60% PC, 30% PE, and 10% PS with the ANKHD1 fragments *in vitro*. The phospholipid composition is thought to resemble that of early endosomes (Evans and Hardison, 1985; Kobayashi et al., 1998). The N+ARD25 fragment displayed higher membrane vesiculation ability than that of the

N+ARD15, ARD10, and ARD25 fragments in the liposome sedimentation assay at a 250 nM protein concentration (Figures 27A and 27B). I observed the liposome after incubation with these ANKHD1 fragments (250 nM) via transmission electron microscopy. Consistent with the liposome sedimentation assay, N+ARD25 vesiculates the membrane into small vesicles. Although N+ARD15 did not deform the membrane, ARD10 and ARD25 deformed the liposomes into tubules (Figure 27C). Interestingly, ARD10 showed higher membrane vesiculation ability than that of N+ARD15 at 1 μM (Figures 27D and 27E).

Since the proteins with membrane deformation ability often form dimers and oligomers, the oligomerization of ANKHD1 with or without liposomes made of 60% PC, 30% PE, and 10% PS was examined using a chemical crosslinking. The dimerization of N+ARD15, N+ARD25, and ARD25 were detected by the crosslinking via bis-*N*-succinimidyl-(pentaethylene glycol) ester (BS(PEG)5) (Figure 27F). N+ARD25 was more effectively crosslinked than N+ARD15 and ARD25 (Figure 27F). In contrast, the clear dimer bands of ARD10 were not detected by the crosslinking (Figure 27F). The dimerization occurred with or without liposomes. These results suggest that N+ARD15 involves in dimerization, enabling the efficient membrane vesiculation through ARD10.

3-6. Membrane vesiculation by ANKHD1 results from electrostatic interactions and the amphipathic helix

PS at the deformation sites of early endosomes and recycling endosomes is thought to be enriched in cytoplasmic leaflet by lipid flippase (Chen et al., 2010; Lee et al., 2015; Uchida et al., 2011; Xu et al., 2013). Therefore, I examined the vesiculation of liposomes containing 40% PC / 30% PE / 30% PS. The N+ARD25 fragment showed the most efficient membrane vesiculation of liposomes containing 40% PC / 30% PE / 30% PS as well as membrane vesiculation of liposomes containing 60% PC / 30% PE / 10% PS (Figure 28A). Membrane vesiculation of these liposomes was dependent on the protein concentration of N+ARD25 fragment (Figures 28B and 28C). Then, the liposomes were filtered to reduce the liposome size larger than 800 nm. The N+ARD25 fragment vesiculated the filtered liposomes in a similar manner to the liposomes without filtration. These results suggested that ANKHD1 did not require the large liposome diameter for the membrane vesiculation (Figures 28B and 28C). I also examined the binding of these ANKHD1 fragments in the liposome sedimentation assay by increasing the centrifugation speed. The N+ARD15 fragment did not bind to these liposomes while the ARD10, N+ARD25, and ARD25 fragments bound to these liposomes, indicating that ANKHD1 binds to liposomes through the region containing ARD10 (Figure 28D).

I tried to examine the contribution of electrostatic interactions between the negatively charged lipids and the positively charged amino acid residues (basic amino acid residues) of ANKHD1 for the membrane vesiculation ability. The latter 10 ANKs have more frequent basic amino acid residues at position 1 and position 2 in the ANK than the first 15 ANKs in sequence alignments among the ANKs in ANKHD1 (Figure 29A). To detect the positively charged surface of the 10 ANKs, the structural model of the 10 ANKs was predicted by the Phyre2 program (Kelley et al., 2015) (Figures 29B and 29C). K1323, K1324, R1357, and K1358 were substituted into acidic amino acid residues to reduce the positive charge on surface of the latter 10 ANKs, resulting in the K1323E-K1324E or R1357E-K1358E mutations (Figure 30A). At 250 nM and 150 nM protein concentrations, the N+ARD25 with K1323E-K1324E or R1357E-K1358E mutations showed weaker membrane vesiculation than N+ARD25 in the liposome sedimentation assay (Figures 30B and 30C). These results suggest that membrane vesiculation by ANKHD1 is caused by electrostatic interactions between proteins and the lipid membrane.

The amphiphilicity of a potential α-helix is shown as the hydrophobic moment, which is determined by using Heliquest (Gautier et al., 2008). The hydrophobic moment of ANKHD1 indicated that ANKHD1 had a possible amphipathic helix at 1400–1415 aa (Figures 29D and 30A). At 250 nM and 150 nM protein concentrations, deletion of 1400–1415 aa (Δ1400-1415 aa) in N+ARD25 reduced the membrane vesiculation in the liposome sedimentation assay (Figures 30B and 30C).

Next, I prepared the K1323E-K1324E + R1357E-K1358E (4E) and K1323E-K1324E + R1357E-K1358E + Δ1400-1415 aa mutations (4E+ΔAH) in N+ARD25. At 250 nM, the 4E+ΔAH mutant dramatically decreased the membrane vesiculation compared to N+ARD25 and the 4E mutant in the liposome sedimentation assay (Figure 30D). Transmission electron microscopy revealed that the N+ARD25 fragment vesiculated liposomes into small vesicles, but 4E+ΔAH mutant did not vesiculate liposomes (Figure 30E). Therefore, the combination of mutations reducing basic amino acid residues and deletion of the amphipathic helix further decreased the membrane vesiculation ability. These results indicated that both the amphipathic helix and electrostatic interactions between membrane and protein were required for the membrane vesiculation and deformation, suggesting that ANKHD1 can mediate membrane scission for vesicle formation in a similar way to that of BAR proteins with amphipathic helices.

3-7. The membrane vesiculation by ANKHD1 regulates the number and area of early endosomes

I examined the involvement of the membrane vesiculation ability of ANKHD1 in the regulation of early endosomes. The siRNA-resistant ANKHD1-EGFP and its 4E+ΔAH mutant were expressed in HeLa cells treated with ANKHD1 siRNA to level similar to the endogenous ANKHD1 (Figure 31A). The amount of EEA1, the number of EEA1 puncta, and the total area of EEA1 localization in ANKHD1 siRNA-treated HeLa cells was increased compared to those in control siRNA-treated HeLa cells (Figures 31A-31E). In ANKHD1 siRNA-treated HeLa cells, the expressed ANKHD1-EGFP, but not the expressed 4E+ΔAH-EGFP, restored the amount of EEA1, the number of EEA1 puncta, and the total area of EEA1 localization to the levels in the control siRNA-treated HeLa cells (Figures 31A-31E). To examine the effect of membrane vesiculation by ANKHD1 on enlargement of the EEA1-positive early endosomes, the size distribution of EEA1 puncta was analyzed in control siRNA-treated HeLa cells and ANKHD1 siRNA-treated HeLa cells. In ANKHD1 siRNA-treated HeLa cells, the number of EEA1 puncta was increased in all four size ranges ($< 0.1\ \mu m^2$, $0.1\text{-}0.2\ \mu m^2$, $0.2\text{-}0.4\ \mu m^2$, and $0.4< \mu m^2$) (Figure 31F). ANKHD1-EGFP expression, but not 4E+ΔAH-EGFP expression, restored the number of EEA1 puncta in all four size ranges in ANKHD1 siRNA-treated HeLa cells to the levels in control siRNA-treated HeLa cells (Figure 31F). The average area of the EEA1 puncta in these HeLa cells was largely unchanged (Figure 31G). These results indicate that ANKHD1-mediated membrane vesiculation is essential for vesiculation of EEA1-positive early endosomal membrane.

I expressed the siRNA-resistant ANKHD1-Venus×3 and its 4E+ΔAH mutant in ANKHD1-depleted HeLa cells to the similar level of endogenous ANKHD1 (Figure 32A). The expression of ANKHD1-Venus×3 was sufficient to restore the number and average area of expressed mCherry-Rab5Q79L-positive puncta, while the expression of 4E+ΔAH-Venus×3 could not restore those of expressed mCherry-Rab5Q79L-positive puncta (Figures 32B-32D). These results suggest that ANKHD1 regulates the morphology of early endosomes through the vesiculation ability.

Chapter 4. Discussion

4-1. Mechanism of the membrane vesiculation by ANKHD1

Most of the proteins with membrane fission ability, including dynamin, ESCRT proteins, and endophilin, assemble into dimers and/or oligomers. These structures are supposed to be essential for membrane tubulation for vesiculation (Antonny et al., 2016; Boucrot et al., 2012; Wollert et al., 2009).

The ARD of ANKHD1 can deform liposomes into tubules and vesicles in my studies. ANKHD1 contains 25 ANKs, which consist the former 15 ANKs and the latter 10 ANKs. I observed the dimerization of ANKHD1 through the N-terminal region (ANKHD1 1-885 aa) containing the former 15 ANKs in vitro. Since ARDs are protein-protein interaction modules, some ARDs form homodimer (Pasquali et al., 2017). The dimerization of ANKHD1 is considered to be occurred by the 15 ANKs. Membrane vesiculation was caused by the latter 10 ANKs. ARDs often adopt curved conformations, and this feature is remarkable to a large number of ankyrin repeats such as Ankyrin-R that contains 24 ANKs (Wang et al., 2014). I expected that the ANKHD1 dimer had a curved structure and functioned as a scaffold for deformation of the lipid membrane. The predicted structure of the 10 ANKs suggested the surface abundant in the basic amino-acid residues, analogous to the membrane binding surface of BAR domains. Furthermore, ANKHD1 contains a possible amphipathic helix. Some BAR domains have amphipathic helices for membrane vesiculation (Boucrot et al., 2012). Therefore, it is reasonable that the ANKHD1 has membrane vesiculation and tubulation abilities (Figure 33).

Deletion of the amphipathic helix of N+ARD25 showed the weak membrane vesiculation, indicating the ARD of ANKHD1 has membrane vesiculation potential. N+ARD25 also has higher membrane vesiculation ability than ARD25. There are some reports that protein crowding cause membrane vesiculation and deformation by the high membrane coverage of proteins (Busch et al., 2015; Snead et al., 2017), suggesting the high molecular weight proteins with lipid binding ability might have membrane deformation ability for the large surface area to the membrane compared with small structured proteins. The molecular weight of the ARD25 dimer is about 260 kDa, and that of the N+ARD25 dimer is about 340 kDa. Higher membrane vesiculation by N+ARD25 might be due to protein crowding. My study also demonstrated that the vesiculation of liposomes were detected by the ARDs containing fragments of ANKRD17 and ANKFY1, which are high molecular weight protein over 100 kDa. Therefore, by increasing the protein concentration, other ARDs containing fragments, which did not show membrane vesiculation at 1μM in Figure 8, might display membrane vesiculation.

In case of ENTH domain (1-164 aa) of Epsin 1, the membrane vesiculation is caused by the amphipathic helix insertion at ratio of 1 helix to 200 lipids (Boucrot et al., 2012). The low density of the amphipathic helix is sufficient for membrane vesiculation. The area of membrane binding surface of the ENTH domain is equivalent to an area of 20 lipids (Boucrot et al., 2012), and the percentage of membrane coverage is 50% for the production of 20 nm vesicles by the ENTH domain (Snead et al., 2017), suggesting about 30 molecules of the ENTH domain are required for membrane vesiculation. Therefore, 2 or 4 molecules of ANKHD1 (1-2542 aa) might be enough for vesicle formation duo to its large molecular weight, which is about 15-fold higher than that of the ENTH domain.

4-2. Regulation of the membrane scission by ANKHD1

The ARD of ANKHD1 vesiculated liposomes composed of PC, PE, and PS. The K1323E-K1324E and R1357E-K1358E mutations in the 10 ANKs, that were considered to reduce the electrostatic interactions to the negatively charged lipids, decreased vesiculation of the liposomes. Deletion of the amphipathic helix adjacent to the 10 ANKs was considered to diminish the amphipathic helix insertion into the lipid bilayer, decreasing vesiculation of the liposomes.

Membrane lipid compositions differ in organelles between inner and outer leaflets by the asymmetric distributions of lipids. The different lipid compositions are considered to be required for spatial-temporal regulation of the binding of cytosolic lipid-binding proteins. The reductions of the membrane vesiculation by the K1323E-K1324E and R1357E-K1358E mutations suggest that the membrane vesiculation by ANKHD1 may be regulated by PS-rich membrane in budding compartment of early endosome.

The membrane fission by ANKHD1 for vesicle formation in vitro is thought to be independent of ATP or GTP hydrolysis. Some studies have reported several examples of protein-mediated vesiculation of lipid membrane without ATP or GTP hydrolysis in vitro. The BAR proteins containing amphipathic helices, including endophilin, vesiculate lipid membrane in vitro (Boucrot et al., 2012; Gallop et al., 2006; Masuda et al., 2006), presumably due to mechanical force applied to membrane (Simunovic et al., 2017). Membrane scission by ANKHD1 might be caused in combination with mechanical forces, which include the forces resulting from the medium flow in vitro and the motor proteins in cells.

The dimeric ANKHD1 functions as a membrane scission protein in vitro. However, whether ANKHD1 appeares in cells as heterodimer or homodimer for membrane scission of early endosome is not examined in my study. The membrane scission of ANKHD1 might be regulated by other protein through protein-protein interaction, resulting in decrease in the vesiculation of early endosome membrane by the inhibition of the dimeric ANKHD1.

4-3. Regulation of the early endosome enlargement by the membrane vesiculation ability of ANKHD1

The EEA1-positive early endosomes were increased in ANKHD1 knockdown cells, consistent with the increase in the amount of endogenous EEA1. Further, I found that the increase of Rab5 recruited the endogenous ANKHD1 to early endosome. Therefore, it is reasonable to consider that early endosomes are the place of ANKHD1 function.

However, the localization of ANKHD1 on early endosomes did not clearly occur with all ANKHD1. If ANKHD1 mediated membrane fission, it is possible that the localization of ANKHD1 at the early endosome was limited. The membrane scission protein such as dynamin and ESCRT often do not localize strongly at the target organelles (Gautreau et al., 2014; Lee et al., 2016; Schiel et al., 2012).

Early endosomes accompany the continuous homotypic fusion of endocytic vesicles. After the homotypic fusion, the Rab5-positive tubules of early endosome are generated, and then the tubules are finally deformed into vesicles by membrane scission (Skjeldal et al., 2012). However, the membrane fission proteins at the tubules positive for Rab5 in early endosome are unknown. ANKHD1 might involve in the membrane scission. The observation that the Rab5Q79L-positive early endosomes were enlarged by ANKHD1 knockdown indicates that ANKHD1 mediates membrane scission of early endosomes with activated Rab5. Because Rab5-positive early endosomes are enlarged by the constitutive activation of Rab5, further increase in the area of early endosomes induced by the downregulation of ANKHD1 indicated that membrane vesiculation by ANKHD1 negatively regulated fusion-mediated early endosome enlargement.

4-4. Budding compartment of early endosome in ANKHD1-mediated membrane scission

Rab5-localized early endosomes are converted into Rab7-localized late endosomes, and then fuse to lysosomes (Rink et al., 2005). The observation of lysosomes stained with Lysotracker indicated that early endosome maturation to late endosomes/lysosomes was not affected by ANKHD1, because the Lysotracker staining remained unchanged in ANKHD1 siRNA-treated cells.

The early endosome vesicles, which are formed by vesiculation, are transported to recycling endosomes, plasma membrane, and trans-Golgi. Rab5 does not localize in the budding compartment of early endosomes for trafficking to these organelles (Bonifacino and Rojas, 2006; Grant and Donaldson, 2009; Maxfield and

McGraw, 2004; Naslavsky and Caplan, 2011; Sönnichsen et al., 2000). Hence, ANKHD1-mediated vesiculation of early endosomes might be involved in unknown vesicle transport pathways, which might affect mitochondria because the total area of mitochondria was decreased in ANKHD1 siRNA-treated cells. Alternatively, because ANKHD1 partially colocalizes with Rab5 and EEA1, early endosome vesicles generated by ANKHD1 could be transported to plasma membrane or recycling endosomes, which contain abundant PS (Chen et al., 2010; Lee et al., 2015; Uchida et al., 2011; Xu et al., 2013).

4-5. Possible function of ANKHD1 in Hippo pathway

Hippo pathway regulates apoptosis and cell proliferation. When the hippo pathway is inactive, ANKHD1 binds to Yes associated protein (YAP) to induce cell proliferation in nucleus (Machado-Neto et al., 2014; Sansores-Garcia et al., 2013; Sidor et al., 2013). When the Hippo pathway is activated, ANKHD1 is transferred into the cytoplasm, and then apoptosis is induced (Sansores-Garcia et al., 2013; Sidor et al., 2013). The early endosome is involved in cell proliferation through a serine/threonine protein kinase (Akt) activation (Masters et al., 2017; Schenck et al., 2008). Akt inhibits Hippo pathway signalling (Nishio et al., 2013) and is activated in EEA1-positive early endosome (Nazarewicz et al., 2011). My study showed that ANKHD1 regulated the number of EEA1-positive early endosome. It may be possible that ANKHD1 decreases EEA1-positive early endosome when the hippo pathway is activated, effectively inducing apoptosis because of inactivation of Akt through reduction of the number of EEA1-positive early endosome. Therefore, the behaviour of early endosomes by ANKHD1 in this study does not contradict to the known observations about ANKHD1.

The Hippo pathway might provide a connection between mitochondria and ANKHD1. In *Drosophila*, the homologue of human ANKHD1 is Mask. The loss of Mask induces mitophagy for the removal of damaged mitochondria, which is a type of autophagy (Zhu et al., 2015). The decrease in the quantity of mitochondria in ANKHD1 siRNA-depleted cells might have been caused by mitophagy.

The relation between early endosome and mitochondria have been reported. Endocytic proteins indirectly involve in the regulation of the size of mitochondria through mitochondrial membrane fission (Farmer et al., 2017), suggesting that the possible ANKHD1-mediated vesicles are transported from early endosomes to mitochondria. The interactions between endosomes and mitochondria also affect motility of endosomes (Das et al., 2016), suggesting the site of ANKHD1 function. The detailed functional analysis of ANKHD1 in cells are yet to be determined.

4-6. Conclusion

In my thesis, I showed that ANKHD1 had membrane vesiculation and deformation abilities in vitro. ANKHD1 contains the first 15 ANKs, the latter 10 ANKs, and the amphipathic helix adjacent to the latter 10 ANKs. I found that the dimerization of ANKHD1 was required for the 15 ANKs-containing region and the membrane vesiculation was caused by the predicted curved structure of the 10 ANKs with the adjacent amphipathic helix, which is similar to the BAR domains with vesiculation ability.

The number and the size of early endosome are regulated by Rab5, which facilitates membrane fusion. I found that ANKHD1 regulated the number and size of early endosomes associated with Rab5 activation. The colocalization with ANKHD1 was enhanced by the activation of Rab5. Furthermore, Rab5-mediated enlargement of early endosomes was suppressed by the membrane vesiculation by ANKHD1. Also, ANKHD1 localized at the membrane fission sites of the early endosomes. Therefore, ANKHD1 negatively regulates the early endosome enlargement by the membrane vesiuclation.

My research suggests the possibility that some ARDs might have membrane deformation ability similar to that of ANKHD1. In membrane-deforming proteins, BAR domain is evolutionally conserved domain, however, other conserved domains with membrane deformation ability except for BAR domain and a few number of proteins have not been elucidated. Therefore, further study of ARDs may contribute to understanding of membrane tubulation and vesiculation in unknown process of various cellular events.

Figures

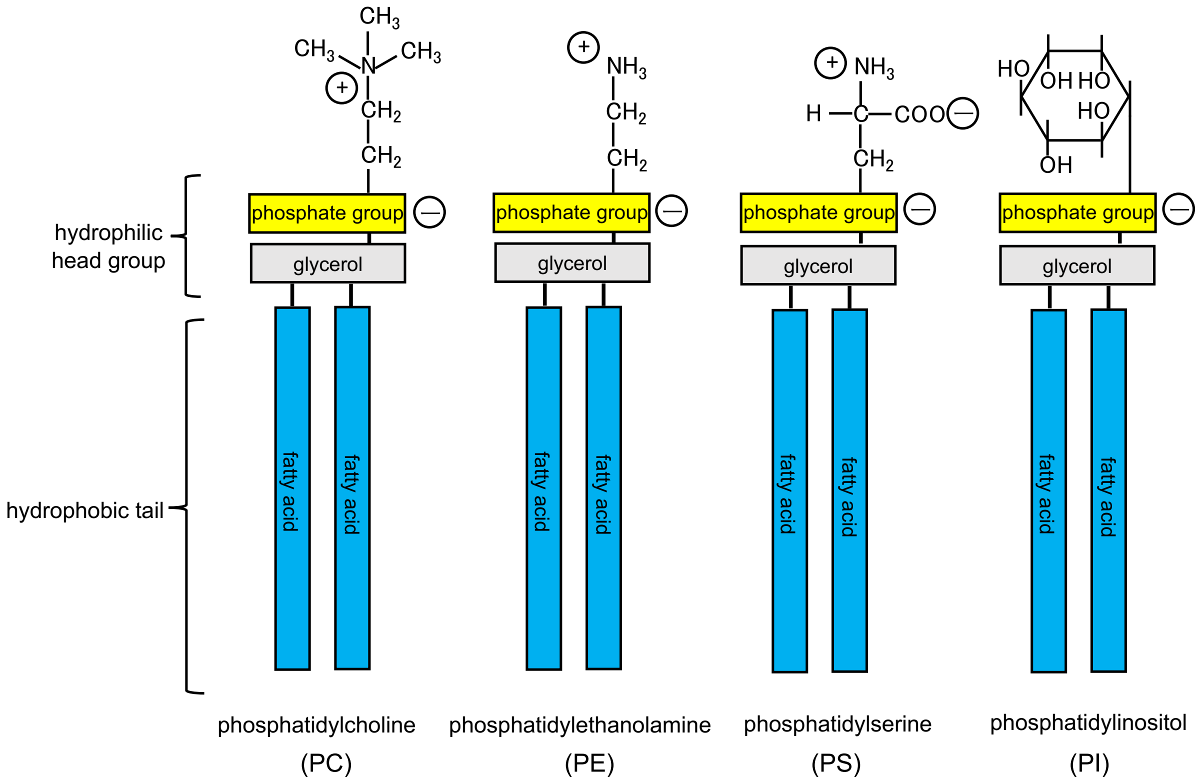

Figure 1. Major phospholipids in cell membrane

Four major phospholipids molecules are shown. These phospholipids are classified by different polar head groups. PC, PE, PS, and PI are phosphoglycerolipids. Only PS has a negative charge by its polar head in four phospholipids.

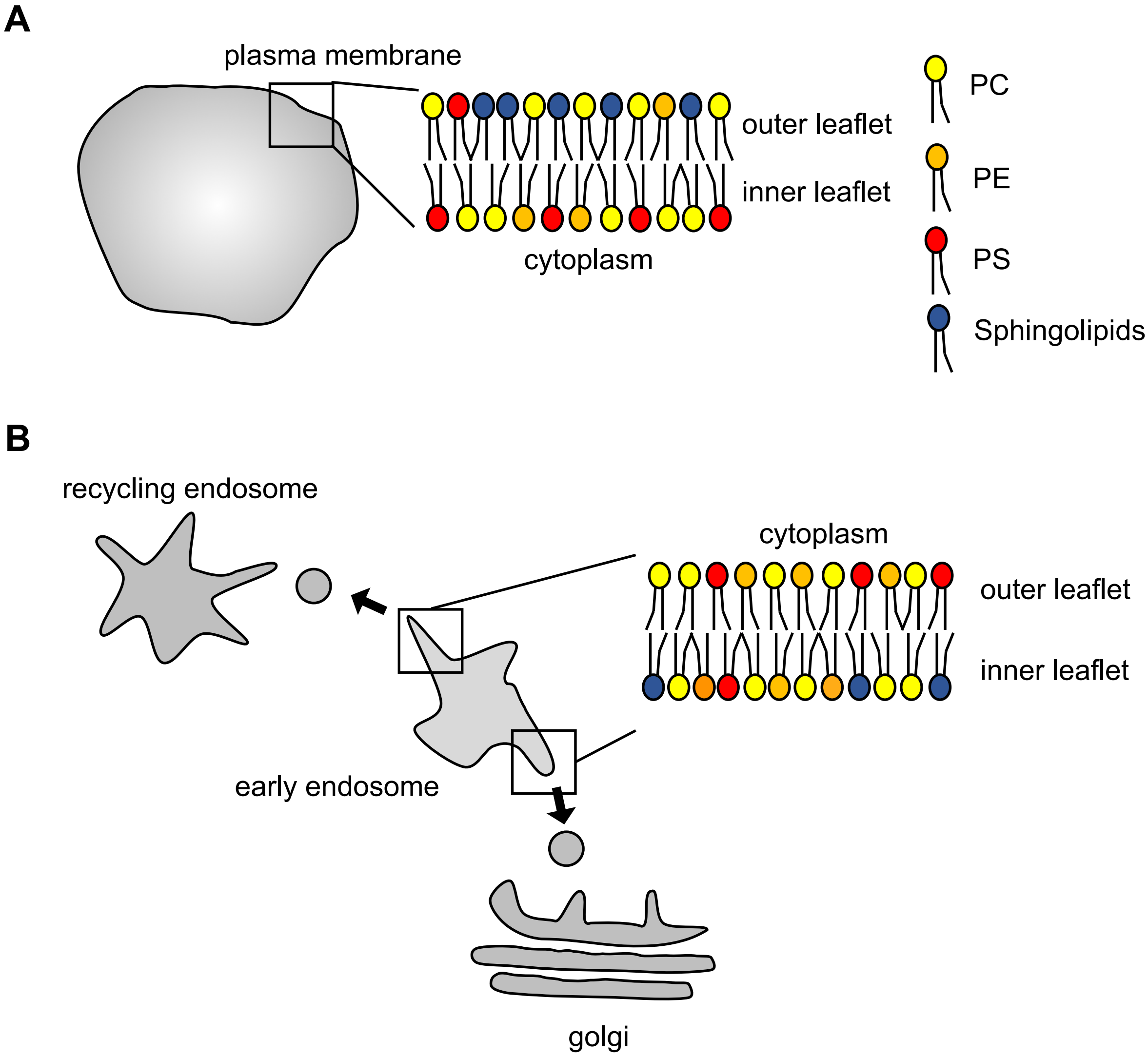

Figure 2. Asymmetric distributions of phospholipids in plasma membrane and early endosome

(A) The distributions of phospholipids and sphingolipids are different in plasma membrane. In plasma membrane, sphingolipids are predominantly localized in the outer leaflet while PE and PS are predominantly localized in the inner leaflet.

(B) In budding compartment of early endosome, PS is localized in outer leaflet. The asymmetric distribution has an important role for vesicle trafficking to recycling endosome and Golgi by membrane-deforming proteins.

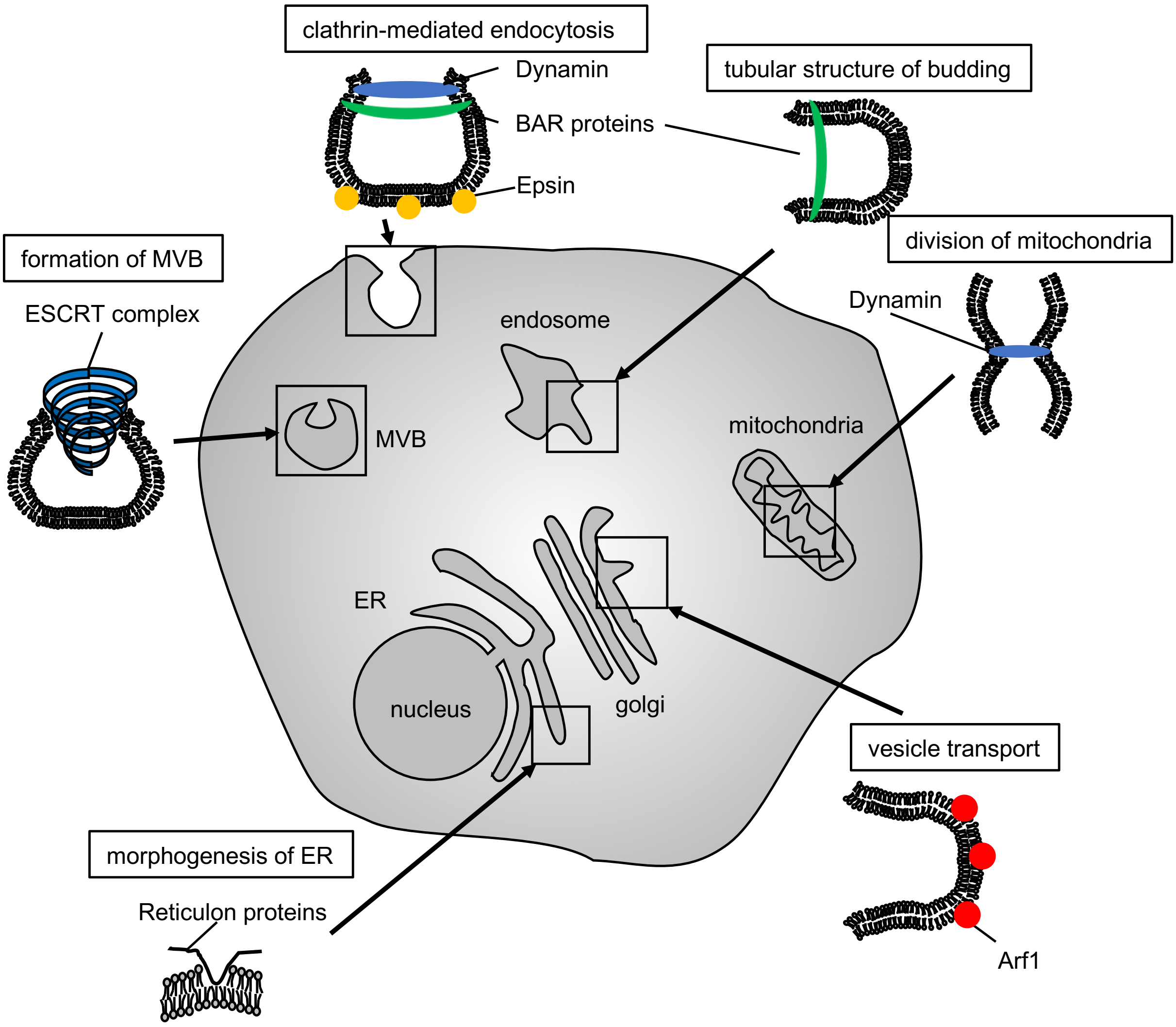

Figure 3. Membrane-deforming proteins in cell

Membrane-deforming proteins regulate the tubular membrane structure, membrane fission for vesicle formation (vesiculation), and organelle divisions. Typical membrane-deforming proteins in cell are shown.

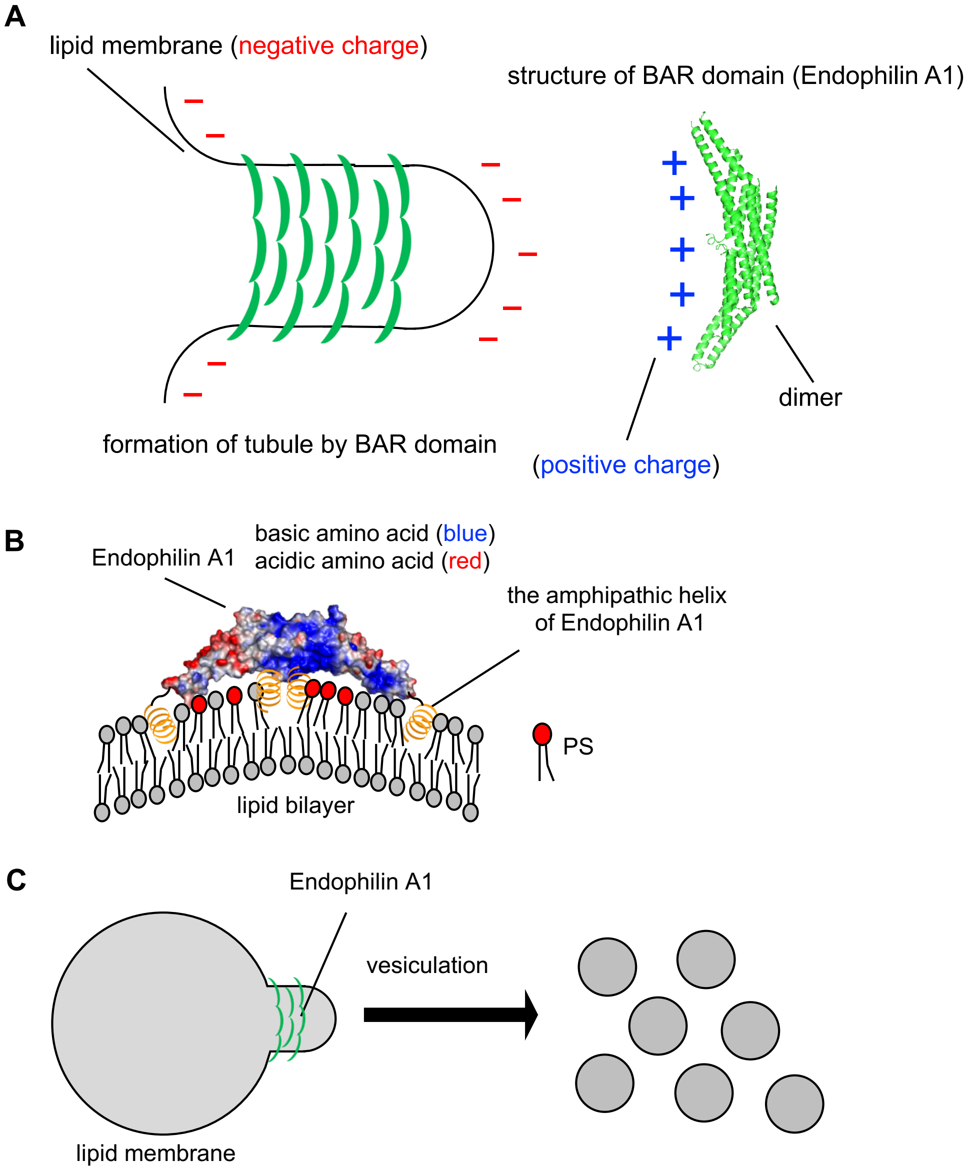

Figure 4. Tubulation and vesiculation by BAR domain

(A) BAR domain has positively charged surface and forms a curved structure. Lipid membrane containing negatively charged lipids such as PS is deformed into tubules that fit to the shape of the BAR domains.

(B) Endophilin A1 (PDB ID: 1zww) has amphipathic helices. The amphipathic helices are inserted into the hemilayer of the lipid membrane.

(C) Endophilin A1 induces vesiculation of the membrane by the amphipathic helix in vitro.

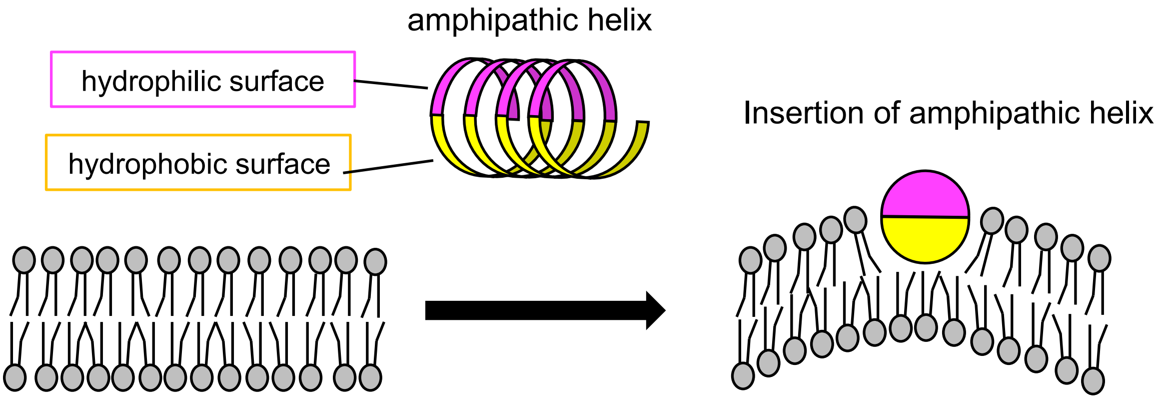

Figure 5. Insertion of amphipathic helix generates membrane curvature

The amphipathic helix constitutes hydrophilic and hydrophobic surface. Membrane curvature is regulated by the insertion of the hydrophobic surface into the hemilayer of the lipid membrane. The generation of membrane curvature results in formation of tubules and vesicles.

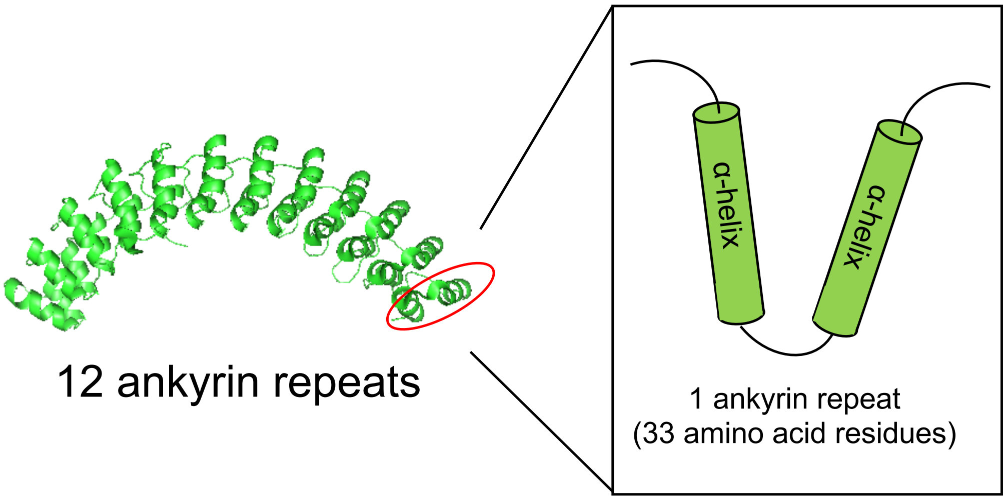

Figure 6. Structure of ARD

ARD is constituted of several ANKs. One ANK contains 33 amino-acid residues and forms two antiparallel α-helices. Crystal structure of 12 ANKs (no.13-24) of human AnkyrinR, which contains 24 ANKs, are shown (PDB ID: 1N11).

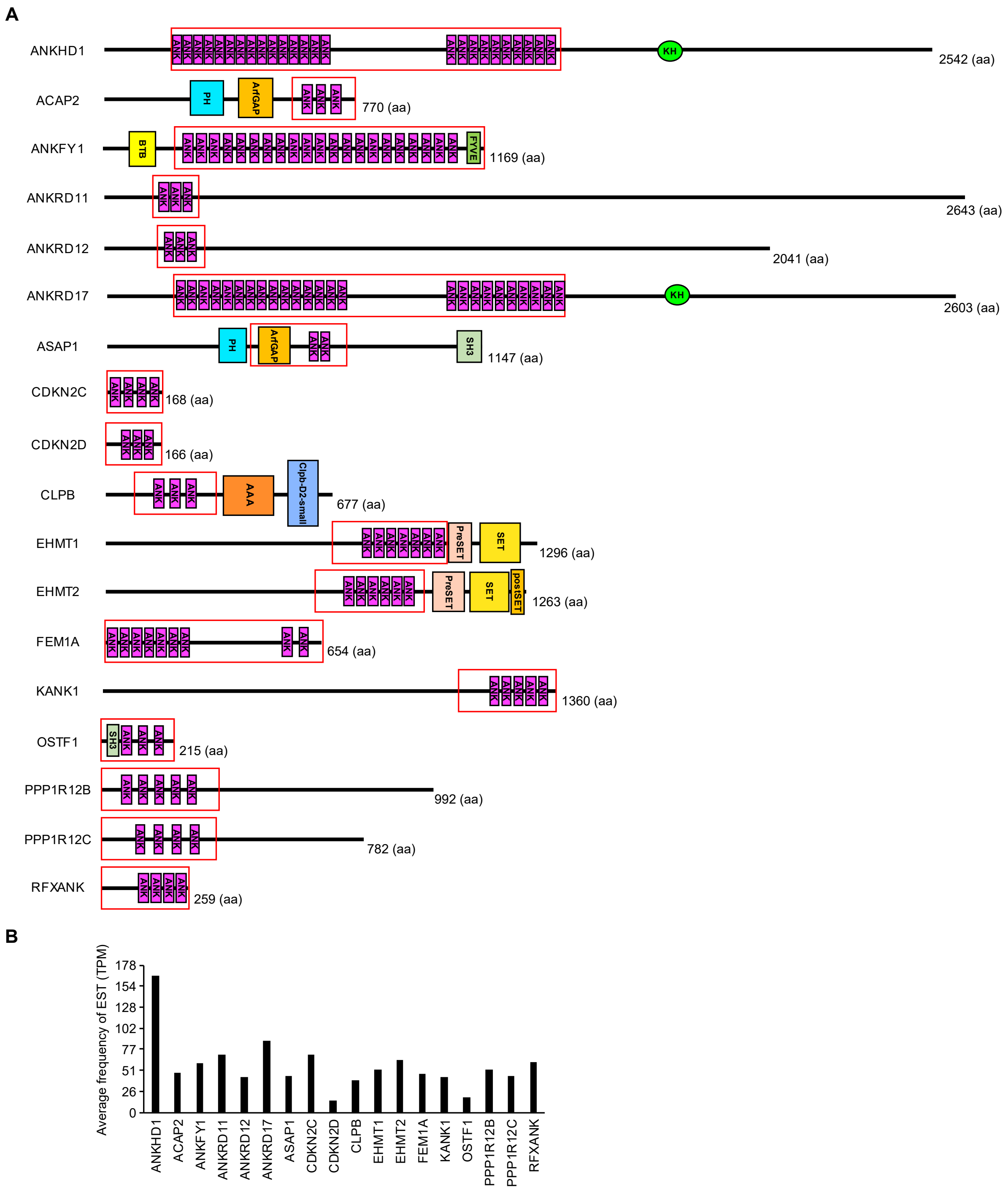

Figure 7. Domain structure of 18 ARD fragments and these human EST frequencies

(A) Illustration of the 18 ANK proteins. The 18 ARDs containing fragments, surrounded by red lines, were used in Figure 8.

(B) Average human EST frequencies (TPM: Transcripts per million) of the highly transcribed 18 ARD proteins among 78 organs/developmental stages/health states from the Unigene database (https://www.ncbi.nlm.nih.gov/unigene).

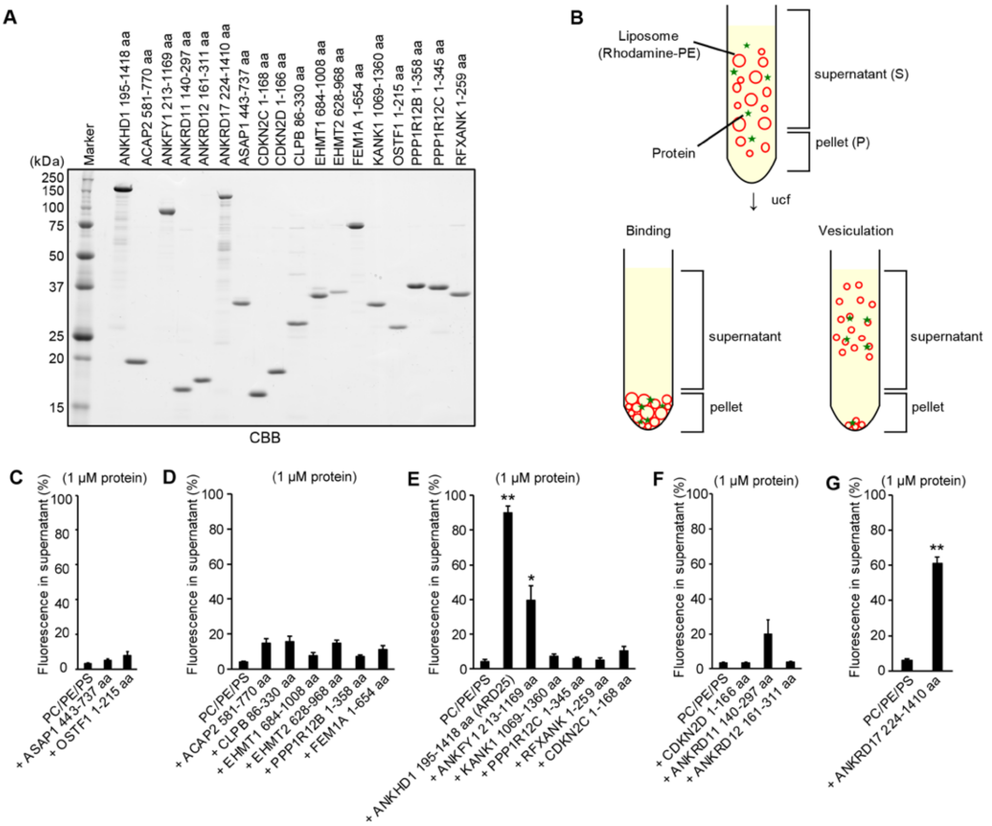

Figure 8. Identification of the ARD of ANKHD1 as a membrane vesiculation protein

(A) The purity of the 18 purified ARDs containing fragments was analyzed by SDS-PAGE. The gel was stained by CBB.

(B) Illustration of liposome sedimentation assay for membrane binding and vesiculation by proteins. The liposomes were labelled with rhodamine-PE, and the small liposomes vesiculated by proteins were not effectively precipitated after centrifugation at 109000 × *g*. Increase of vesiculated liposomes increased the fluorescence of rhodamine-PE in the supernatant. The supernatant (S) and the pellet (P) fractions were separated, and then analyzed by SDS-PAGE. The proteins and liposomes were visualized by CBB staining and Rhodamine fluorescence, respectively.

(C–G) Liposome sedimentation assay at 109000 × *g* for the 18 ARDs fragments at 1 μM. Liposomes were composed of 60% PC, 30% PE, and 10% PS and labelled with rhodamine-PE. The percentages of rhodamine-PE in the supernatant measured using ImageJ software are shown as the mean of three independent experiments. Error bars indicate SE. Student's *t*-test, $^{*}P < 0.05$ and $^{**}P < 0.01$.

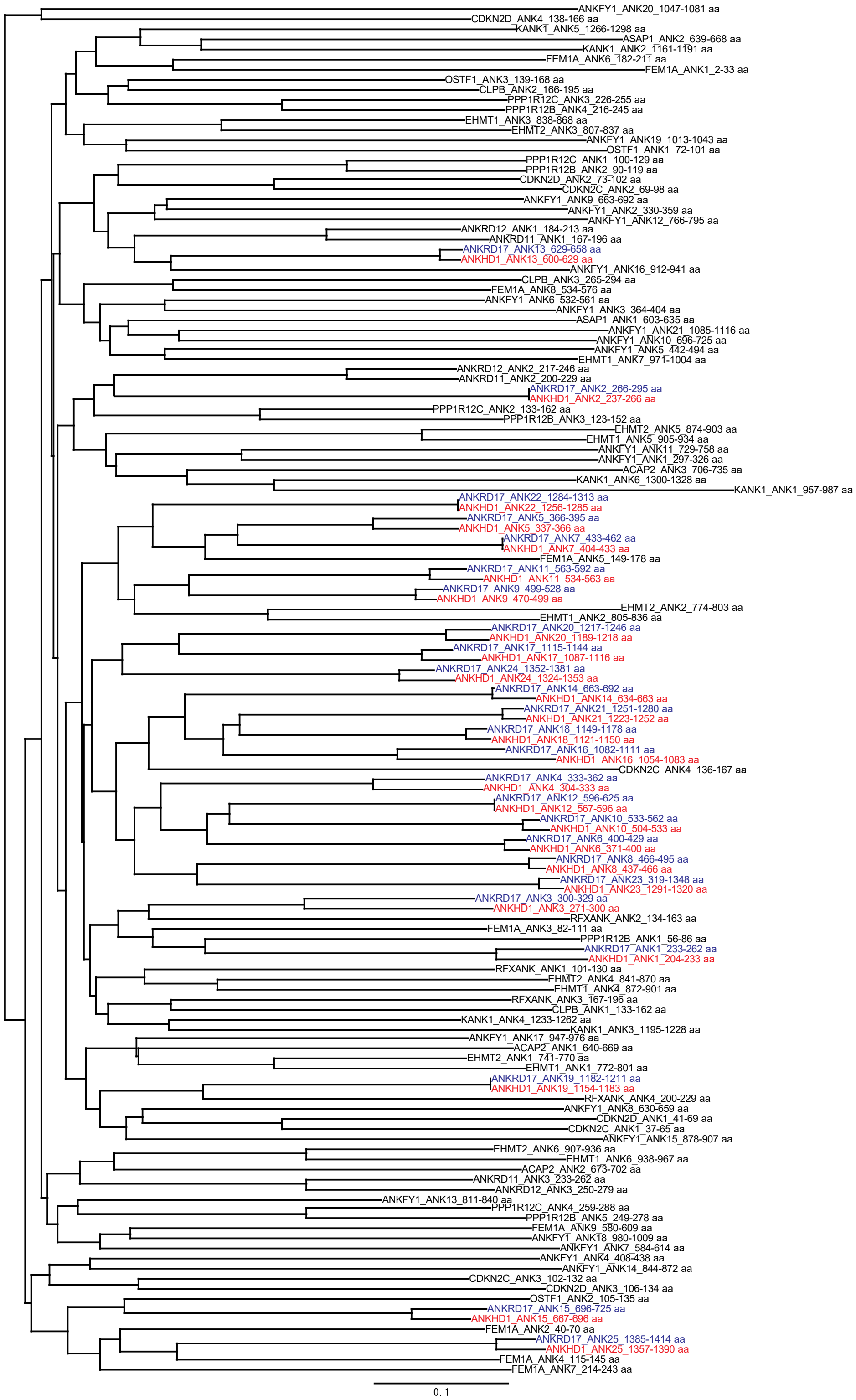

Figure 9. Phylogenetic tree of ANKs from the highly transcribed human 18 ARD proteins

Figure 9. ***Continued***

Phylogenetic tree of ANKs from the highly transcribed human 18 ARD proteins is shown. The amino acid sequences of the ANKs within each protein are compared in the human 18 ARD proteins. ANKHD1 and ANKRD17 are indicated as red and blue, respectively.

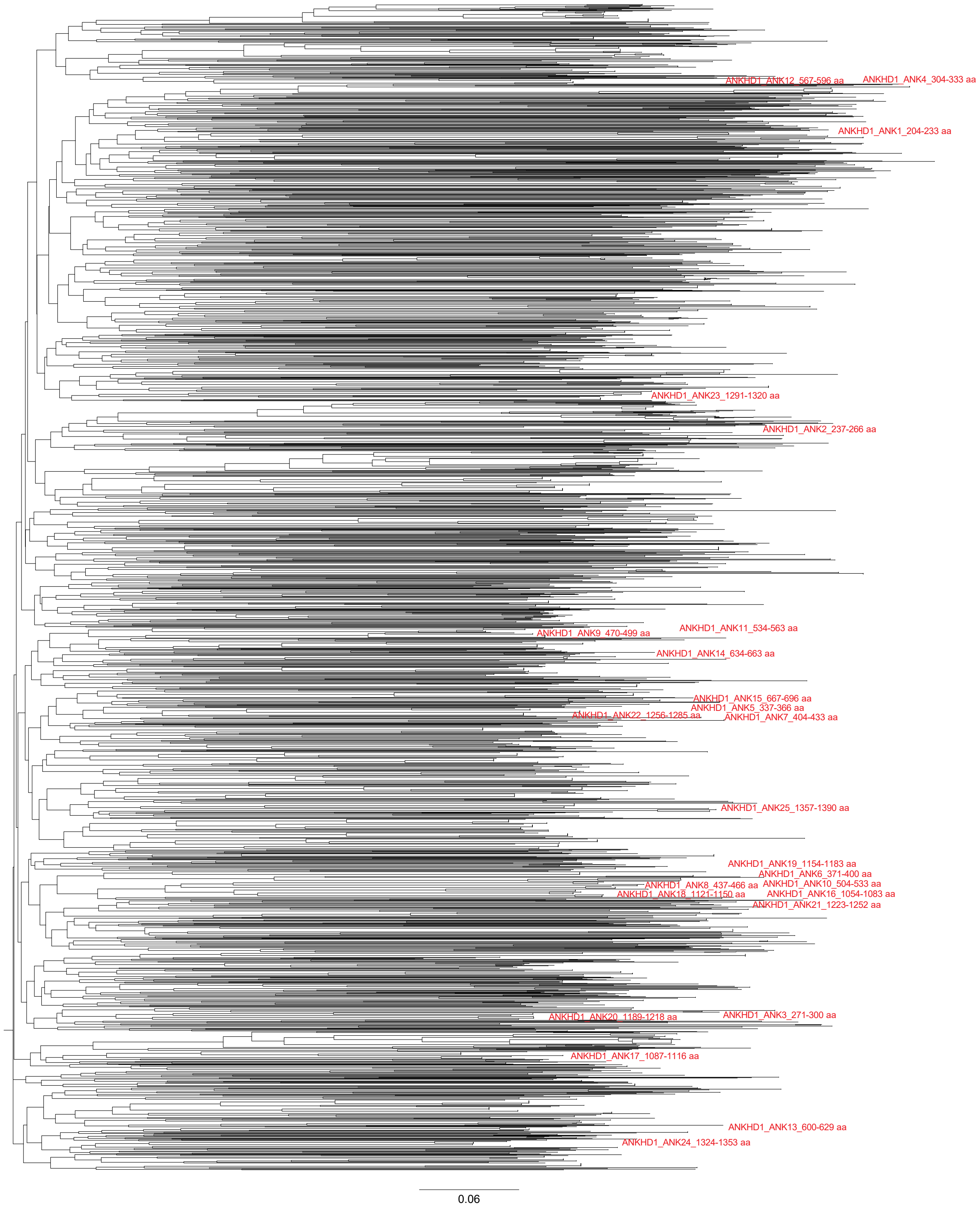

Figure 10. Phylogenetic tree of ANKs from all human ARD proteins

Figure 10. ***Continued***

Phylogenetic tree of ANKs of all human ARD proteins from SMART （http://smart.embl-heidelberg.de) is shown. The amino acid sequences of ANKs within each protein are compared in all human ARD proteins. Red indicates ANKHD1. The names of ARD-containing proteins other than ANKHD1 are not shown.

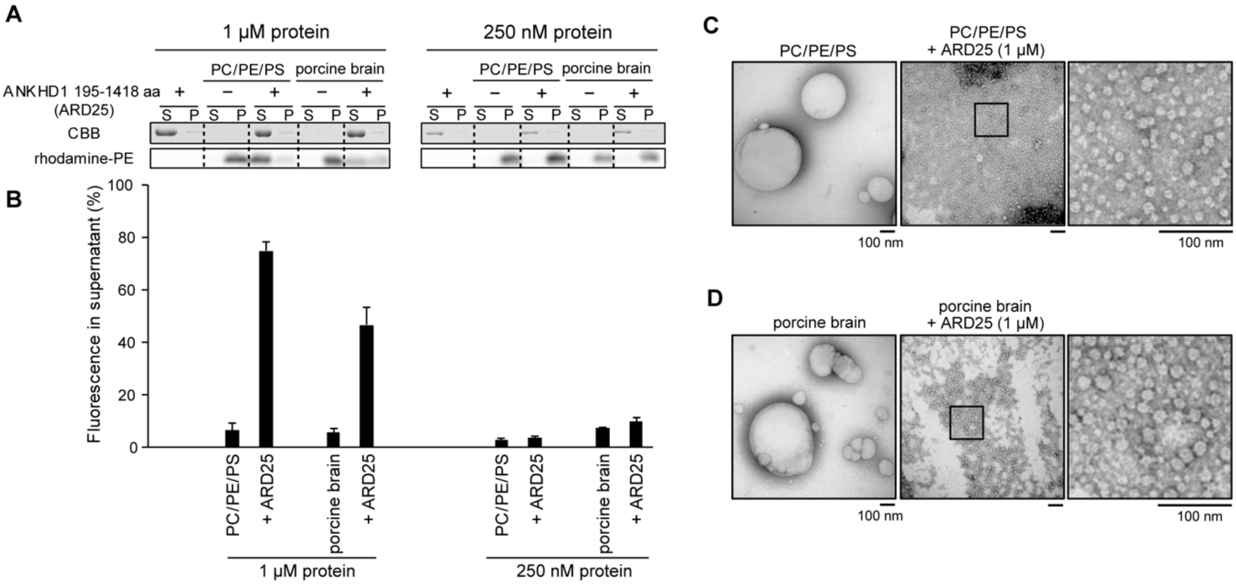

Figure 11. ANKHD1 vesiculates liposomes into small vesicles

(A) Liposome sedimentation assay for ARD25 (1 μM and 250 nM) using ultracentrifugation at 109000 × *g*. The liposome compositions were 60% PC, 30% PE, and 10% PS and brain lipids from porcine. The liposomes were labelled with rhodamine-PE.

(B) Percentages of Rhodamine-PE in the supernatants in (A) measured using ImageJ software are shown as the mean of four (1 μM protein) and three (250 nM protein) independent experiments. Error bars indicate SE.

(C-D) Electron micrographs of liposomes composed of 60% PC / 30% PE / 10% PS (C) and brain lipids from porcine (D) after incubation with ARD25 at 1 μM for 20 min. Negative staining visualized liposomes. Scale bars, 100 nm. The selected region presents an enlarged image.

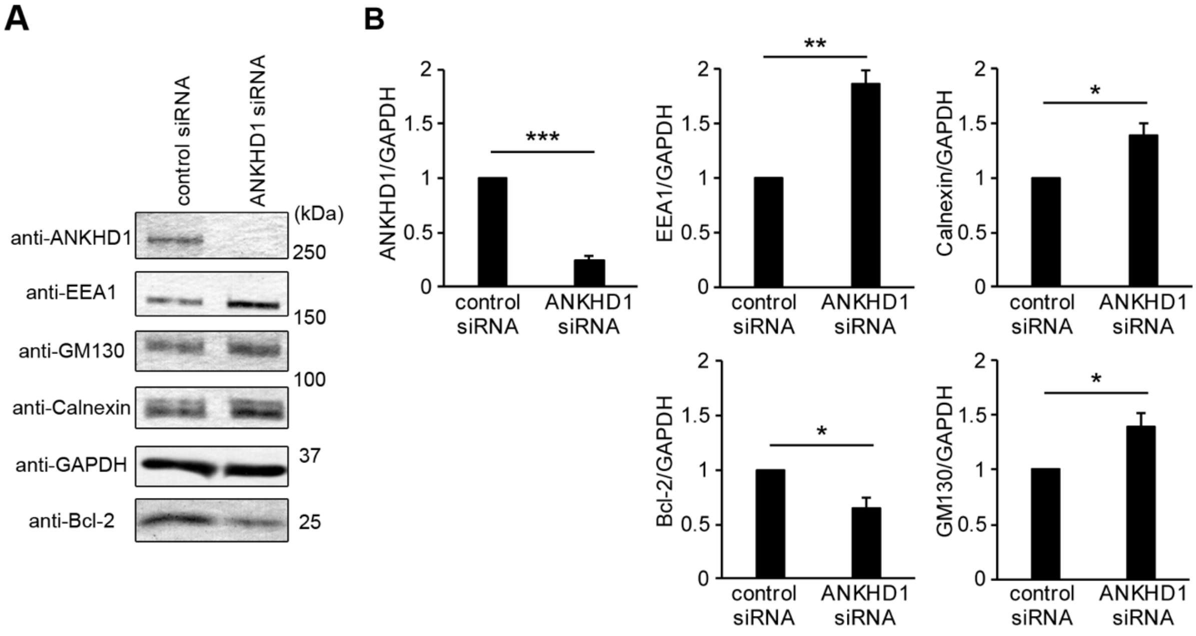

Figure 12. The amount of marker proteins for organelles in ANKHD1 siRNA-treated cells

(A) Effect of ANKHD1 siRNA on the amounts of organelle marker proteins, including EEA1 (early endosome), GM130 (cis-Golgi), Calnexin (ER), and Bcl-2 (mitochondria). Control siRNA or ANKHD1 siRNA were transfected into HeLa cells. The whole-cell lysates were analyzed by western blotting with the antibodies. Glyceraldehyde-3-phosphate dehydrogenase (GAPDH) was used as the loading control.

(B) Quantification of the signal intensities in (A). The intensities of these bands were quantified using ImageJ. Data are shown as the mean of five independent experiments. Error bars indicate SE. Student's *t*-test, **P* < 0.05, ***P* < 0.01, and ****P* < 0.001. ns, not significant.

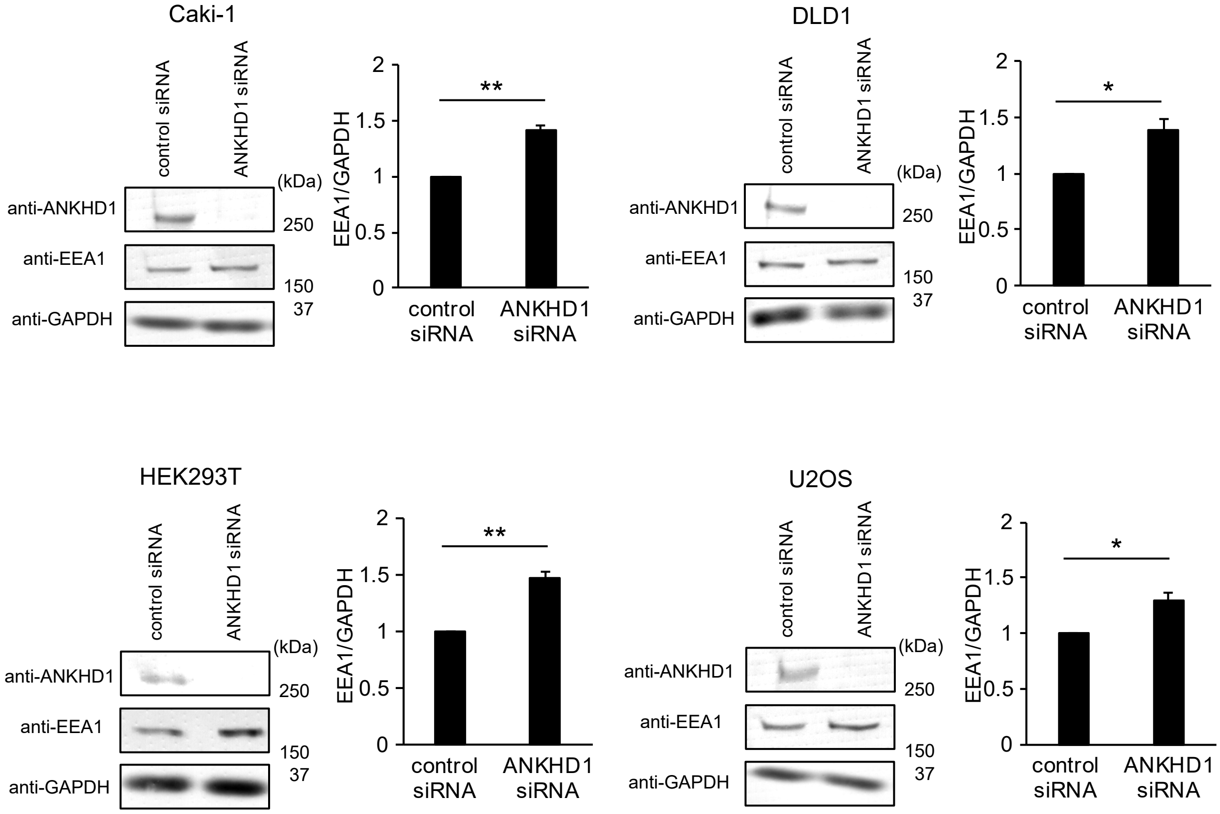

Figure 13. Increase in the amount of EEA1 in ANKHD1 knockdown cells

Effects of the treatment of ANKHD1 siRNA on the amount of endogenous EEA1 in Caki-1 cells, DLD1 cells, HEK293T cells, and U2OS cells. GAPDH was used as the loading control. The intensities of these bands were quantified using ImageJ. Data are shown as the mean of four independent experiments. Error bars indicate SE. Student's *t*-test, **P* < 0.05 and ***P* < 0.01.

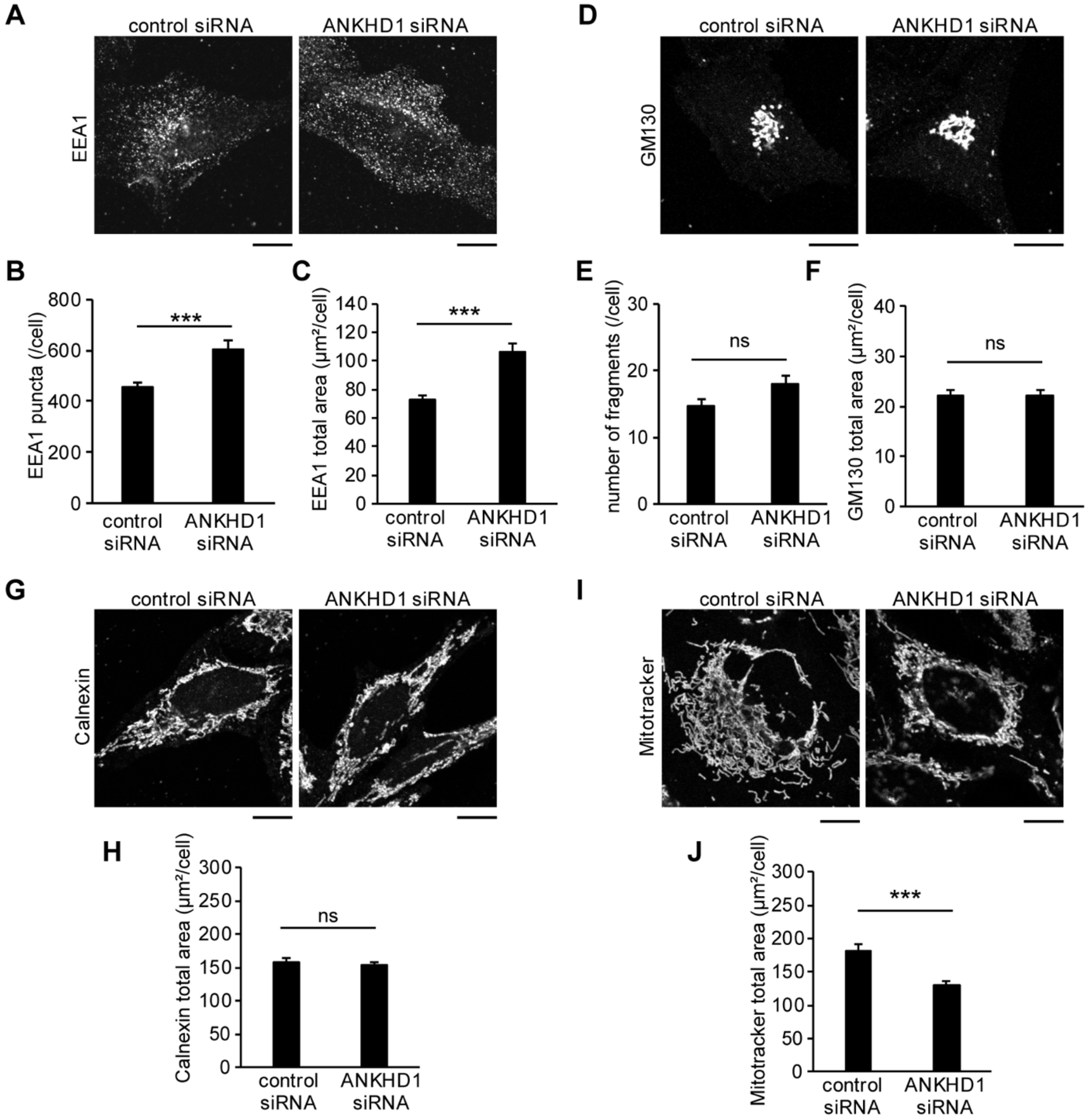

Figure 14. ANKHD1 knockdown increases EEA1-positive early endosome total area and decreases mitochondria total area

Figure 14. ***Continued***

(A) Representative images of endogenous EEA1 in control siRNA-treated HeLa cells and ANKHD1 siRNA-treated HeLa cells by confocal microscopy.

(B-C) The number of EEA1 puncta (B) and the total area of EEA1 staining (C) per cell in (A) were analyzed by ImageJ software. Data are shown as the mean of 43 and 42 cells in three independent experiments for control siRNA-treated cells and ANKHD1 siRNA-treated cells, respectively.

(D) Representative images of endogenous GM130 in control siRNA-treated HeLa cells and ANKHD1 siRNA-treated HeLa cells by confocal microscopy.

(E-F) The number of Golgi fragments (E) and the total area of GM130 staining (F) in (D) analyzed using ImageJ software as in (C) are shown as the mean of 68 and 78 cells in three independent experiments for control siRNA-treated cells and ANKHD1 siRNA-treated cells, respectively.

(G) Representative images of endogenous Calnexin in control siRNA-treated HeLa cells and ANKHD1 siRNA-treated HeLa cells by confocal microscopy.

(H) The total area of Calnexin staining in (G) analyzed using ImageJ software as in (C) are shown as the mean of 44 and 46 cells in three independent experiments for control siRNA-treated cells and ANKHD1 siRNA-treated cells, respectively.

(I) Representative images of mitochondria stained by using Mitotracker in control siRNA-treated HeLa cells and ANKHD1 siRNA-treated HeLa cells.

(J) The total area of Mitotracker staining in (I) analyzed by ImageJ software as in (C) are shown as the mean of 55 and 52 cells in three independent experiments for control siRNA-treated cells and ANKHD1 siRNA-treated cells, respectively.

All error bars indicate SE. Student’s *t*-test, $^{***}P < 0.001$. ns, not significant. Scale bars, 10 μm.

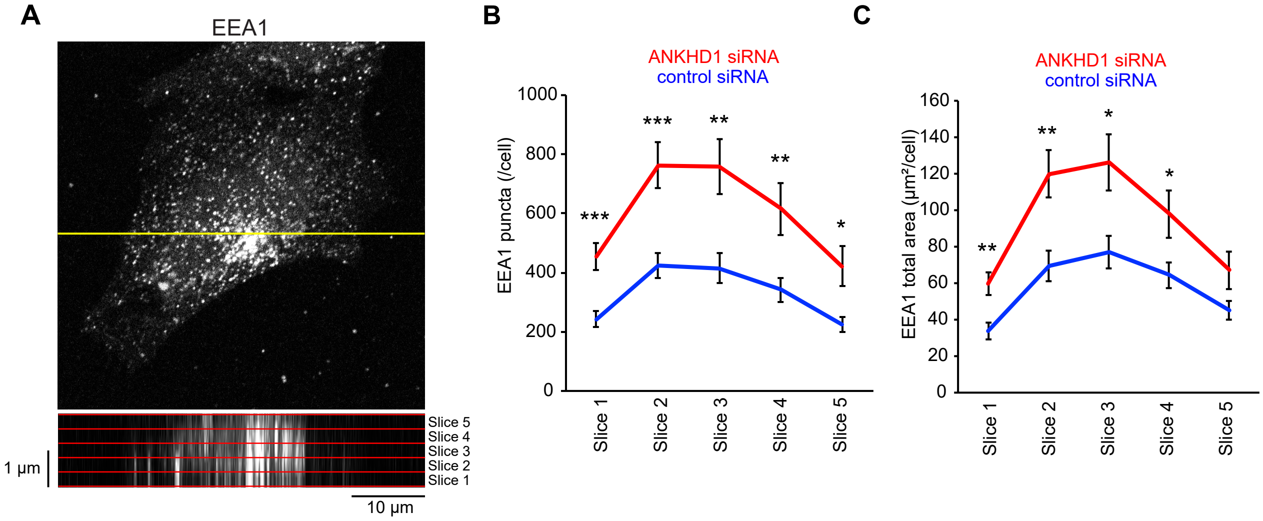

Figure 15. The number and the total area of EEA1-positive early endosomes at each focal plane upon ANKHD1 siRNA treatment

(A) The z-stack images of EEA1 puncta in HeLa cells by immunostaining. The lower panel is the z section at the yellow line in the upper panel. The z-stack images were acquired at 0.4 μm intervals by confocal microscopy for the measurement of the number of EEA1 puncta and the total area of EEA1 staining in each focal plane. The z axis was enlarged five times at the lower panel.

(B-C) The number of EEA1 puncta (B) and the total area of EEA1 staining (C) at each focal plane in HeLa cells treated with control or ANKHD1 siRNA were measured by ImageJ software. Confocal slices were acquired at 0.4 μm intervals. Data are shown as the mean of 14 cells. All error bars indicate SE. Student's *t*-test, $^{*}P < 0.05$, $^{**}P < 0.01$, and $^{***}P < 0.001$.

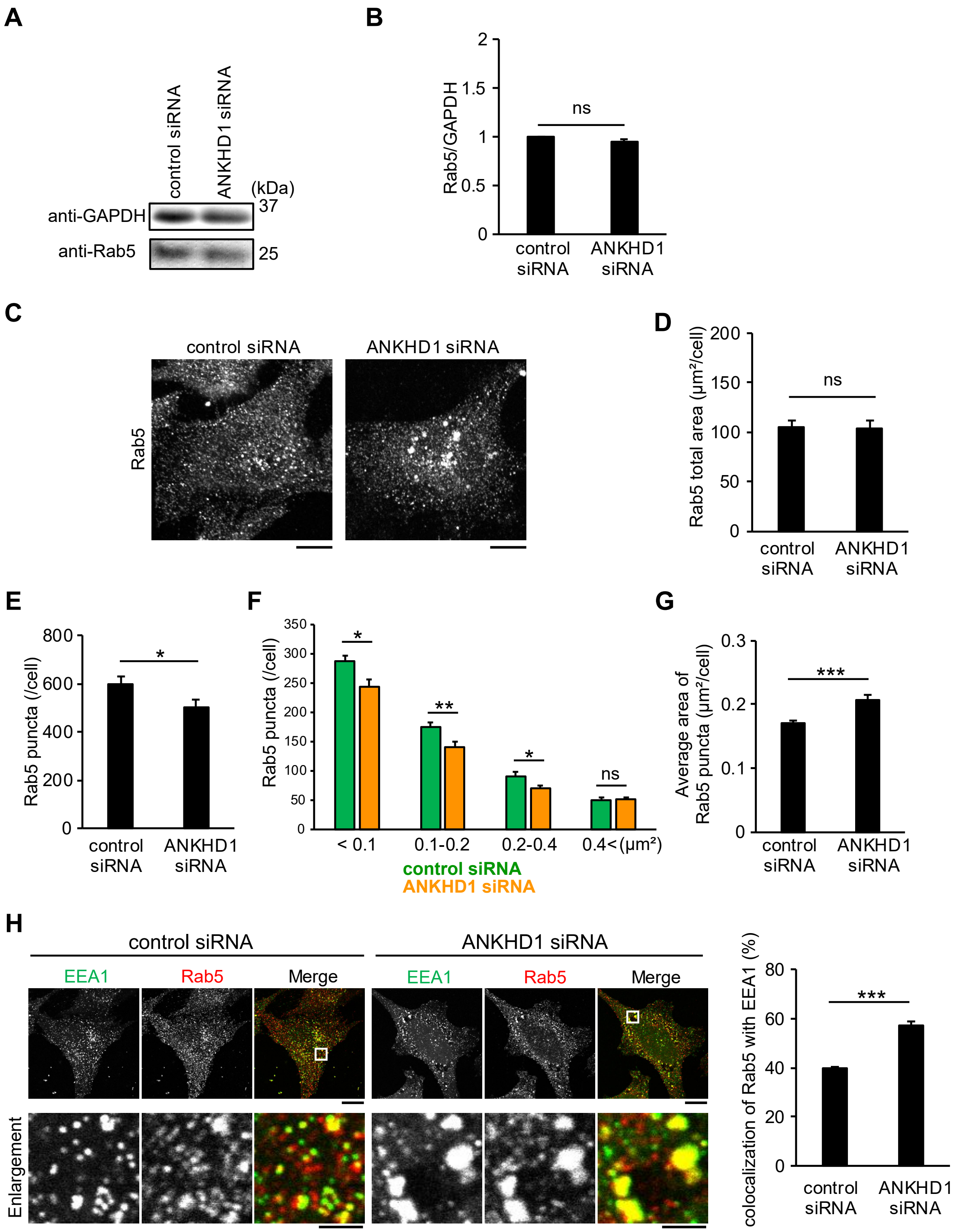

Figure 16. ANKHD1 knockdown increases the average size of Rab5-positive early endosomes and the colocalization of Rab5 with EEA1

Figure 16. ***Continued***

(A) Levels of endogenous Rab5 in HeLa cells upon control or ANKHD1 siRNA treatment by western blotting. GAPDH was used as the loading control.

(B) Quantification of Rab5 in (A). The intensities of these bands were quantified by ImageJ software. Data are shown as the mean of five independent experiments.

(C) Representative images of endogenous Rab5 in HeLa cells upon control or ANKHD1 siRNA treatment by confocal microscopy. Scale bars, 10 μm.

(D-G) The total area (D), the number (E), the size distribution (F), and the average area (G) of endogenous Rab5 in (C) analyzed by using ImageJ software are shown as the mean of 30 cells in three independent experiments for control siRNA-treated cells and ANKHD1 siRNA-treated cells.

(H) Colocalization percentages of endogenous Rab5 with endogenous EEA1 in control siRNA-treated HeLa cells and ANKHD1 siRNA-treated HeLa cells by confocal microscopy. Data are shown as the mean of 7 and 8 cells for control siRNA and ANKHD1 siRNA, respectively. Scale bars, 10 μm. Scale bars in magnification, 2 μm. All error bars indicate SE. Student's *t*-test, *$P < 0.05$, **$P < 0.01$, and ***$P < 0.001$. ns, not significant.

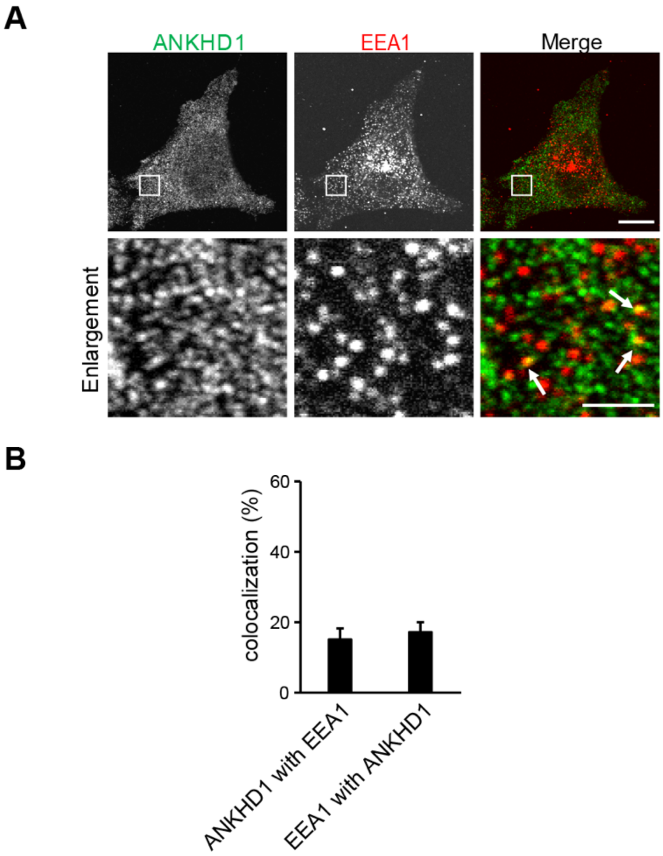

Figure 17. Localization of ANKHD1 on EEA1-positive early endosomes

(A) Representative images of endogenous ANKHD1 and EEA1 in HeLa cells by immunostaining. Arrows show colocalization of ANKHD1 and EEA1. The enlarged image of the selected region in the upper image is the lower image. Scale bars, 10 µm. Scale bars in magnification, 2 µm.

(B) Percentages of colocalization of ANKHD1 or EEA1 with EEA1 or ANKHD1, respectively, per cell in (A) analyzed by ImageJ software. Data are shown as the means of nine cells. Error bars indicate SE.

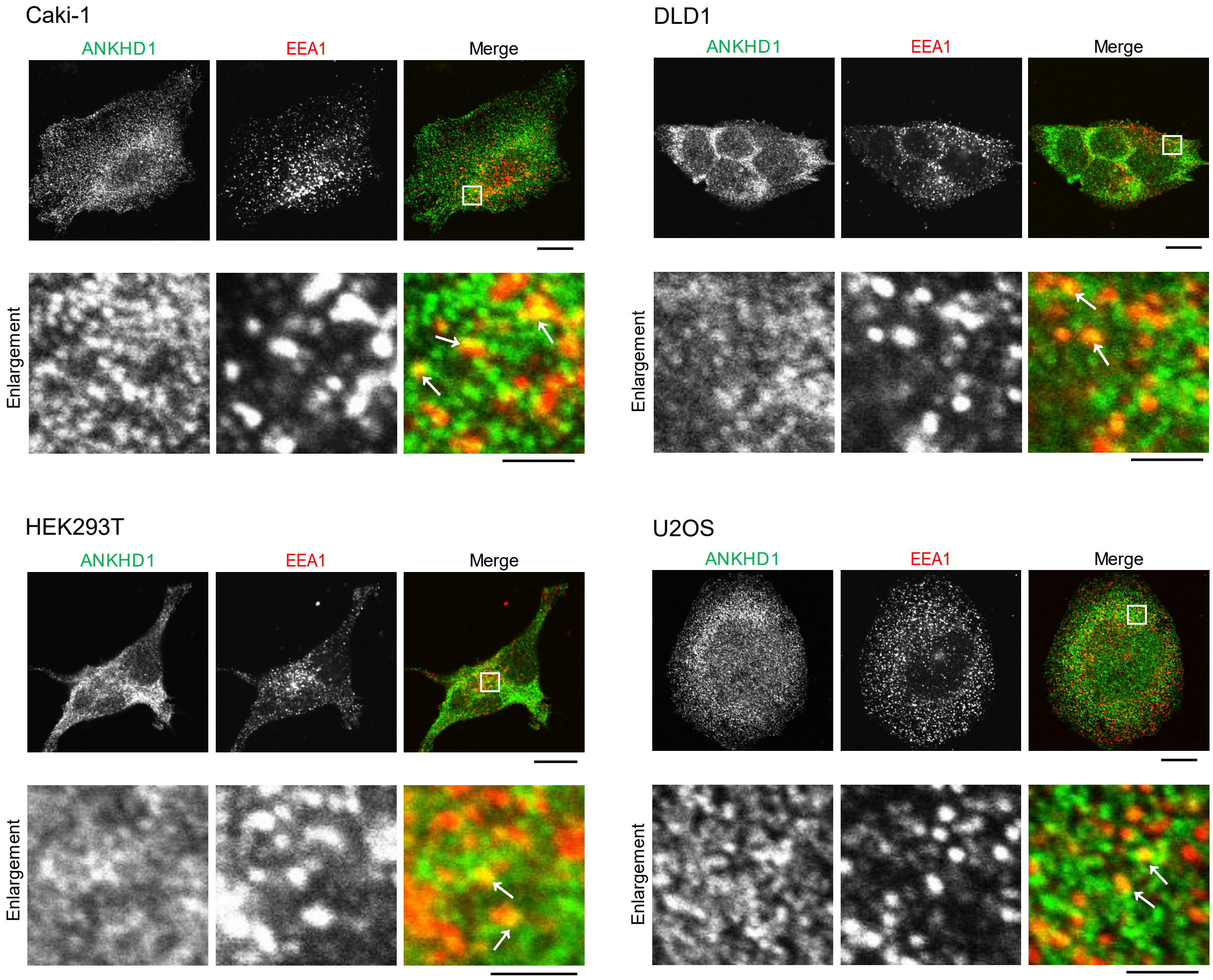

Figure 18. Localization of ANKHD1 on EEA1-positive early endosomes in Caki-1 cells, DLD1 cells, HEK293T cells, and U2OS cells

Representative images of endogenous ANKHD1 and EEA1 in Caki-1 cells, DLD1 cells, HEK293T cells, and U2OS cells by confocal microscopy. Arrows show colocalization of ANKHD1 and EEA1. Scale bars, 10 µm. Scale bars in magnification, 2 µm.

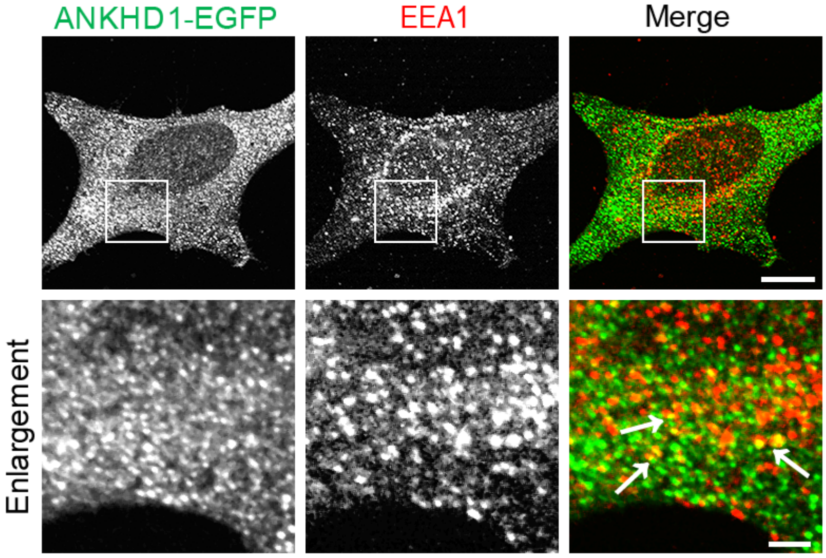

Figure 19. ANKHD1-EGFP localizes in EEA1-positive early endosomes

Confocal microscopy images of expressed ANKHD1 and endogenous EEA1 in HeLa cells by immunostaining. Arrows show colocalization of ANKHD1-EGFP and endogenous EEA1.

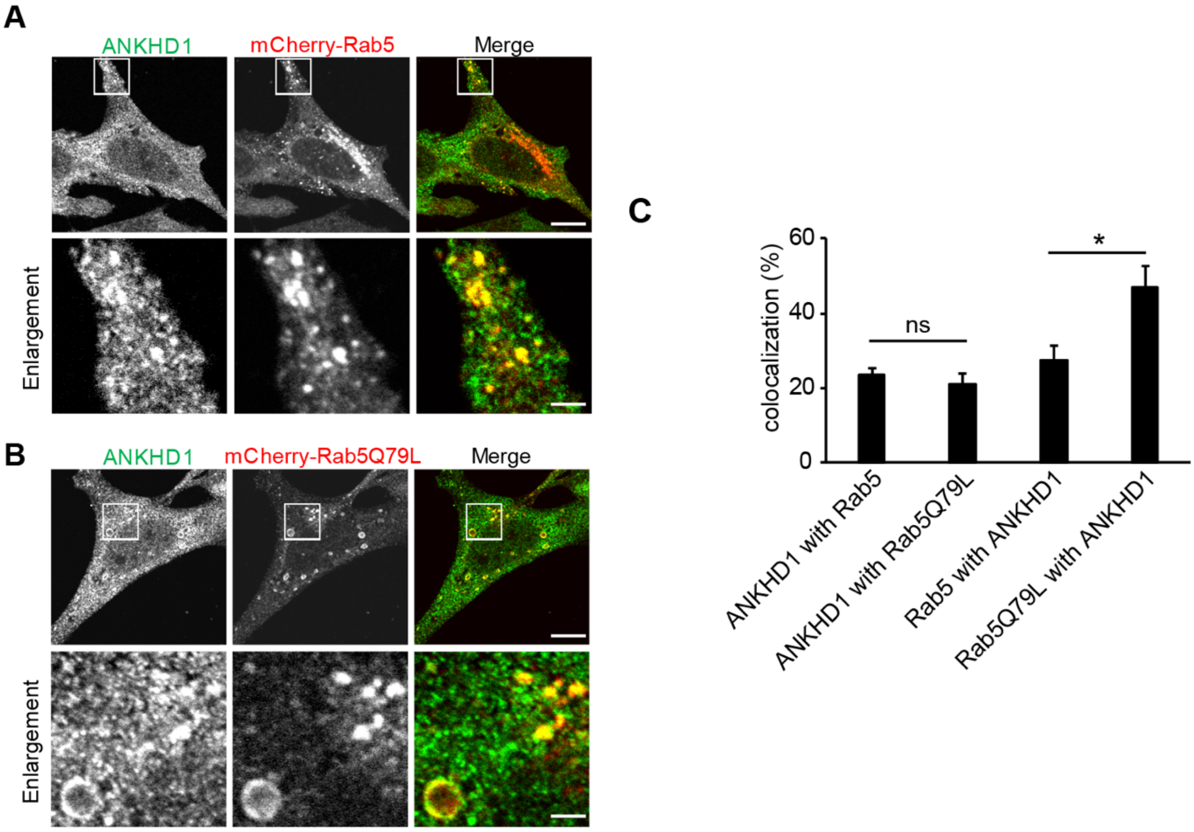

Figure 20. Localization of endogenous ANKHD1 on Rab5-positive early endosomes

(A and B) Representative images of endogenous ANKHD1 in HeLa cells expressing mCherry-Rab5 (A), or mCherry-Rab5Q79L (B) by confocal microscopy. Scale bars, 10 µm. Scale bars in magnification, 2 µm.

(C) Percentages of colocalization of endogenous ANKHD1 with mCherry-Rab5 or mCherry-Rab5Q79L and mCherry-Rab5 or mCherry-Rab5Q79L with endogenous ANKHD1 per cell in (A and B) calculated by ImageJ software. Data are shown as the mean of 10 and 11 cells expressing mCherry-Rab5 and mCherry-Rab5Q79L, respectively. Error bars represent SE. Student's *t*-test, $^*P < 0.05$. ns, not significant.

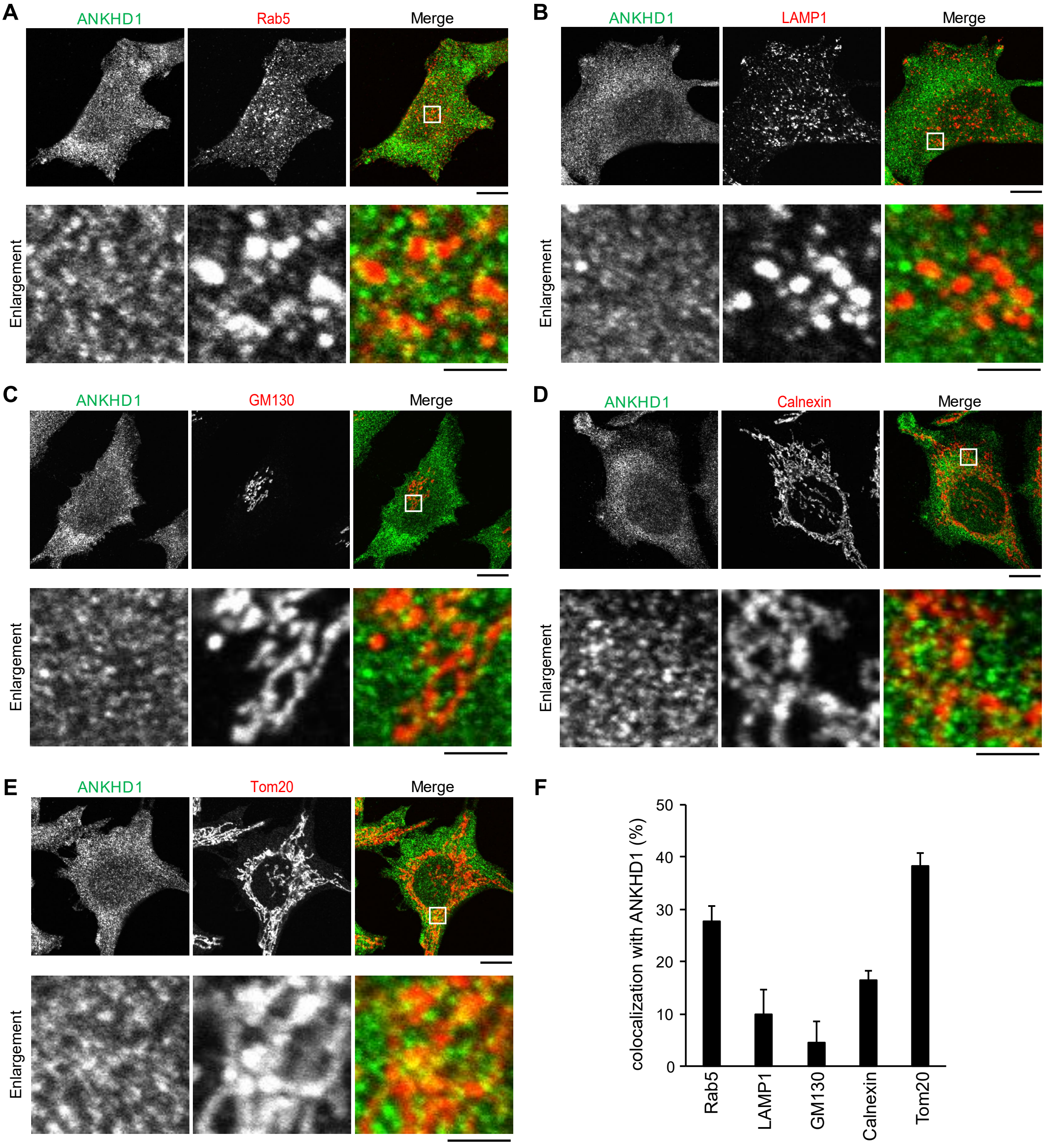

Figure 21. Localization of ANKHD1 in Rab5-positive early endosomes, late endosome/lysosomes, Golgi, ER, and mitochondria

Figure 21. ***Continued***

(A) Representative images of endogenous ANKHD1 and Rab5 in HeLa cells by immunostaining. The enlarged image of the selected region in the upper image is the lower image.

(B) Representative images of endogenous ANKHD1 and LAMP1 in HeLa cells by immunostaining.

(C) Representative images of endogenous ANKHD1 and GM130 in HeLa cells by immunostaining.

(D) Representative images of endogenous ANKHD1 and Calnexin in HeLa cells by immunostaining.

(E) Representative images of endogenous ANKHD1 and Tom20 in HeLa cells by immunostaining.

(F) Colocalization percentages of Rab5, LAMP1, GM130, Calnexin, or Tom20 with endogenous ANKHD1 per cell in (A-E) analyzed by ImageJ software. Data are shown as the means of 10 (A), 10 (B), 13 (C), 15 (D), and 12 (E) cells. Error bars represent SE. Scale bars, 10 μm. Scale bars in magnification, 2 μm.

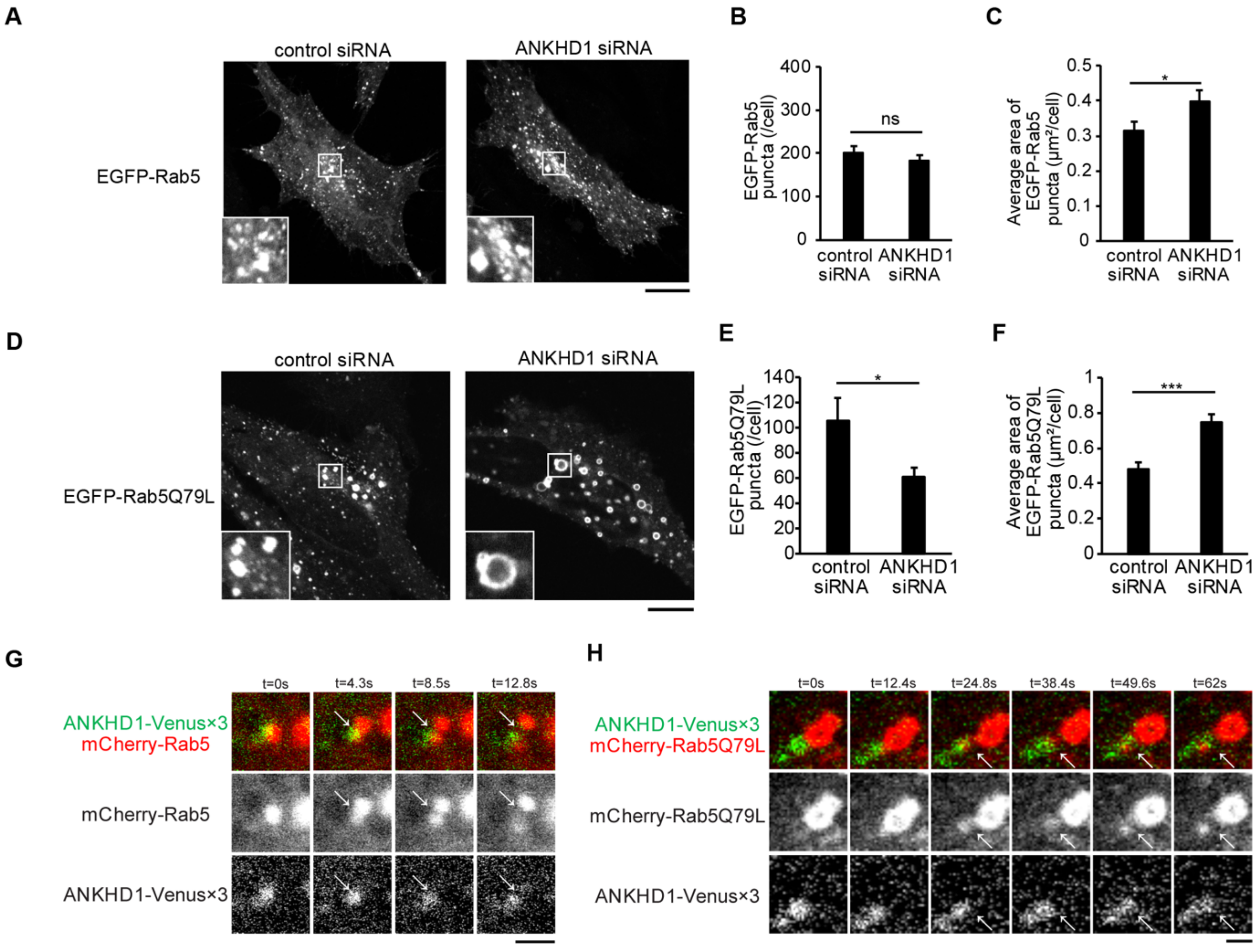

Figure 22. ANKHD1 regulates the size of Rab5-positive early endosomes and localizes at the membrane fission site

Figure 22. ***Continued***

(A) Representative images of expressed EGFP-Rab5 in control siRNA-treated HeLa cells and ANKHD1 siRNA-treated HeLa cells. Scale bars, 10 µm.

(B–C) The number (B) and the average area (C) of EGFP-Rab5 puncta per cell in (A) measured by ImageJ software are shown as the mean of 21 and 18 cells in three independent experiments for control siRNA-treated cells and ANKHD1 siRNA-treated cells, respectively.

(D) Representative images of expressed EGFP-Rab5Q79L in control siRNA-treated HeLa cells and ANKHD1 siRNA-treated HeLa cells. Scale bars, 10 µm.

(E–F) The number (E) and the average area (F) of EGFP-Rab5Q79L puncta per cell in (D) measured by ImageJ software are shown as the mean of 30 and 29 cells in three independent experiments for control siRNA-treated cells and ANKHD1 siRNA-treated cells, respectively.

(G) Live imaging of ANKHD1-depleted HeLa cells expressing ANKHD1-Venus×3 and mCherry-Rab5. Arrows show membrane fission of early endosome. Scale bar, 1 µm.

(H) Live imaging of ANKHD1-depleted HeLa cells expressing ANKHD1-Venus×3 and mCherry-Rab5Q79L. Arrows show membrane fission of early endosome. Scale bar, 1 µm.

All error bars indicate SE. Student's *t*-test, $*P < 0.05$ and $***P < 0.001$. ns, not significant.

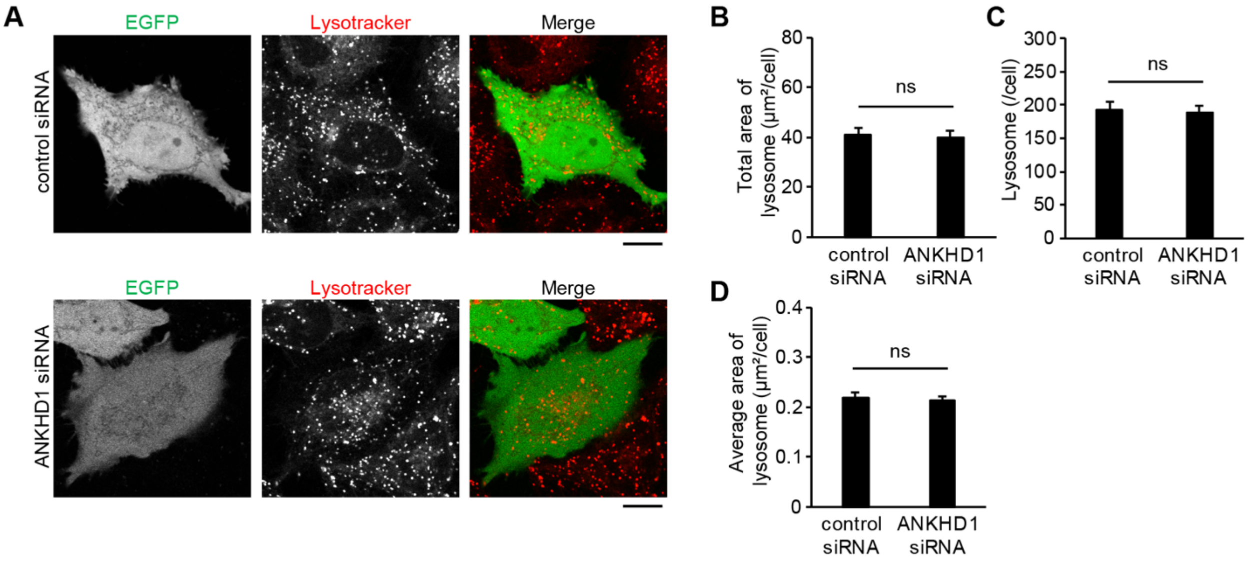

Figure 23. ANKHD1 knockdown does not affect maturation of early endosomes to late endosomes/lysosomes

(A) Representative images of lysosome morphology stained with Lysotracker in HeLa cells upon treatment with control or ANKHD1 siRNA. Scale bars, 10 μm.

(B-D) The total area (B), the number (C), and average area (D) of lysosomes per cell in (A) analyzed by ImageJ software are shown as the means of 26 and 25 cells in three independent experiments for control siRNA-treated cells and ANKHD1 siRNA-treated cells, respectively. Error bars indicate SE. Student’s *t*-test, ns, not significant.

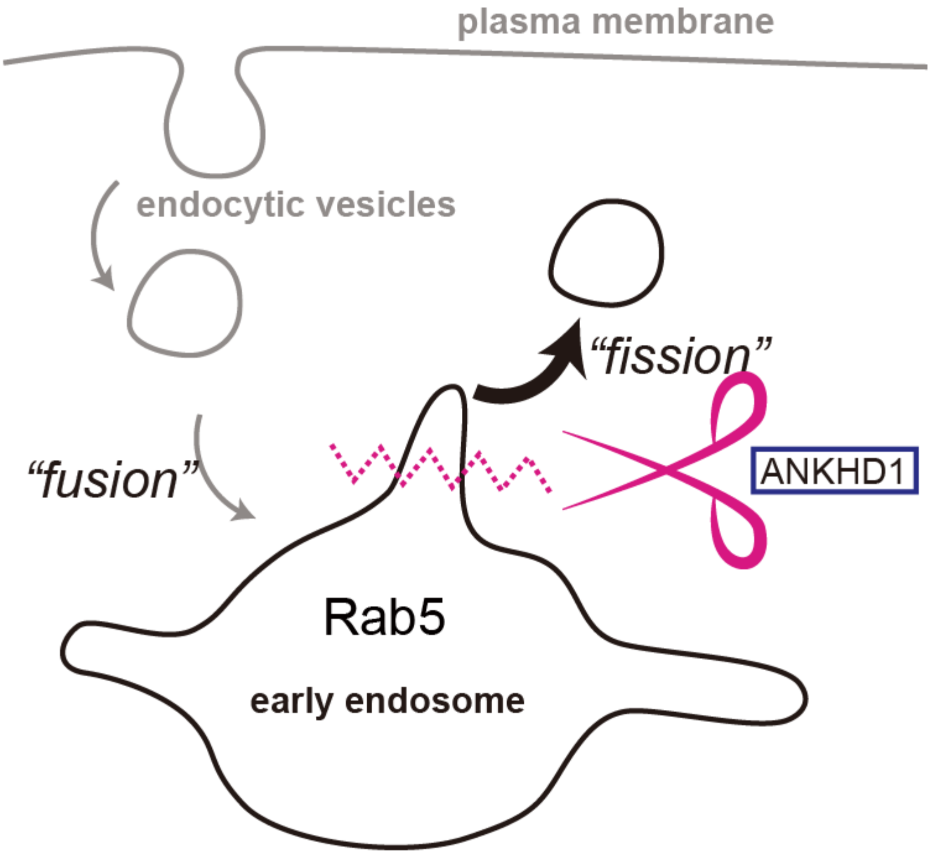

Figure 24. Proposed function of ANKHD1 on early endosomes

ANKHD1 mediates membrane scission of Rab5-positive early endosomes.

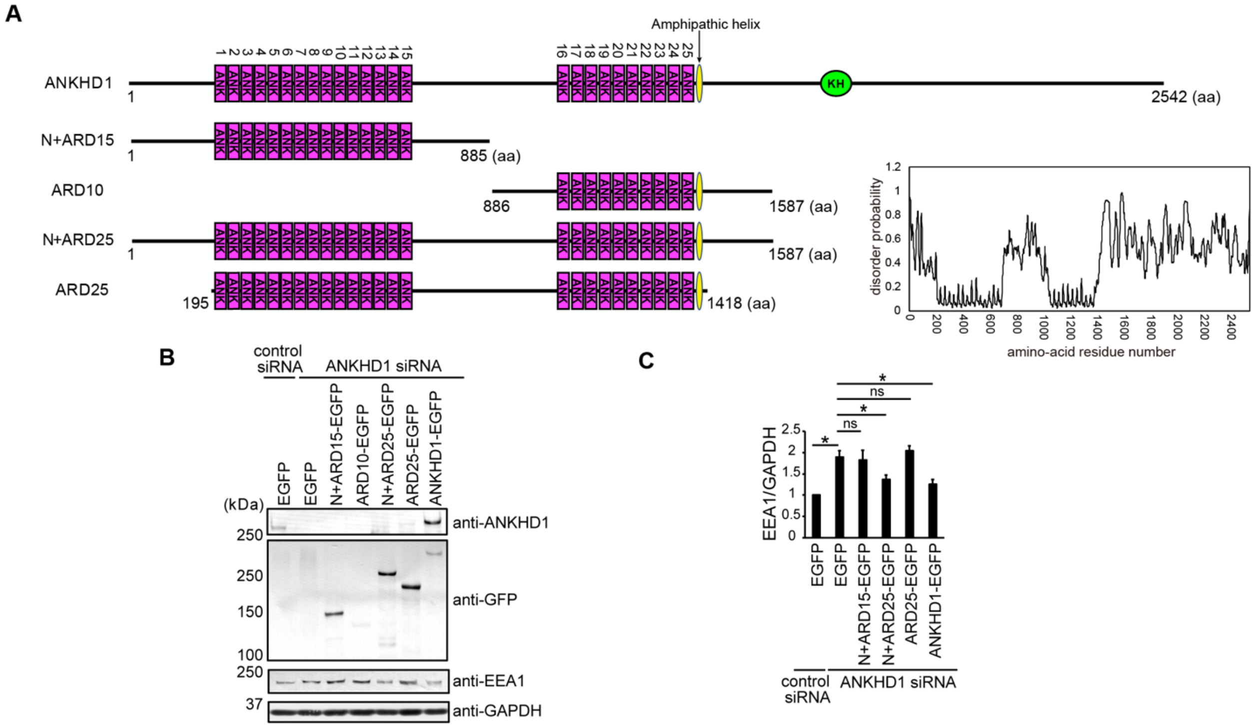

Figure 25. Effect of the ANKHD1 fragments on the amount of EEA1

(A) Illustration of human ANKHD1 (1-2542 aa) and the ANKHD1 fragments including ANKHD1 1-885 aa (N+ARD15), ANKHD1 886-1587 aa (ARD10), ANKHD1 1-1587 aa (N+ARD25), and ANKHD1 195-1418 aa (ARD25). ANKs, the amphipathic helix (1400-1415 aa), and the KH domain were shown. Disorder probability was calculated by PrDOS (http://prdos.hgc.jp).

(B) Amounts of endogenous EEA1, endogenous ANKHD1, and expressed ANKHD1 fragments in HeLa cells transfected with control siRNA + EGFP, ANKHD1 siRNA + EGFP, ANKHD1 siRNA + N+ARD15-EGFP, ANKHD1 siRNA + ARD10-EGFP, ANKHD1 siRNA + N+ARD25-EGFP, ANKHD1 siRNA + ARD25-EGFP, or ANKHD1 siRNA + ANKHD1-EGFP for rescue experiments by western blotting. GAPDH was used as the loading control.

(C) The signal intensities of EEA1 in (B) quantified by ImageJ software are shown as the mean of three independent experiments. Error bars indicate SE. Student's *t*-test, $^{**}P < 0.05$. ns, not significant.

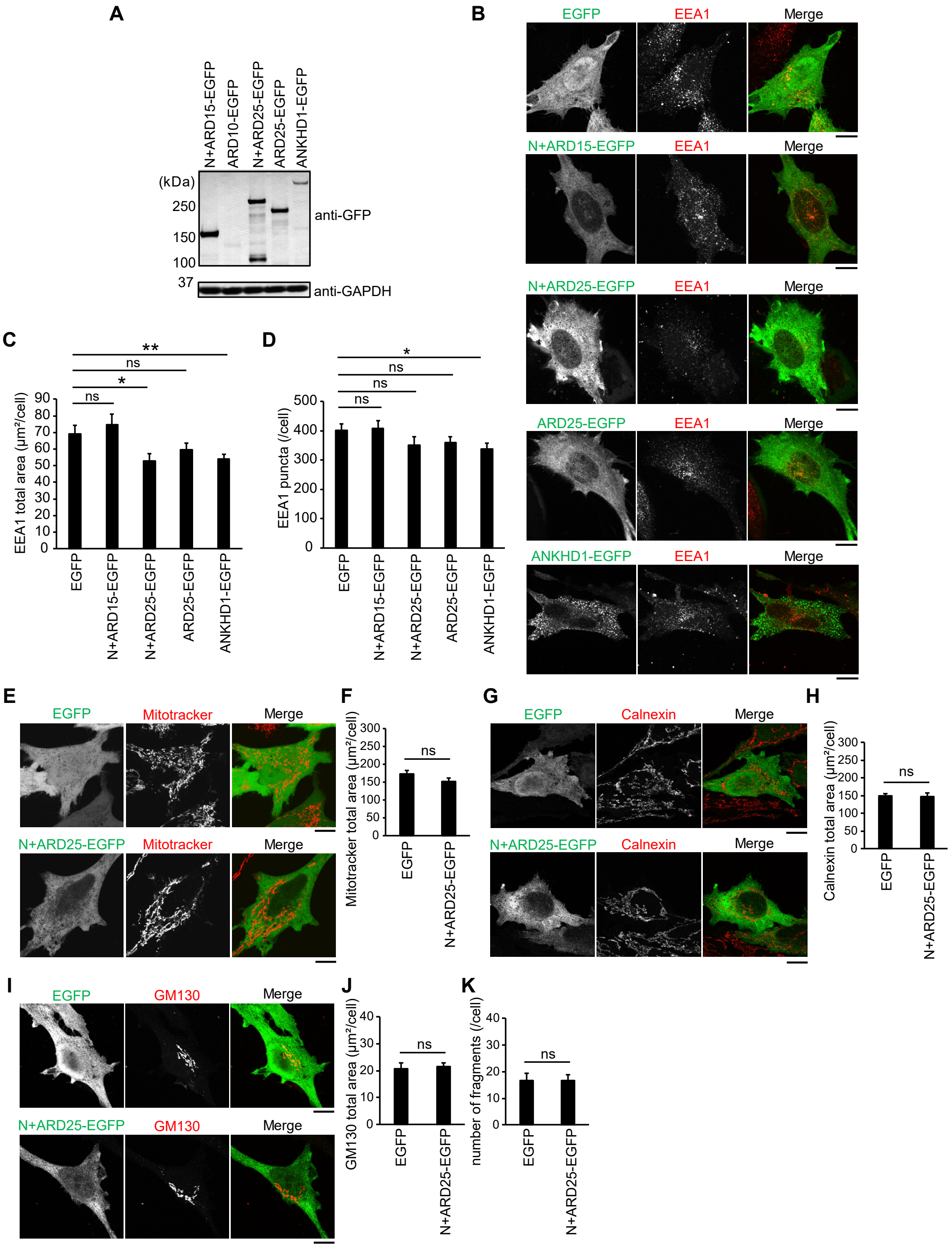

Figure 26. Effect of ANKHD1 fragments on the total area of EEA1-positive early endosomes, ER, mitochondria, and Golgi

Figure 26. ***Continued***

(A) Levels of expressed EGFP, N+ARD15-EGFP, ARD10-EGFP, N+ARD25-EGFP, ARD25-EGFP, and ANKHD1-EGFP in HeLa cells by western blotting.

(B) Representative images of endogenous EEA1 in HeLa cells expressing EGFP, N+ARD15-EGFP, N+ARD25-EGFP, ARD25-EGFP, or ANKHD1-EGFP by immunostaining.

(C-D) The total area of EEA1 staining (C) and number of EEA1 puncta (D) in (B) was analyzed by using ImageJ software. Data are shown as the mean of 25, 26, 25, 24, and 26 cells in three independent experiments for EGFP, N+ARD15, N+ARD25, ARD25, and ANKHD1, respectively.

(E) Representative images of mitochondria visualized by using Mitotracker in HeLa cells expressing EGFP or N+ARD25-EGFP.

(F) The total area of Mitotracker staining in (E) analyzed by using ImageJ software as in (C) are shown as the mean of 22 and 21 cells in three independent experiments for EGFP and N+ARD25, respectively.

(G) Representative images of endogenous Calnexin in HeLa cells expressing EGFP or N+ARD25-EGFP by immunostaining.

(H) The total area of Calnexin staining in (G) analyzed by using ImageJ software as in (C) are shown as the mean of 22 cells from three independent experiments for EGFP and N+ARD25.

(I) Representative images of endogenous GM130 in HeLa cells expressing EGFP or N+ARD25-EGFP by immunostaining.

(J-K) The total area (J) of GM130 staining analyzed using ImageJ software as in (C) and the number of Golgi fragments (K) in (I) are shown as the mean of 22 cells in three independent experiments for EGFP and N+ARD25.

All error bars indicate SE. Student's *t*-test, $*P < 0.05$ and $**P < 0.01$. ns, not significant. Scale bars, 10 µm

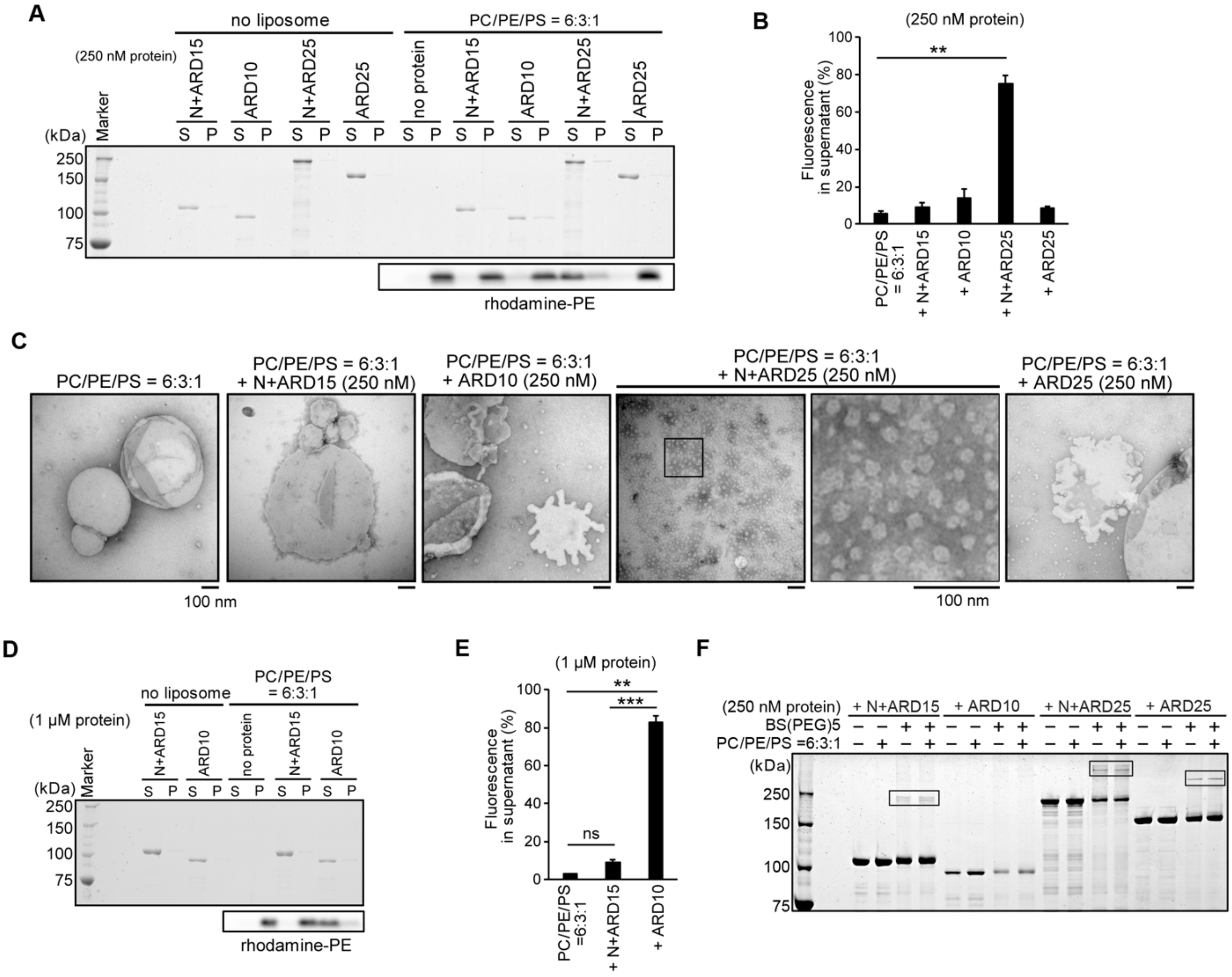

Figure 27. Dimeric ANKHD1 and the membrane vesiculation ability

Figure 27. ***Continued***

(A) Liposome sedimentation assay using ultracentrifugation at 109000 × *g* for N+ARD15, ARD10, N+ARD25, and ARD25 (250 nM). The liposome composition was 60% PC / 30% PE / 10% PS. The liposomes were labelled with rhodamine-PE.

(B) Quantification of liposomes in the supernatants in (A) measured using ImageJ software. Data are shown as the mean of three independent experiments.

(C) Electron micrographs of liposomes after incubation with N+ARD15, ARD10, N+ARD25, or ARD25 (250 nM) for 20 min. The liposome composition was 60% PC / 30% PE / 10% PS. Negative staining visualized liposomes. The selected region presents an enlarged image. Scale bars, 100 nm.

(D) Liposome sedimentation assay using ultracentrifugation at 109000 × *g* for N+ARD15 and ARD10 (1 μM). The liposome composition was 60% PC / 30% PE / 10% PS. The liposomes were labelled with rhodamine-PE.

(E) Quantification of liposomes in the supernatants in (D) measured using ImageJ software. Data are shown as the mean of three independent experiments.

(F) Crosslinking assay for N+ARD15, ARD10, N+ARD25, or ARD25. After incubation of ANKHD1 fragments (250 nM) with or without liposome, these ANKHD1 fragments were incubated with 100 μM BS(PEG)5. The liposome composition was 60% PC / 30% PE / 10% PS. The selected regions show the dimer of ANKHD1 fragments.

All error bars indicate SE. Student's *t*-test, $**P < 0.01$ and $***P < 0.001$. ns, not significant.

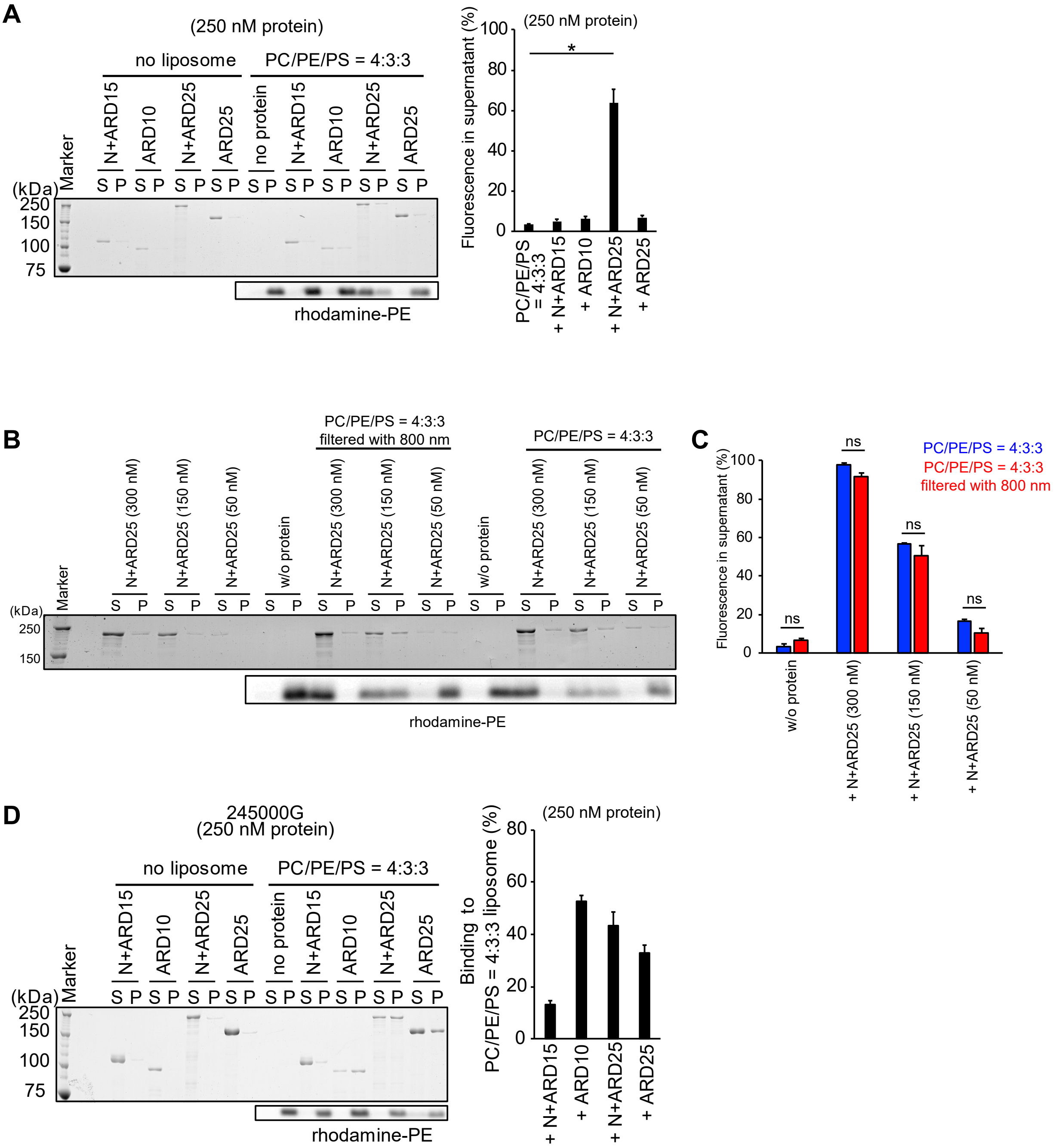

Figure 28. Vesiculation and binding abilities of ANKHD1 to liposome enriched in PS

Figure 28. ***Continued***

(A) Liposome sedimentation assay using ultracentrifugation at 109000 × *g* for N+ARD15, ARD10, N+ARD25, and ARD25 (250 nM). The liposomes were composed of 40% PC / 30% PE / 30% PS and were labelled with rhodamine-PE. The percentage of the fluorescence of Rhodamine-PE in the supernatant measured using ImageJ software are shown on the right as the mean of three independent experiments.

(B) Liposome sedimentation assay using ultracentrifugation at 109000 × *g* for N+ARD25 with liposomes filtered through 800 nm or liposomes without filtration. N+ARD25 was prepared at 50 nM, 150 nM, or 300 nM. The liposomes were composed of 40% PC / 30% PE / 30% PS and were labelled with rhodamine-PE.

(C) The percentages of the fluorescence of Rhodamine-PE in the supernatant in (B) measured using ImageJ software are shown as the mean of three independent experiments.

(D) Liposome sedimentation assay using ultracentrifugation at 245000 × *g* for N+ARD15, ARD10, N+ARD25, and ARD25 (250 nM). Most of the liposomes were precipitated at 245000 × *g*. The liposomes were composed of 40% PC / 30% PE / 30% PS and were labelled with rhodamine-PE. The percentages of the proteins in the pellet measured using ImageJ software are shown as the mean of three independent experiments.

All error bars represent SE. Student’s *t*-test. *$P < 0.05$. ns, not significant.

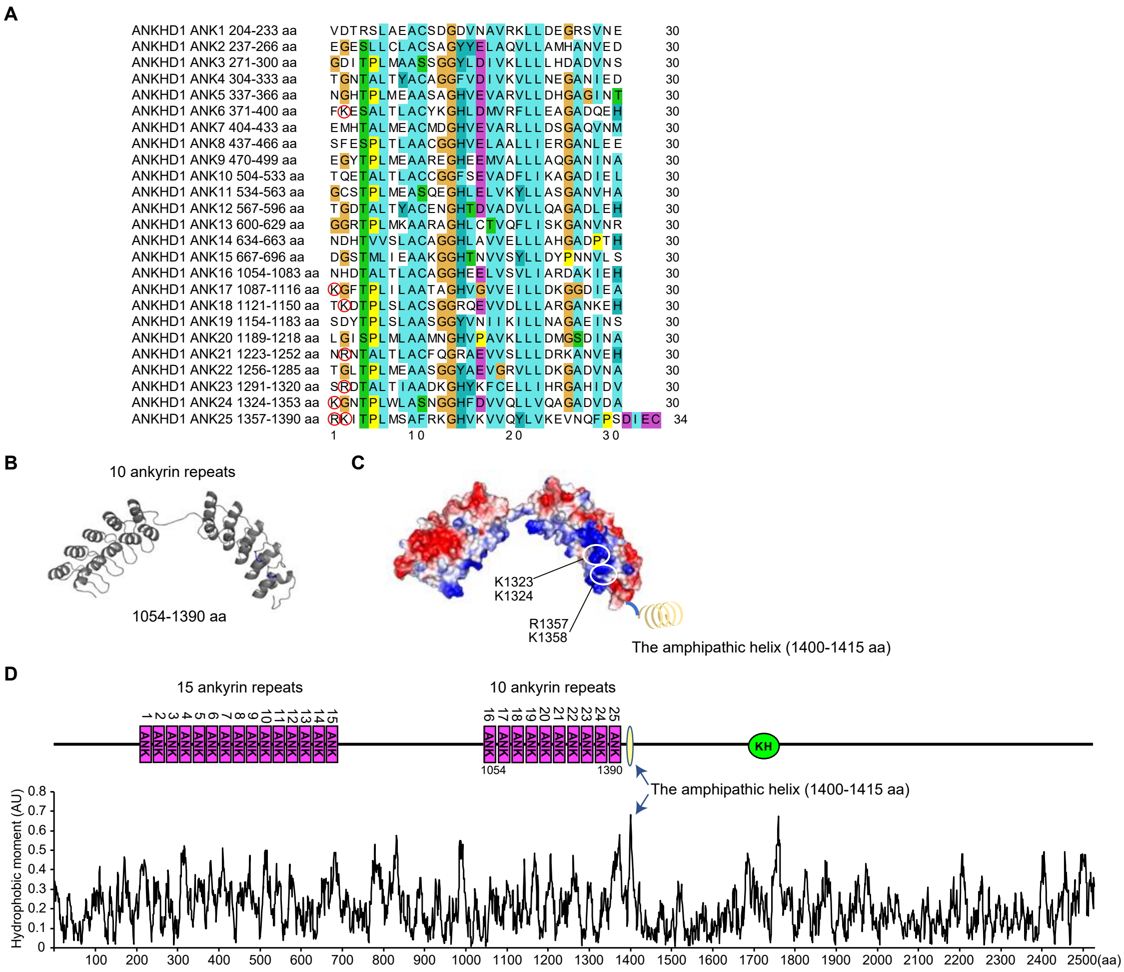

Figure 29. Structural characteristics of the latter 10 ANKs of ANKHD1

(A) Sequence alignment of ANKs in ANKHD1 by Clustal X. The colors in sequence alignment are based in the Clustal X program. Arginine and lysine at position 1 and position 2 in ANKs are indicated with red circles.

(B) Structural model of the latter 10 ANKs (1054-1390 aa) predicted by Phyre2 (http://www.sbg.bio.ic.ac.uk/phyre2).

(C) Electrostatic surface of the latter 10 ANKs generated by Pymol using the model of (B). The amphipathic helix (1400-1415 aa) is also illustrated. The mutated basic amino acid residues, K1323, K1324, R1357, and K1358, are indicated.

(D) The hydrophobic moment of ANKHD1 calculated by using Heliquest. The high score means that the helix is predicted to form an amphipathic helix. Arrow indicates the highest hydrophobic moment of 1400-1415 aa residues in ANKHD1.

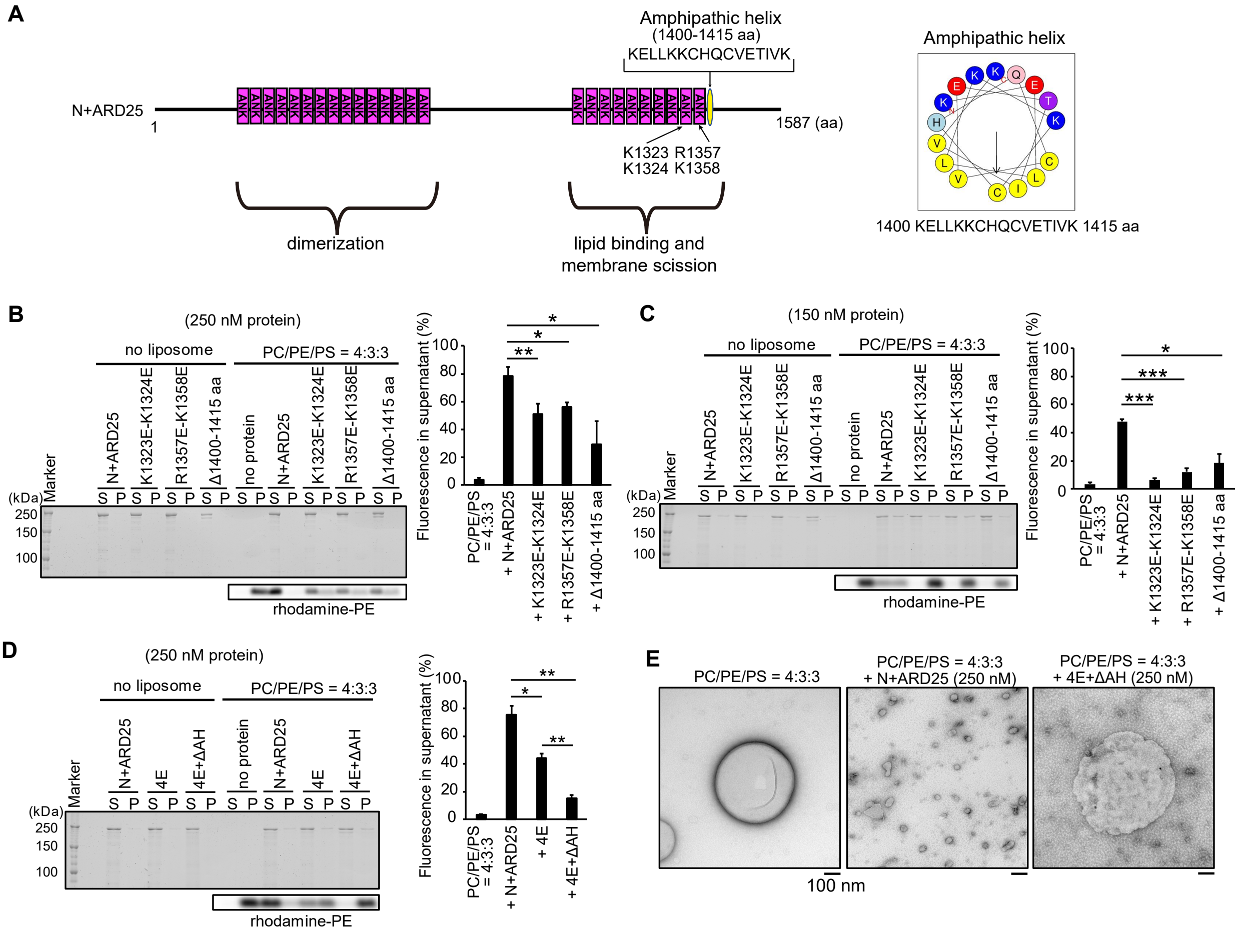

Figure 30. Membrane vesiculation by ANKHD1 is caused by the amphipathic helix and the electrostatic interaction

Figure 30. *Continued*

(A) Illustration of the K1323E-K1324E and R1357E-K1358E mutations in which positively charged amino acids were substituted into negatively charged amino acids and the amphipathic helix of N+ARD25. The wheel diagram of the amphipathic helix predicted by Heliquest is shown. Amphiphilicity of a helix is indicated by the hydrophobic moment.

(B-C) Liposome sedimentation assay using ultracentrifugation at 109000 × *g* for N+ARD25 and its mutants with K1323E-K1324E, R1357E-K1358E or deletion of the amphipathic helix (Δ 1400-1415 aa) at 250 nM (B) and 150 nM (C). The liposome composition was 40% PC / 30% PE / 30% PS. The liposomes were labelled with rhodamine-PE. The percentage of the fluorescence of Rhodamine-PE in the supernatant measured using ImageJ software are shown as the mean of three (B) or four (C) independent experiments.

(D) Liposome sedimentation assay using ultracentrifugation at 109000 × *g* for N+ARD25 and its mutants with K1323E-K1324E-R1357E-K1358E (4E), or K1323E-K1324E-R1357E-K1358E+Δ 1400-1415 aa (4E+ΔAH) (250 nM). The liposome composition was 40% PC / 30% PE / 30% PS. The liposomes were labelled with rhodamine-PE. The percentage of the fluorescence of Rhodamine-PE in the supernatant measured using ImageJ software are shown as the mean of four independent experiments.

(E) Electron micrographs of liposomes composed of 40% PC / 30% PE / 30% PS after incubation with N+ARD25 or 4E+ΔAH at 250 nM for 20 min. Scale bars, 100 nm.

All error bars indicate SE. Student's *t*-test, **P* < 0.05, ***P* < 0.01, and ****P* < 0.001. ns, not significant.

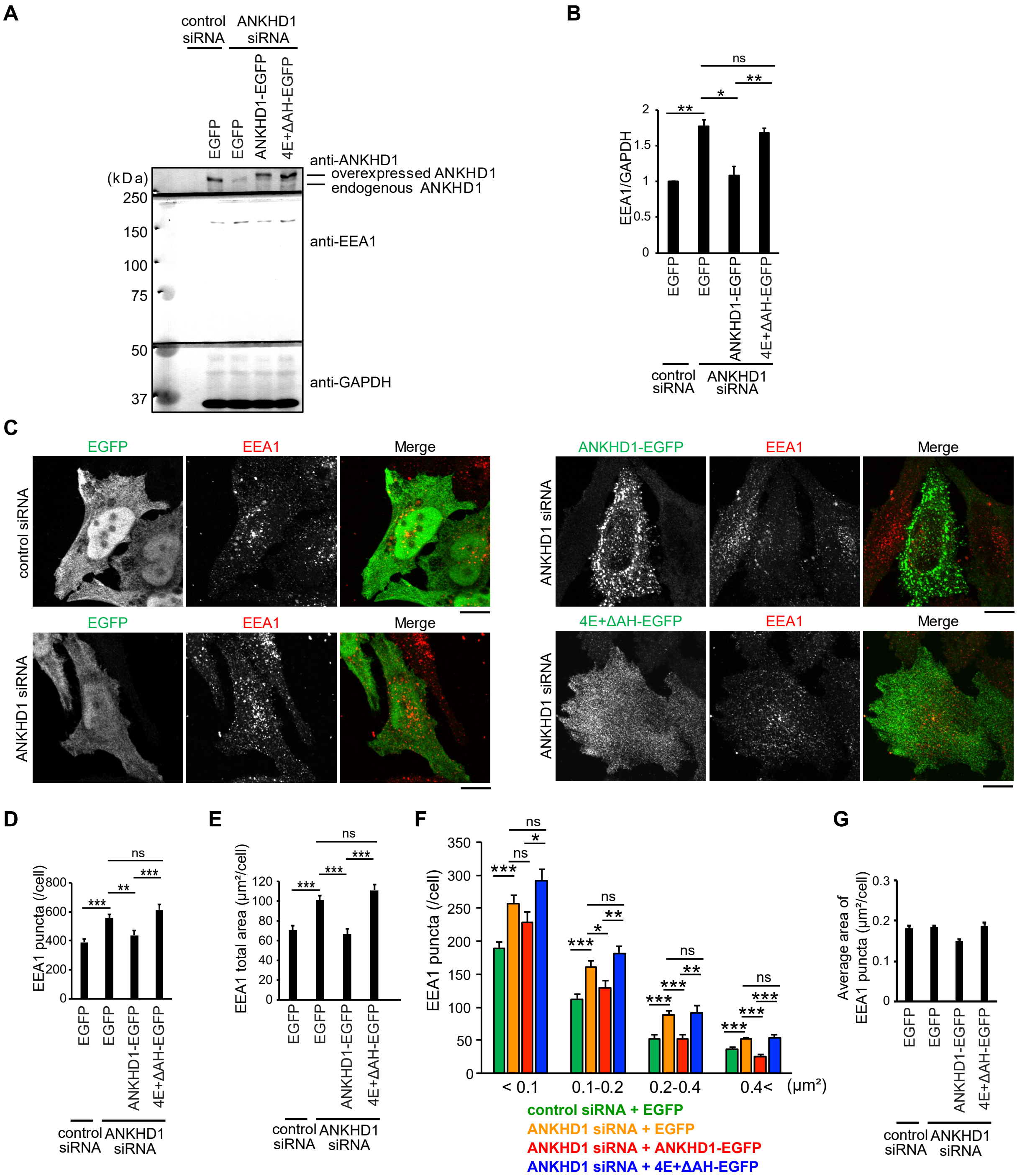

Figure 31. ANKHD1 regulates the number and total area of EEA1-positive early endosomes through the membrane vesiculation ability

Figure 31. ***Continued***

(A) Levels of expressed ANKHD1, endogenous ANKHD1, and endogenous EEA1 in control siRNA-treated HeLa cells expressing EGFP and ANKHD1 siRNA-treated HeLa cells expressing EGFP, ANKHD1-EGFP, or ANKHD1-EGFP with 4E+ΔAH (4E+ΔAH-EGFP) for rescue experiments by western blotting. GAPDH was used as the loading control.

(B) The signal intensities of EEA1 in (A) quantified by ImageJ software are shown as the mean of four independent experiments.

(C) Representative images of endogenous EEA1 as in (A) for the rescue experiments by confocal microscopy. Scale bars, 10 μm

(D-G) The number (D), the total area (E), the size distribution (F), and the average area (G) of EEA1 puncta per cell in (C) analyzed by using ImageJ software are shown as the mean of 27, 27, 25, and 25 cells in three independent experiments for EGFP + control siRNA, EGFP + ANKHD1 siRNA, ANKHD1-EGFP + ANKHD1 siRNA, and 4E+ΔAH-EGFP + ANKHD1 siRNA, respectively.

All error bars indicate SE. Student's *t*-test, *$P < 0.05$, **$P < 0.01$, and ***$P < 0.001$. ns, not significant.

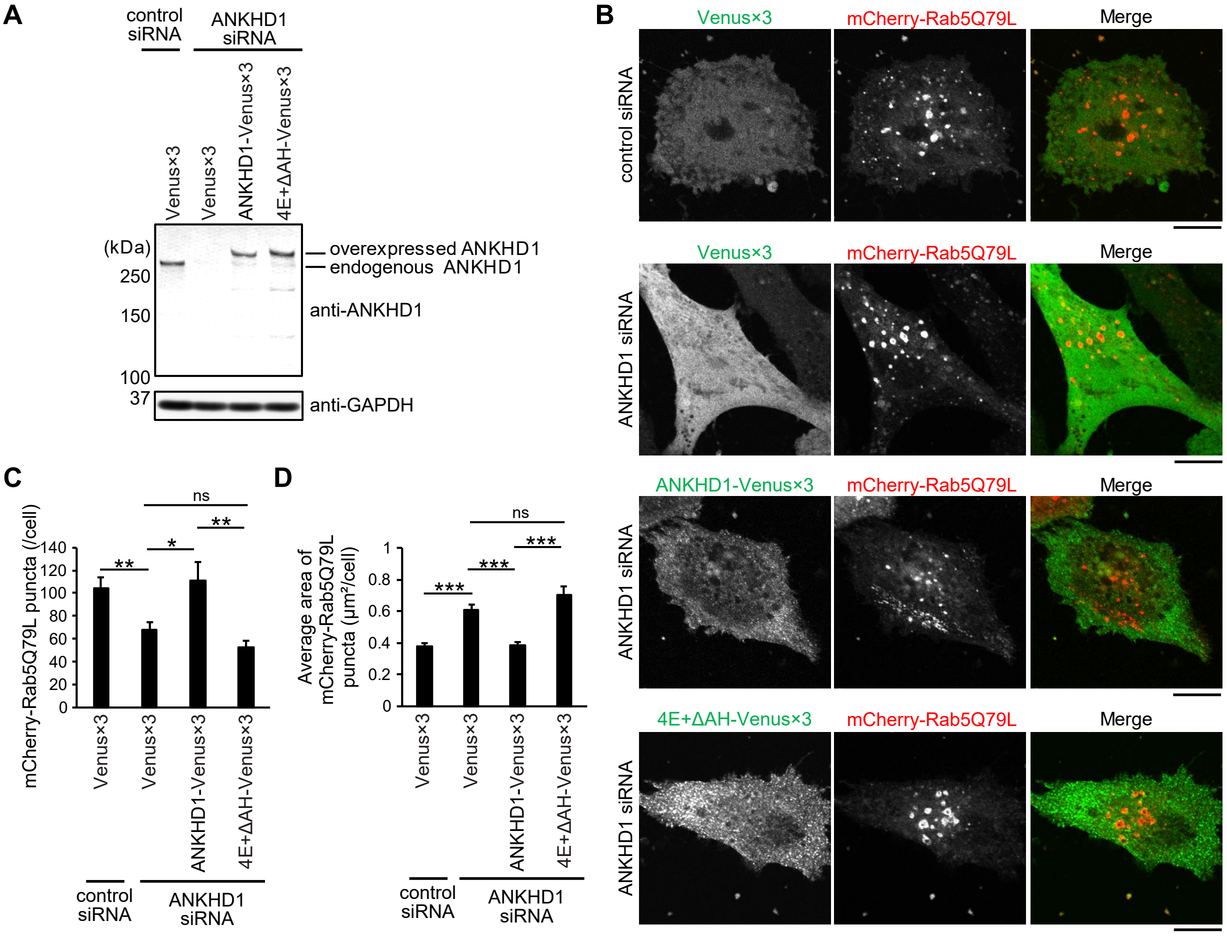

Figure 32. ANKHD1 regulates the number and average size of Rab5-positive early endosomes through the membrane vesiculation ability

Figure 32. *Continued*

(A) Levels of expressed ANKHD1 and endogenous ANKHD1 in control siRNA-treated HeLa cells expressing Venus×3 and ANKHD1 siRNA treated-HeLa cells expressing Venus×3, ANKHD1-Venus×3, or ANKHD1-Venus×3 with 4E+ΔAH (4E+ΔAH-Venus×3) for rescue experiments by western blotting. GAPDH was used as the loading control.

(B) Representative images of control siRNA-treated HeLa cells expressing Venus×3 + mCherry-Rab5Q79L and ANKHD1 siRNA-treated HeLa cells expressing Venus×3 + mCherry-Rab5Q79L, ANKHD1- Venus×3 + mCherry-Rab5Q79L, or 4E+ΔAH-Venus×3 + mCherry-Rab5Q79L for rescue experiments by confocal microscopy. Scale bars, 10 μm

(C, D) The number (C) and average area (D) of mCherry-Rab5Q79L puncta per cell in (B) measured using ImageJ software are shown as the mean of 23, 19, 16, and 19 cells in three independent experiments for Venus×3 + control siRNA, Venus×3 + ANKHD1 siRNA, ANKHD1- Venus×3 + ANKHD1 siRNA, and 4E+ΔAH- Venus×3 + ANKHD1 siRNA, respectively. Error bars indicate SE. Student's *t*-test, $^{*}P < 0.05$, $^{**}P < 0.01$, and $^{***}P < 0.001$. ns, not significant.

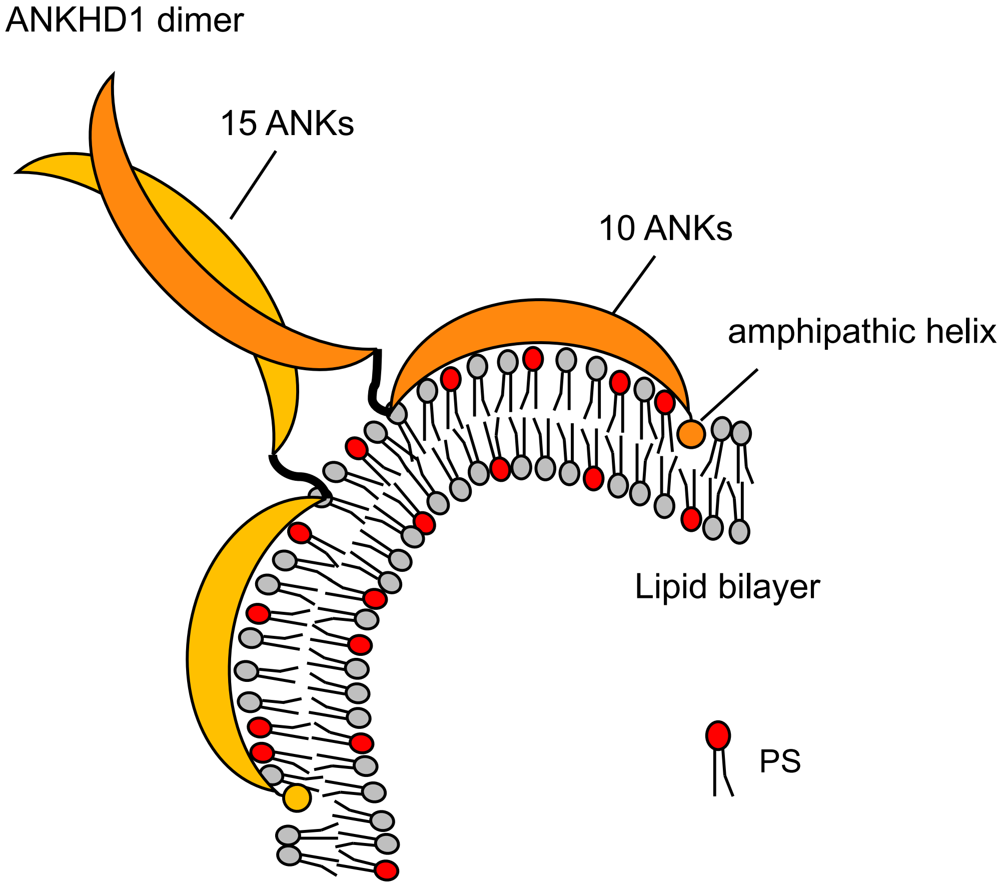

Figure 33. Model of the mechanism of membrane vesiculation by ANKHD1

The schematic illustration of the membrane deformation by the dimeric ANKHD1. ANKHD1 contains the first 15 ANKs and the latter 10ANKs. The first 15 ANKs involve in dimer formation, and the latter 10 ANKs have the membrane deformation ability. The latter 10 ANKs are predicted to have a curved structure with positively charged surface. Furthermore, there is the amphipathic helix (1400-1415 aa) adjacent to the latter 10 ANKs. The membrane binding of the latter 10 ANKs to negatively charged lipid, PS, and insertion of the amphipathic helix into lipid bilayer with the dimer formation contribute to the membrane vesiculation.

Table 1. Source of the ARD-containing protein from NCBI

Name	Source
Arf-GAP with coiled-coil, ANK repeat and PH domain-containing protein 2	NP_084414.1
Ankyrin repeat and FYVE domain-containing protein 1	NP_033801.4
Ankyrin repeat and KH domain-containing protein 1	NP_060217.1
Ankyrin repeat domain-containing protein 11	NP_001074848.2
Ankyrin repeat domain-containing protein 12	NP_001020743.1
Ankyrin repeat domain-containing protein 17	NP_112148.2
Arf-GAP with SH3 domain, ANK repeat and PH domain-containing protein 1	NP_034156.2
Cyclin-dependent kinase 4 inhibitor C	NP_001288297.1
Cyclin-dependent kinase 4 inhibitor D	NP_034008.2
Caseinolytic peptidase B protein homolog	NP_033217.1
Euchromatic histone-lysine N-methyltransferase 1	NP_001012536.2
Euchromatic histone-lysine N-methyltransferase 2	NP_665829.1
Protein fem-1 homolog A-A	NP_034322.3
KN motif and ankyrin repeat domain-containing protein 1	NP_852069.4
Osteoclast-stimulating factor 1	NP_059071.1
Protein phosphatase 1 regulatory subunit 12B	NP_001074776.1
Protein phosphatase 1 regulatory subunit 12C	NP_084110.2
DNA-binding protein RFXANK	NP_001020760.1

Table 2. Strategy of cloning used in the thesis

plasmid	species	restriction site	template	forward primer	reverse primer
pGEX-6P-1-ACAP2 581-770 aa	mouse	BamHI, EcoRI	mouse brain cDNA	5'-CGGGATCCGAAGGAGAAAGGCAAGAGTC-3'	5'-GGAATTCTTATCAGAACTTCTGTGAATC-3'
pGEX-6P-1-ANKFY1 213-1169 aa	mouse	EcoRI	mouse brain cDNA	5'-GGAATTCATGATCAAATCCAAGACAGAG-3'	5'-GGAATTCTTACTAAGAGACTCCACCCAGAGTCAGTAC-3'
pGEX-6P-1-ANKRD11 140-297 aa	mouse	BamHI, EcoRI	mouse brain cDNA	5'-CGGGATCCCCTTCCCAGTCTACAGTGTG-3'	5'-GGAATTCTTAAGTAGAGCTCTCCTCACTGG-3'
pGEX-6P-1-ANKRD12 161-311 aa	mouse	BamHI, EcoRI	mouse brain cDNA	5'-CGGGATCCACGCCAGCCCAGAAGAAAAC-3'	5'-GGAATTCTTATTCATCATCGCCAGACAAAG-3'
pGEX-6P-1-ANKRD17 112-779 aa	mouse	BamHI, EcoRI	mouse brain cDNA	5'-CGGGATCCAGCGAGGAAGAGGAGGACGACGACGAC-3'	5'-GGAATTCTTACTTTTGTTTAGAAGCAGCTTTACTC-3'
pGEX-6P-1-ANKRD17 1045-1410 aa	mouse	BamHI, EcoRI	mouse brain cDNA	5'-CGGGATCCGTTTCCCAACCTCAGACTCCAACTCCAAG-3'	5'-GGAATTCTTATGATGGAAACTGATTGACCTCTTTGAC-3'
pGEX-6P-1-ASAP1 443-737 aa	mouse	BamHI, EcoRI	mouse brain cDNA	5'-CGGGATCCAGCACAGGGGAGAATAGCC-3'	5'-GGAATTCTTAATCCAGATCGTCATCGCTC-3'
pGEX-6P-1-CDKN2C 1-168 aa	mouse	BamHI, EcoRI	mouse brain cDNA	5'-CGGGATCCATGGCCGAGCCTTGGGGGAAC-3'	5'-GGAATTCTTATCACTGCAGGCTTGTGGCTC-3'
pGEX-6P-1-CDKN2d 1-166 aa	mouse	BamHI, EcoRI	mouse brain cDNA	5'-CGGGATCCATGCTTCTGGAAGAAGTCTG-3'	5'-GGAATTCTTATCACATTGGGATCATCATG-3'
pGEX-6P-1-CLPB 86-330 aa	mouse	BamHI, EcoRI	mouse brain cDNA	5'-CGGGATCCGCCTCGTCGGAACGCGGTC-3'	5'-GGAATTCTTACGCAGCACCGACGGTGGCG-3'
pGEX-6P-1-EHMT1 684-1008 aa	mouse	EcoRI	mouse brain cDNA	5'-GGAATTCCAGAGCACAGCCCCCCAGG-3'	5'-GGAATTCTTACACCGTCTTCTCAACAGC-3'
pGEX-6P-1-EHMT2 628-968 aa	mouse	BamHI, EcoRI	mouse brain cDNA	5'-CGGGATCCCGAGCGGATACCTCCCAG-3'	5'-GGAATTCTTAAGCCCGGTTCCCTACCCC-3'
pGEX-6P-1-FEM1A 1-654 aa	mouse	BamHI, EcoRI	mouse brain cDNA	5'-CGGGATCCATGGATCTGCACACAGCG-3'	5'-GGAATTCTTATCAATGCAACTGGATGAAGG-3'
pGEX-6P-1-KANK1 1069-1360 aa	mouse	EcoRI	mouse brain cDNA	5'-GGAATTCGCCAGGGTGGAAGATGAAG-3'	5'-GGAATTCTTATCAGTCAAAAGAACCTCGG-3'
pGEX-6P-1-OSTF1 1-215 aa	mouse	BamHI, EcoRI	mouse brain cDNA	5'-CGGGATCCATGTCCAAGCCACCTCCC-3'	5'-GGAATTCTTATCAGTCTGAGTCTTCGTC-3'
pGEX-6P-1-PPP1R12B 1-358 aa	mouse	BamHI, EcoRI	mouse brain cDNA	5'-CGGGATCCATGGCGGAGCTGGAGCAC-3'	5'-GGAATTCTTAGCTGGACTCTTTGTTTTC-3'
pGEX-6P-1-PPP1R12C 1-345 aa	mouse	EcoRI	mouse brain cDNA	5'-GGAATTCATGTCCGGCGAGGATGGTCC-3'	5'-GGAATTCTTATCTGTGCTTACTACTTGAAG-3'
pGEX-6P-1-RFXANK 1-259 aa	mouse	EcoRI	mouse brain cDNA	5'-GGAATTCATGGAGCCCACTCAGGTTGCAGAGAACC-3'	5'-GGAATTCTTATCACTCGGGGTCCACAGGCCCCAGG-3'

plasmid	species	restriction site	template	forward primer	reverse primer
pGEX-6P-1-ANKHD1 1-885 aa	human	BamHI	ANKHD1 cDNA	5'-GAAGATCTGCCACCATGCTGACTGATAGCGGAGG-3'	5'-GAAGATCTATCTCCTTCCCCTTCTGGGAAG-3'
pGEX-6P-1-ANKHD1 1-886-1587 aa	human	BamHI	ANKHD1 cDNA	5'-GAAGATCTGCCACCATGGGTAGTCTCCCAGAGGATC-3'	5'-GAAGATCTTGCACCACCACCTCTAGGTTC-3'
pGEX-6P-1-ANKHD1 1-1587 aa	human	BamHI	ANKHD1 cDNA	5'-GAAGATCTGCCACCATGCTGACTGATAGCGGAGG-3'	5'-GAAGATCTTGCACCACCACCTCTAGGTTC-3'
pEGFP-N3-ANKHD1 1-885 aa	human	BamHI	ANKHD1 cDNA	5'-GAAGATCTGCCACCATGCTGACTGATAGCGGAGG-3'	5'-GAAGATCTATCTCCTTCCCCTTCTGGGAAG-3'
pEGFP-N3-ANKHD1 886-1587 aa	human	BamHI	ANKHD1 cDNA	5'-GAAGATCTGCCACCATGGGTAGTCTCCCAGAGGATC-3'	5'-GAAGATCTTGCACCACCACCTCTAGGTTC-3'
pEGFP-N3-ANKHD1 1-1587 aa	human	BamHI	ANKHD1 cDNA	5'-GAAGATCTGCCACCATGCTGACTGATAGCGGAGG-3'	5'-GAAGATCTTGCACCACCACCTCTAGGTTC-3'
pEGFP-N3-ANKHD1	human	BamHI	ANKHD1 cDNA	5'-GAAGATCTATCTCCTTCCCCTTCTGGGAAG-3'	5'-GAAGATCTGTTGACATATTTGAGATGC-3'

Table 3. Incubation temperature after addition of IPTG in protein expression

plasmid	temperature
pGEX-6P-1- ANKHD1 1-885 aa (N+ARD15)	20℃
pGEX-6P-1-ANKHD1 886-1587 aa (ARD10)	20℃
pGEX-6P-1-ANKHD1 1-1587 aa (N+ARD25)	12℃
pcold-GST-ANKHD1 195-1418 aa (ARD25)	15℃
pGEX-6P-1-ACAP2 581-770 aa	12℃
pGEX-6P-1-ANKFY1 213-1169 aa	12℃
pGEX-6P-1-ANKRD11 140-297 aa	12℃
pGEX-6P-1-ANKRD12 161-311 aa	12℃
pGEX-6P-1-ANKRD17 112-779 aa	12℃
pGEX-6P-1-ANKRD17 1045-1410 aa	12℃
pGEX-6P-1-ASAP1 443-737 aa	12℃
pGEX-6P-1-CDKN2C 1-168 aa	12℃
pGEX-6P-1-CDKN2D 1-166 aa	12℃
pGEX-6P-1-CLPB 86-330 aa	12℃
pGEX-6P-1-EHMT1 684-1008 aa	12℃
pGEX-6P-1-EHMT2 628-968 aa	12℃
pGEX-6P-1-FEM1A 1-654 aa	12℃
pGEX-6P-1-KANK1 1069-1360 aa	12℃
pGEX-6P-1-OSTF1 1-215 aa	12℃
pGEX-6P-1-PPP1R12B 1-358 aa	12℃
pGEX-6P-1-PPP1R12C 1-345 aa	12℃
pGEX-6P-1-RFXANK 1-259 aa	12℃

Acknowledgments

I am deeply grateful to Prof. Shiro Suetsugu (Nara Institute of Science and Technology) for his kind support, valuable discussion, and considerable encouragement. I would like to show my appreciation to examiners of my doctorate dissertation, Prof. Yoshitaka Fukada (University of Tokyo) as chief examiner, Prof. Miho Ohsugi (University of Tokyo), Prof. Mutsuhiro Takekawa (University of Tokyo), and Prof. Sotaro Uemura (University of Tokyo). I would like to express my gratitude to Assistant Prof. Kyoko Hanawa (Nara Institute of Science and Technology) and Assistant Prof. Tamako Nishimura (Nara Institute of Science and Technology) for kind technical assistance. I would like to thank lab members, Mr. Maruyama Kohei (Nara Institute of Science and Technology) and Mr. Kazuki Kida (Nara Institute of Science and Technology) for helpful support. I would like to express my sincere appreciation to my family for constant cooperation.

The article of my study, which is not peer-reviewed, is previewed in Cell Press Sneak Peek.

Membrane deformation ability of the ankyrin repeat and KH domain-containing protein 1 (ANKHD1) and its involvement in the early endosome enlargement.

Kitamata, M., Hanawa-Suetsugu, K., Maruyama, K., and Suetsugu, S.

This study was finally published in iScience.

Kitamata, M., Hanawa-Suetsugu, K., Maruyama, K., and Suetsugu, S. (2019). Membrane-Deformation Ability of ANKHD1 Is Involved in the Early Endosome Enlargement. iScience *17*, 101-118.

References

Achiriloaie, M., Barylko, B., and Albanesi, J.P. (1999). Essential role of the dynamin pleckstrin homology domain in receptor-mediated endocytosis. Mol Cell Biol *19*, 1410-1415.

Al-Khodor, S., Price, C.T., Kalia, A., and Abu Kwaik, Y. (2010). Functional diversity of ankyrin repeats in microbial proteins. Trends Microbiol *18*, 132-139.

Antonny, B., Burd, C., De Camilli, P., Chen, E., Daumke, O., Faelber, K., Ford, M., Frolov, V.A., Frost, A., Hinshaw, J.E.*, et al.* (2016). Membrane fission by dynamin: what we know and what we need to know. EMBO J *35*, 2270-2284.

Babst, M., Katzmann, D.J., Estepa-Sabal, E.J., Meerloo, T., and Emr, S.D. (2002a). Escrt-III: an endosome-associated heterooligomeric protein complex required for mvb sorting. Dev Cell *3*, 271-282.

Babst, M., Katzmann, D.J., Snyder, W.B., Wendland, B., and Emr, S.D. (2002b). Endosome-associated complex, ESCRT-II, recruits transport machinery for protein sorting at the multivesicular body. Dev Cell *3*, 283-289.

Bigay, J., and Antonny, B. (2012). Curvature, lipid packing, and electrostatics of membrane organelles: defining cellular territories in determining specificity. Dev Cell *23*, 886-895.

Boguski, M.S., and Schuler, G.D. (1995). ESTablishing a human transcript map. Nat Genet *10*, 369-371.

Bonifacino, J.S., and Rojas, R. (2006). Retrograde transport from endosomes to the trans-Golgi network. Nat Rev Mol Cell Biol *7*, 568-579.

Boucrot, E., Pick, A., Çamdere, G., Liska, N., Evergren, E., McMahon, H.T., and Kozlov, M.M. (2012). Membrane fission is promoted by insertion of amphipathic helices and is restricted by crescent BAR domains. Cell *149*, 124-136.

Breeden, L., and Nasmyth, K. (1987). Similarity between cell-cycle genes of budding yeast and fission yeast and the Notch gene of Drosophila. Nature *329*, 651-654.

Buchkovich, N.J., Henne, W.M., Tang, S., and Emr, S.D. (2013). Essential N-terminal insertion motif anchors the ESCRT-III filament during MVB vesicle formation. Dev Cell *27*, 201-214.

Burd, C., and Cullen, P.J. (2014). Retromer: a master conductor of endosome sorting. Cold Spring Harb Perspect Biol *6*.

Busch, D.J., Houser, J.R., Hayden, C.C., Sherman, M.B., Lafer, E.M., and Stachowiak, J.C. (2015). Intrinsically disordered proteins drive membrane curvature. Nat Commun *6*, 7875.

Carlton, J.G., and Martin-Serrano, J. (2007). Parallels between cytokinesis and retroviral budding: a role for the ESCRT machinery. Science *316*, 1908-1912.

Chen, B., Jiang, Y., Zeng, S., Yan, J., Li, X., Zhang, Y., Zou, W., and Wang, X. (2010). Endocytic sorting and recycling require membrane phosphatidylserine asymmetry maintained by TAT-1/CHAT-1. PLoS Genet *6*, e1001235.

Das, A., Nag, S., Mason, A.B., and Barroso, M.M. (2016). Endosome-mitochondria interactions are modulated by iron release from transferrin. J Cell Biol *214*, 831-845.

Daumke, O., Roux, A., and Haucke, V. (2014). BAR domain scaffolds in dynamin-mediated membrane fission. Cell *156*, 882-892.

Devaux, P.F. (1991). Static and dynamic lipid asymmetry in cell membranes. Biochemistry *30*, 1163-1173.

Evans, W.H., and Hardison, W.G. (1985). Phospholipid, cholesterol, polypeptide and glycoprotein composition of hepatic endosome subfractions. Biochem J *232*, 33-36.

Farmer, T., Reinecke, J.B., Xie, S., Bahl, K., Naslavsky, N., and Caplan, S. (2017). Control of mitochondrial homeostasis by endocytic regulatory proteins. J Cell Sci *130*, 2359-2370.

Farsad, K., Ringstad, N., Takei, K., Floyd, S.R., Rose, K., and De Camilli, P. (2001). Generation of high curvature membranes mediated by direct endophilin bilayer interactions. J Cell Biol *155*, 193-200.

Ford, M.G., Mills, I.G., Peter, B.J., Vallis, Y., Praefcke, G.J., Evans, P.R., and McMahon, H.T. (2002). Curvature of clathrin-coated pits driven by epsin. Nature *419*, 361-366.

Friedman, J.R., Dibenedetto, J.R., West, M., Rowland, A.A., and Voeltz, G.K. (2013). Endoplasmic reticulum-endosome contact increases as endosomes traffic and mature. Molecular biology of the cell *24*, 1030-1040.

Gallop, J.L., Jao, C.C., Kent, H.M., Butler, P.J., Evans, P.R., Langen, R., and McMahon, H.T. (2006). Mechanism of endophilin N-BAR domain-mediated membrane curvature. The EMBO journal *25*, 2898-2910.

Gargini, R., Escoll, M., García, E., García-Escudero, R., Wandosell, F., and Antón, I.M. (2016). WIP Drives Tumor Progression through YAP/TAZ-Dependent Autonomous Cell Growth. Cell Rep *17*, 1962-1977.

Gautier, R., Douguet, D., Antonny, B., and Drin, G. (2008). HELIQUEST: a web server to screen sequences with specific alpha-helical properties. Bioinformatics *24*, 2101-2102.

Gautreau, A., Oguievetskaia, K., and Ungermann, C. (2014). Function and regulation of the endosomal fusion and fission machineries. Cold Spring Harbor perspectives in biology *6*.

Gehart, H., Goginashvili, A., Beck, R., Morvan, J., Erbs, E., Formentini, I., De Matteis, M.A., Schwab, Y., Wieland, F.T., and Ricci, R. (2012). The BAR domain protein Arfaptin-1 controls secretory granule biogenesis at the trans-Golgi network. Dev Cell *23*, 756-768.

Grant, B.D., and Donaldson, J.G. (2009). Pathways and mechanisms of endocytic recycling. Nat Rev Mol Cell Biol *10*, 597-608.

He, K., Marsland, R., III, Upadhyayula, S., Song, E., Dang, S., Capraro, B.R., Wang, W., Skillern, W., Gaudin, R., Ma, M.*, et al.* (2017). Dynamics of phosphoinositide conversion in clathrin-mediated endocytic traffic. Nature *552*, 410-414.

Hinshaw, J.E., and Schmid, S.L. (1995). Dynamin self-assembles into rings suggesting a mechanism for coated vesicle budding. Nature *374*, 190-192.

Horvath, S.E., and Daum, G. (2013). Lipids of mitochondria. Prog Lipid Res *52*, 590-614.

Hu, J., Shibata, Y., Voss, C., Shemesh, T., Li, Z., Coughlin, M., Kozlov, M.M., Rapoport, T.A., and Prinz, W.A. (2008). Membrane proteins of the endoplasmic reticulum induce high-curvature tubules. Science *319*, 1247-1250.

Huotari, J., and Helenius, A. (2011). Endosome maturation. The EMBO journal *30*, 3481-3500.

Jarsch, I.K., Daste, F., and Gallop, J.L. (2016). Membrane curvature in cell biology: An integration of molecular mechanisms. J Cell Biol *214*, 375-387.

Jones, S.M., Howell, K.E., Henley, J.R., Cao, H., and McNiven, M.A. (1998). Role of dynamin in the formation of transport vesicles from the trans-Golgi network. Science *279*, 573-577.

Jozsef, L., Tashiro, K., Kuo, A., Park, E.J., Skoura, A., Albinsson, S., Rivera-Molina, F., Harrison, K.D., Iwakiri, Y., Toomre, D.*, et al.* (2014). Reticulon 4 is necessary for endoplasmic reticulum tubulation, STIM1-Orai1 coupling, and store-operated calcium entry. J Biol Chem *289*, 9380-9395.

Kanaji, S., Iwahashi, J., Kida, Y., Sakaguchi, M., and Mihara, K. (2000). Characterization of the signal that directs Tom20 to the mitochondrial outer membrane. J Cell Biol *151*, 277-288.

Katzmann, D.J., Babst, M., and Emr, S.D. (2001). Ubiquitin-dependent sorting into the multivesicular body pathway requires the function of a conserved endosomal protein sorting complex, ESCRT-I. Cell *106*, 145-155.

Keenan, T.W., and Morré, D.J. (1970). Phospholipid class and fatty acid composition of golgi apparatus isolated from rat liver and comparison with other cell fractions. Biochemistry *9*, 19-25.

Kelley, L.A., Mezulis, S., Yates, C.M., Wass, M.N., and Sternberg, M.J. (2015). The Phyre2 web portal for protein modeling, prediction and analysis. Nat Protoc *10*, 845-858.

Kim, D.H., Park, M.J., Gwon, G.H., Silkov, A., Xu, Z.Y., Yang, E.C., Song, S., Song, K., Kim, Y., Yoon, H.S*., et al.* (2014). An ankyrin repeat domain of AKR2 drives chloroplast targeting through coincident binding of two chloroplast lipids. Dev Cell *30*, 598-609.

Kobayashi, T., Stang, E., Fang, K.S., de Moerloose, P., Parton, R.G., and Gruenberg, J. (1998). A lipid associated with the antiphospholipid syndrome regulates endosome structure and function. Nature *392*, 193-197.

Kuge, O., Dascher, C., Orci, L., Rowe, T., Amherdt, M., Plutner, H., Ravazzola, M., Tanigawa, G., Rothman, J.E., and Balch, W.E. (1994). Sar1 promotes vesicle budding from the endoplasmic reticulum but not Golgi compartments. J Cell Biol *125*, 51-65.

Lawe, D.C., Chawla, A., Merithew, E., Dumas, J., Carrington, W., Fogarty, K., Lifshitz, L., Tuft, R., Lambright, D., and Corvera, S. (2002). Sequential roles for phosphatidylinositol 3-phosphate and Rab5 in tethering and fusion of early endosomes via their interaction with EEA1. J Biol Chem *277*, 8611-8617.

Lee, J.E., Westrate, L.M., Wu, H., Page, C., and Voeltz, G.K. (2016). Multiple dynamin family members collaborate to drive mitochondrial division. Nature *540*, 139-143.

Lee, M.C., Orci, L., Hamamoto, S., Futai, E., Ravazzola, M., and Schekman, R. (2005). Sar1p N-terminal helix initiates membrane curvature and completes the fission of a COPII vesicle. Cell *122*, 605-617.

Lee, S., Uchida, Y., Wang, J., Matsudaira, T., Nakagawa, T., Kishimoto, T., Mukai, K., Inaba, T., Kobayashi, T., Molday, R.S., *et al.* (2015). Transport through recycling endosomes requires EHD1 recruitment by a phosphatidylserine translocase. The EMBO journal *34*, 669-688.

Letunic, I., and Bork, P. (2017). 20 years of the SMART protein domain annotation resource. Nucleic Acids Res.

Li, J., Mahajan, A., and Tsai, M.D. (2006). Ankyrin repeat: a unique motif mediating protein-protein interactions. Biochemistry *45*, 15168-15178.

Lux, S.E., John, K.M., and Bennett, V. (1990). Analysis of cDNA for human erythrocyte ankyrin indicates a repeated structure with homology to tissue-differentiation and cell-cycle control proteins. Nature *344*, 36-42.

Machado-Neto, J.A., Lazarini, M., Favaro, P., Franchi, G.C., Nowill, A.E., Saad, S.T., and Traina, F. (2014). ANKHD1, a novel component of the Hippo signaling pathway, promotes YAP1 activation and cell cycle progression in prostate cancer cells. Exp Cell Res *324*, 137-145.

Marquardt, D., Geier, B., and Pabst, G. (2015). Asymmetric lipid membranes: towards more realistic model systems. Membranes (Basel) *5*, 180-196.

Masters, T.A., Tumbarello, D.A., Chibalina, M.V., and Buss, F. (2017). MYO6 Regulates Spatial Organization of Signaling Endosomes Driving AKT Activation and Actin

Dynamics. Cell Rep *19*, 2088-2101.

Masuda, M., Takeda, S., Sone, M., Ohki, T., Mori, H., Kamioka, Y., and Mochizuki, N. (2006). Endophilin BAR domain drives membrane curvature by two newly identified structure-based mechanisms. EMBO J *25*, 2889-2897.

Maxfield, F.R., and McGraw, T.E. (2004). Endocytic recycling. Nat Rev Mol Cell Biol *5*, 121-132.

McCullough, J., Clippinger, A.K., Talledge, N., Skowyra, M.L., Saunders, M.G., Naismith, T.V., Colf, L.A., Afonine, P., Arthur, C., Sundquist, W.I.*, et al.* (2015). Structure and membrane remodeling activity of ESCRT-III helical polymers. Science *350*, 1548-1551.

McMahon, H.T., and Gallop, J.L. (2005). Membrane curvature and mechanisms of dynamic cell membrane remodelling. Nature *438*, 590-596.

McNiven, M.A., and Thompson, H.M. (2006). Vesicle formation at the plasma membrane and trans-Golgi network: the same but different. Science *313*, 1591-1594.

Mosavi, L.K., Cammett, T.J., Desrosiers, D.C., and Peng, Z.Y. (2004). The ankyrin repeat as molecular architecture for protein recognition. Protein science : a publication of the Protein Society *13*, 1435-1448.

Murray, D.H., Jahnel, M., Lauer, J., Avellaneda, M.J., Brouilly, N., Cezanne, A., Morales-Navarrete, H., Perini, E.D., Ferguson, C., Lupas, A.N.*, et al.* (2016). An endosomal tether undergoes an entropic collapse to bring vesicles together. Nature *537*, 107-111.

Nagai, T., Ibata, K., Park, E.S., Kubota, M., Mikoshiba, K., and Miyawaki, A. (2002). A variant of yellow fluorescent protein with fast and efficient maturation for cell-biological applications. Nat Biotechnol *20*, 87-90.

Nakamura, N., Rabouille, C., Watson, R., Nilsson, T., Hui, N., Slusarewicz, P., Kreis, T.E., and Warren, G. (1995). Characterization of a cis-Golgi matrix protein, GM130. J Cell Biol *131*, 1715-1726.

Naslavsky, N., and Caplan, S. (2011). EHD proteins: key conductors of endocytic transport. Trends Cell Biol *21*, 122-131.

Nazarewicz, R.R., Salazar, G., Patrushev, N., San Martin, A., Hilenski, L., Xiong, S., and Alexander, R.W. (2011). Early endosomal antigen 1 (EEA1) is an obligate scaffold for angiotensin II-induced, PKC-alpha-dependent Akt activation in endosomes. J Biol Chem *286*, 2886-2895.

Nishimura, T., Morone, N., and Suetsugu, S. (2018). Membrane re-modelling by BAR domain superfamily proteins via molecular and non-molecular factors. Biochemical Society transactions *46*, 379-389.

Nishio, M., Otsubo, K., Maehama, T., Mimori, K., and Suzuki, A. (2013). Capturing the mammalian Hippo: elucidating its role in cancer. Cancer Sci *104*, 1271-1277.

Oh, P., McIntosh, D.P., and Schnitzer, J.E. (1998). Dynamin at the neck of caveolae mediates their budding to form transport vesicles by GTP-driven fission from the plasma membrane of endothelium. J Cell Biol *141*, 101-114.

Paczkowski, J.E., and Fromme, J.C. (2014). Structural basis for membrane binding and remodeling by the exomer secretory vesicle cargo adaptor. Dev Cell *30*, 610-624.

Pasquali, C.C., Islam, Z., Adamoski, D., Ferreira, I.M., Righeto, R.D., Bettini, J., Portugal, R.V., Yue, W.W., Gonzalez, A., Dias, S.M.G.*, et al.* (2017). The origin and evolution of human glutaminases and their atypical C-terminal ankyrin repeats. J Biol Chem *292*, 11572-11585.

Personnic, N., Bärlocher, K., Finsel, I., and Hilbi, H. (2016). Subversion of Retrograde Trafficking by Translocated Pathogen Effectors. Trends Microbiol *24*, 450-462.

Peter, B.J., Kent, H.M., Mills, I.G., Vallis, Y., Butler, P.J., Evans, P.R., and McMahon, H.T. (2004). BAR domains as sensors of membrane curvature: the amphiphysin BAR structure. Science *303*, 495-499.

Praefcke, G.J., and McMahon, H.T. (2004). The dynamin superfamily: universal membrane tubulation and fission molecules? Nat Rev Mol Cell Biol *5*, 133-147.

Raiborg, C., Bache, K.G., Gillooly, D.J., Madshus, I.H., Stang, E., and Stenmark, H. (2002). Hrs sorts ubiquitinated proteins into clathrin-coated microdomains of early endosomes. Nat Cell Biol *4*, 394-398.

Ramachandran, R., Pucadyil, T.J., Liu, Y.W., Acharya, S., Leonard, M., Lukiyanchuk, V., and Schmid, S.L. (2009). Membrane insertion of the pleckstrin homology domain variable loop 1 is critical for dynamin-catalyzed vesicle scission. Mol Biol Cell *20*, 4630-4639.

Renard, H.F., Johannes, L., and Morsomme, P. (2018). Increasing Diversity of Biological Membrane Fission Mechanisms. Trends Cell Biol *28*, 274-286.

Rink, J., Ghigo, E., Kalaidzidis, Y., and Zerial, M. (2005). Rab conversion as a mechanism of progression from early to late endosomes. Cell *122*, 735-749.

Roux, A., Uyhazi, K., Frost, A., and De Camilli, P. (2006). GTP-dependent twisting of dynamin implicates constriction and tension in membrane fission. Nature *441*, 528-531.

Saftig, P., and Klumperman, J. (2009). Lysosome biogenesis and lysosomal membrane proteins: trafficking meets function. Nat Rev Mol Cell Biol *10*, 623-635.

Sandra, A., and Pagano, R.E. (1978). Phospholipid asymmetry in LM cell plasma membrane derivatives: polar head group and acyl chain distributions. Biochemistry *17*, 332-338.

Sansores-Garcia, L., Atkins, M., Moya, I.M., Shahmoradgoli, M., Tao, C., Mills, G.B., and Halder, G. (2013). Mask is required for the activity of the Hippo pathway effector Yki/YAP. Curr Biol *23*, 229-235.

Schenck, A., Goto-Silva, L., Collinet, C., Rhinn, M., Giner, A., Habermann, B., Brand, M., and Zerial, M. (2008). The endosomal protein Appl1 mediates Akt substrate specificity and cell survival in vertebrate development. Cell *133*, 486-497.

Schiel, J.A., Simon, G.C., Zaharris, C., Weisz, J., Castle, D., Wu, C.C., and Prekeris, R. (2012). FIP3-endosome-dependent formation of the secondary ingression mediates ESCRT-III recruitment during cytokinesis. Nat Cell Biol *14*, 1068-1078.

Scita, G., Confalonieri, S., Lappalainen, P., and Suetsugu, S. (2008). IRSp53: crossing the road of membrane and actin dynamics in the formation of membrane protrusions. Trends Cell Biol *18*, 52-60.

Sedgwick, S.G., and Smerdon, S.J. (1999). The ankyrin repeat: a diversity of interactions on a common structural framework. Trends Biochem Sci *24*, 311-316.

Senju, Y., Itoh, Y., Takano, K., Hamada, S., and Suetsugu, S. (2011). Essential role of PACSIN2/syndapin-II in caveolae membrane sculpting. J Cell Sci *124*, 2032-2040.

Sever, S., Damke, H., and Schmid, S.L. (2000). Dynamin:GTP controls the formation of constricted coated pits, the rate limiting step in clathrin-mediated endocytosis. J Cell Biol *150*, 1137-1148.

Shibata, Y., Hu, J., Kozlov, M.M., and Rapoport, T.A. (2009). Mechanisms shaping the membranes of cellular organelles. Annu Rev Cell Dev Biol *25*, 329-354.

Shimada, A., Niwa, H., Tsujita, K., Suetsugu, S., Nitta, K., Hanawa-Suetsugu, K., Akasaka, R., Nishino, Y., Toyama, M., Chen, L., *et al.* (2007). Curved EFC/F-BAR-domain dimers are joined end to end into a filament for membrane invagination in endocytosis. Cell *129*, 761-772.

Sidor, C.M., Brain, R., and Thompson, B.J. (2013). Mask proteins are cofactors of Yorkie/YAP in the Hippo pathway. Curr Biol *23*, 223-228.

Simunovic, M., Manneville, J.B., Renard, H.F., Evergren, E., Raghunathan, K., Bhatia, D., Kenworthy, A.K., Voth, G.A., Prost, J., McMahon, H.T.*, et al.* (2017). Friction Mediates Scission of Tubular Membranes Scaffolded by BAR Proteins. Cell *170*, 172-184 e111.

Skjeldal, F.M., Strunze, S., Bergeland, T., Walseng, E., Gregers, T.F., and Bakke, O. (2012). The fusion of early endosomes induces molecular-motor-driven tubule formation and fission. J Cell Sci *125*, 1910-1919.

Snead, W.T., Hayden, C.C., Gadok, A.K., Zhao, C., Lafer, E.M., Rangamani, P., and Stachowiak, J.C. (2017). Membrane fission by protein crowding. Proc Natl Acad Sci U S A *114*, E3258-E3267.

Suetsugu, S. (2010). The proposed functions of membrane curvatures mediated by the BAR domain superfamily proteins. J Biochem *148*, 1-12.

Suetsugu, S., Kurisu, S., and Takenawa, T. (2014). Dynamic shaping of cellular membranes by phospholipids and membrane-deforming proteins. Physiol Rev *94*, 1219-1248.

Suetsugu, S., Murayama, K., Sakamoto, A., Hanawa-Suetsugu, K., Seto, A., Oikawa, T., Mishima, C., Shirouzu, M., Takenawa, T., and Yokoyama, S. (2006). The RAC binding domain/IRSp53-MIM homology domain of IRSp53 induces RAC-dependent membrane deformation. J Biol Chem *281*, 35347-35358.

Suetsugu, S., Toyooka, K., and Senju, Y. (2010). Subcellular membrane curvature mediated by the BAR domain superfamily proteins. Semin Cell Dev Biol *21*, 340-349.

Sönnichsen, B., De Renzis, S., Nielsen, E., Rietdorf, J., and Zerial, M. (2000). Distinct membrane domains on endosomes in the recycling pathway visualized by multicolor imaging of Rab4, Rab5, and Rab11. J Cell Biol *149*, 901-914.

Takahashi, N., Hamada-Nakahara, S., Itoh, Y., Takemura, K., Shimada, A., Ueda, Y., Kitamata, M., Matsuoka, R., Hanawa-Suetsugu, K., Senju, Y.*, et al.* (2014). TRPV4 channel activity is modulated by direct interaction of the ankyrin domain to PI(4,5)P_2. Nat Commun *5*, 4994.

Takei, K., McPherson, P.S., Schmid, S.L., and De Camilli, P. (1995). Tubular membrane invaginations coated by dynamin rings are induced by GTP-gamma S in nerve terminals. Nature *374*, 186-190.

Uchida, Y., Hasegawa, J., Chinnapen, D., Inoue, T., Okazaki, S., Kato, R., Wakatsuki, S., Misaki, R., Koike, M., Uchiyama, Y.*, et al.* (2011). Intracellular phosphatidylserine is essential for retrograde membrane traffic through endosomes. Proceedings of the National Academy of Sciences of the United States of America *108*, 15846-15851.

van Meer, G., Voelker, D.R., and Feigenson, G.W. (2008). Membrane lipids: where they are and how they behave. Nat Rev Mol Cell Biol *9*, 112-124.

Vance, J.E., and Steenbergen, R. (2005). Metabolism and functions of phosphatidylserine. Prog Lipid Res *44*, 207-234.

Wang, C., Wei, Z., Chen, K., Ye, F., Yu, C., Bennett, V., and Zhang, M. (2014). Structural basis of diverse membrane target recognitions by ankyrins. Elife *3*.

Wang, H.J., Guay, G., Pogan, L., Sauvé, R., and Nabi, I.R. (2000). Calcium regulates the association between mitochondria and a smooth subdomain of the endoplasmic reticulum. J Cell Biol *150*, 1489-1498.

Ward, J.J., Sodhi, J.S., McGuffin, L.J., Buxton, B.F., and Jones, D.T. (2004). Prediction and functional analysis of native disorder in proteins from the three kingdoms of life. Journal of molecular biology *337*, 635-645.

Wollert, T., Wunder, C., Lippincott-Schwartz, J., and Hurley, J.H. (2009). Membrane scission by the ESCRT-III complex. Nature *458*, 172-177.

Wolter, K.G., Hsu, Y.T., Smith, C.L., Nechushtan, A., Xi, X.G., and Youle, R.J. (1997). Movement of Bax from the cytosol to mitochondria during apoptosis. J Cell Biol *139*, 1281-1292.

Xu, P., Baldridge, R.D., Chi, R.J., Burd, C.G., and Graham, T.R. (2013). Phosphatidylserine flipping enhances membrane curvature and negative charge required for vesicular transport. J Cell Biol *202*, 875-886.

Yang, Y.S., and Strittmatter, S.M. (2007). The reticulons: a family of proteins with diverse functions. Genome Biol *8*, 234.

Zhu, M., Li, X., Tian, X., and Wu, C. (2015). Mask loss-of-function rescues mitochondrial impairment and muscle degeneration of Drosophila pink1 and parkin mutants. Hum Mol Genet *24*, 3272-3285.

Zoncu, R., Perera, R.M., Balkin, D.M., Pirruccello, M., Toomre, D., and De Camilli, P. (2009). A phosphoinositide switch controls the maturation and signaling properties of APPL endosomes. Cell *136*, 1110-1121.